TECHNISCHE UNIVERSITÄT MÜNCHEN

DEPARTMENT OF PHYSICS

PhD thesis in Plasma Physics

Advanced transport modelling in tokamak plasmas

Ivan Erofeev

Supervisor: Prof. Dr. Sibylle Günter
Advisors: Dr. Emiliano Fable
Dr. Clemente Angioni

TECHNISCHE UNIVERSITÄT MÜNCHEN

DEPARTMENT OF PHYSICS

Advanced transport modelling in tokamak plasmas

Ivan Erofeev

Vollständiger Abdruck der von der Fakultät für Physik der Technischen Universität München zur Erlangung des akademischen Grades eines

Doktors der Naturwissenschaften (Dr. rer. nat.)

genehmigten Dissertation.

Vorsitzende:	Prof. Dr. Christine Papadakis
Prüfer der Dissertation:	1. Hon.-Prof. Dr. Sibylle Günter
	2. Prof. Dr. Katharina Krischer

Die Dissertation wurde am 07.06.2018 an der Technischen Universität München eingereicht und durch die Fakultät für Physik am 17.09.2018 angenommen.

Abstract

Energy production from nuclear fusion reactions has presented a challenge for scientists and engineers for the last decades, in particular, due to the necessity to control matter at extremely high temperatures – the so-called plasma state. According to the commonly used concept of magnetic confinement, plasma is created within a magnetic field with toroidal topology. It makes a very complex physical system with dynamics ranging over many orders of magnitude in temporal and spatial scales. Combined with an enormous number of degrees of freedom, this leads to a situation, when a variation of control parameters, like the electron density, the plasma current or the heating power, modifies the operation regime in a non-linear way. These changes are often related to an interplay between various types of instabilities in a plasma, that have different transport properties. A good example is the L-H transition, when, after the heating power exceeds a certain threshold, turbulence at the plasma edge is suppressed by meso-scale shear flows, which significantly increases the edge pressure gradient: plasma transits from the low-confinement mode (L-mode) to the high-confinement mode (H-mode). However, the plasma core behavior is not modified.

In this work we study two macroscopic phenomena observed in several tokamak plasmas, related to transport processes, and still missing a comprehensive and consistent theoretical explanation. The approach used in this thesis is based on integrated modelling of real plasma conditions, in which these phenomena have been experimentally observed. "Integrated" in this context means that the plasma is represented by a complex system of many processes, and all of these are simulated in a self-consistent manner. It can be considered as a numerical experiment, which is able to provide information about the plasma that is extremely difficult or impossible to obtain in a real experiment. Then, by analyzing these simulations, one can draw conclusions about the real plasma, provided that the macroscopic, measurable quantities are identical.

One of the questions is the mechanism of the saturation of the plasma confinement quality, expressed in terms of the energy confinement time τ_{E}, with the increase of plasma density. This phenomenon is observed in plasmas with no (or weak) external heating, when the energy is introduced mainly by Ohmic heating, so the plasma stays in L-mode. The phenomenon consists in the following: at low density, τ_{E} has linear dependence on the density, but at some critical value this dependence becomes weak, and in many cases negative. This is called the transition from linear to saturated Ohmic confinement regime (LOC to SOC). It has been discovered in the mid-eighties, and several hypotheses have been proposed about its mechanism, but no consensus has been reached so far. Here it is demonstrated, how the interplay between the increasing electron-ion coupling, decreasing impurity concentration and the consequent enhancement of the ITG turbulence may lead to such an effect. Additionally, a transition to

the improved Ohmic confinement regime (IOC), when the linear scaling is observed at SOC typical densities, is also reproduced. Parametric dependencies of the heat fluxes in both LOC and SOC regimes are analyzed, and detailed turbulent spectra for each regime are shown.

Another question concerns the mechanism of spontaneous acceleration of the plasma core in the toroidal direction. It has been observed in both L- and H-mode plasmas with common parametric scalings. Here the focus is on the global effect of profile shearing, which breaks the parallel symmetry of the distribution function through poloidal tilting of turbulence and results in finite radial flux of toroidal momentum. While the significance of this effect has been previously demonstrated with global nonlinear gyrokinetic simulations, it has never been approached via integrated modelling of real plasma discharges. Using the tilting angle θ_0 as a free parameter, this work shows how it scales with macroscopic plasma characteristics, as well as investigates mutual dependencies of θ_0 to such quantities as the mean parallel wavevector $k_{\|}$ and the residual stress, as well as to other critical plasma parameters. It is concluded that the sign and the magnitude of the tilting are related to the dominant turbulence type, with the ITG mode producing notably hollow profiles of the plasma toroidal velocity. A proper account for the usually neglected difference between main ion and impurity rotation velocities is shown to be important. The result is found to be consistent with the observed experimental scalings of the rotation velocity.

A particular attention in this work is paid to the impurity content, which is simulated by an additional species of boron ions. Radial transport of boron is studied, showing how the profiles of its concentration vary with the increase of plasma density.

Integrated modelling can be also considered as a validation for the TGLF transport model used in this work. It has demonstrated a good agreement in what is related to the electron channel of energy and particle transport, but some discrepancy in the ion energy transport, which however is shown to not have a significant effect on the conclusions of this work.

Zusammenfassung

Die Energieerzeugung aus Kernfusionsreaktionen stellte in den letzten Jahrzehnten eine Herausforderung für Wissenschaftler und Ingenieure dar, weil die Materie bei extrem hohen Temperaturen – dem sogenannten Plasmazustand – kontrolliert werden muss. Nach dem gebräuchlichen Konzept des magnetischen Einschlusses wird Plasma in einem Magnetfeld mit toroidaler Topologie erzeugt. Dies bildet ein sehr komplexes physikalisches System mit einem Dynamikbereich über viele räumliche und zeitliche Größenordnungen. In Kombination mit einer enormen Anzahl an Freiheitsgraden führt dies zu einer Situation, in der eine Variation von Steuerparametern, wie zum Beispiel die Elektronendichte, der Plasmastrom oder die Heizleistung, das Betriebsregime in einer nichtlinearen Weise verändert. Diese Änderungen stehen oft im Zusammenhang mit verschiedenen Arten von Instabilitäten in einem Plasma, die unterschiedliche Transporteigenschaften aufweisen. Ein gutes Beispiel ist der LH-Übergang, bei dem die Turbulenz im Plasmarand durch mesoskalige Scherströmungen unterdrückt wird, nachdem die Heizleistung einen bestimmten Schwellenwert überschritten hat. Der Randdrucksgradient wird dabei deutlich erhöht, was das Plasma aus dem Low-Confinement-Modus (L-Modus) in den High-Confinement-Modus (H-Modus) bringt. Dabei wird das Verhalten des Plasmakerns jedoch nicht verändert.

In dieser Arbeit untersuchen wir zwei makroskopische Phänomene, die mit Transportprozessen in Zusammenhang stehen. Diese Phänomene wurden in verschiedenen Tokamak-Plasmen beobachtet, doch es fehlt immer noch eine umfassende und konsistente theoretische Erklärung. Der Ansatz in dieser Arbeit basiert auf einer integrierten Modellierung realer Plasmabedingungen, unter welchem die Phänomene experimentell beobachtet wurden. "Integriert" bedeutet in diesem Kontext, dass das Plasma durch ein komplexes System von vielen Prozessen repräsentiert wird, und diese in einer selbstkonsistenten Weise simuliert werden. Es kann als ein numerisches Experiment betrachtet werden, welches Informationen über das Plasma liefert, die in einem realen Experiment extrem schwierig oder sogar unmöglich zu erhalten sind. Durch Analyse dieser Simulationen kann man Erkenntnisse über das reale Plasma erhalten, sofern die makroskopischen messbaren Größen identisch sind.

Eine der Fragen ist der Mechanismus der Sättigung der Plasmaeinschlussqualität, ausgedrückt in der Energieeinschlusszeit τ_{E}, mit dem Anstieg der Plasmadichte. Dieses Phänomen wird in Plasmen ohne (oder mit schwache) externe Heizung beobachtet, sodass die Energie hauptsächlich ohmsch eingebracht wird, und das Plasma im L-Modus bleibt. Das Phänomen lässt sich folgendermaßen zusammenfassen: für niedrige Plasmadichten hat τ_{E} eine lineare Abhängigkeit von der Plasmadichte, doch ab einem gewissen kritischen Wert wird diese Abhängigkeit schwach und in vielen Fällen sogar negativ. Dies wird als Übergang vom linearen zum gesättigten ohmschen Einschluss-

Regime (LOC zu SOC) bezeichnet. Es wurde Mitte der achtziger Jahre entdeckt, und es wurden mehrere Hypothesen über seinen Mechanismus vorgeschlagen. Bisher wurde jedoch kein Konsens erzielt. Hier zeigen wir, wie das Wechselspiel zwischen der zunehmenden Elektron-Ionen-Kopplung, abnehmender Störstellenkonzentration und der daraus folgenden Verstärkung der ITG-Turbulenz zu einem solchen Effekt führen kann. Zusätzlich wird ein Übergang zu dem verbesserten ohmschen Einschluss-Regime (Improved Ohmic Confinement, IOC) reproduziert, wenn die lineare Skalierung bei SOC-typischen Dichten beobachtet wird. Parametrische Abhängigkeiten der Wärmeströme sowohl in LOC als auch SOC-Regimes werden analysiert, und detaillierte Turbulenzspektren für jedes Regime werden gezeigt.

Eine weitere Frage betrifft den Mechanismus der spontanen Beschleunigung des Plasmakerns in toroidaler Richtung. Es wurde in L- und H-Modus Plasmen mit gemeinsamen parametrischen Skalierungen beobachtet. Wir legen den Fokus auf dem globalen Effekt der Profilscherung, welche die parallele Symmetrie der Verteilungsfunktion durch poloidale Neigung der Turbulenz bricht und zu einem endlichen radialen Fluss des toroidalen Impulses führt. Die Bedeutung dieses Effekts wurde zuvor mit globalen nicht-linearen gyrokinetischen Simulationen demonstriert. Mit integrierter Modellierung von realen Plasmaentladungen wurder er jedoch nie gezeigt. Unter der Verwendung des Neigungswinkels θ_0 zwischen den turbulenten Strukturen und der radialen Richting als ein freier Parameter zeigt diese Arbeit, wie der Neigungswinkel mit makroskopischen Plasmaeigenschaften skaliert. Es werden wechselseitige Abhängigkeiten zwischen θ_0 und Größen wie zum Beispiel den durchschnittlichen parallelen Wellenvektor $k_{\|}$ und die Restspannung. Das Vorzeichen und die Stärke der Neigung stehen dabei in Zusammenhang mit dem dominanten Turbulenztyp, wobei der ITG-Typ besonders Hohlprofile der toroidalen Geschwindigkeit erzeugt. Es wird gezeigt, dass eine angemessene Berücksichtigung des normalerweise vernachlässigten Differenz zwischen den Drehgeschwindigkeiten der Hauptionen und der Störstellen wichtig ist. Das Ergebnis stimmt mit den beobachteten experimentellen Skalierungen der Rotationsgeschwindigkeit überein.

Ein besonderes Augenmerk wird in dieser Arbeit auf den Störstellen gelegt, die durch einen Zusätz des Borspezies simuliert werden. Der radiale Transport von Bor wird untersucht, um zu zeigen, wie sich die Konzentrationsprofile mit der Zunahme der Plasmadichte verändern.

Die integrierte Modellierung kann auch als Validierung für das in dieser Arbeit verwendete TGLF-Transportmodell betrachtet werden. Es hat eine gute Übereinstimmung zwischen Simulation und Experiment in Bezug auf den Elektronenkanal von Energie und Teilchentransport gezeigt. Eine gefundene Diskrepanz im Ionenenergietransport zeigt keinen signifikanten Einfluss auf die hier vorgestellten Ergebnisse.

Contents

Chapter 1

Introduction

1.1 Magnetic confinement concepts

Current views on the way to achieving controlled thermonuclear fusion imply confinement of a high-temperature plasma. Since a plasma consists of charged particles, one can hold it with quasi-stationary magnetic fields. The principle of *magnetic confinement* is based on the fact that charged particles move freely along magnetic field lines, but gyrate in the transverse plane, thereby staying pinned to them. The first magnetic confinement devices had the linear configuration with higher magnetic field on the two ends, trying to exploit the magnetic mirror effect (see Sec. 2.1.2, Fig. 2.3), but proved not effective enough. It became clear, that the magnetic field lines should be closed on themselves, so that the resulting field has the toroidal topology. In this case, the magnetic field lines are curved, which gives rise to the drift motion of charged particles across the field lines (see Sec. 2.1.2). The magnetic field lines should form a toroidal helix in order to compensate for the vertical drift by the poloidal motion of particles, so that the particle orbits are closed. There are two types of devices with toroidal helical field, the *tokamaks* and *stellarators*.

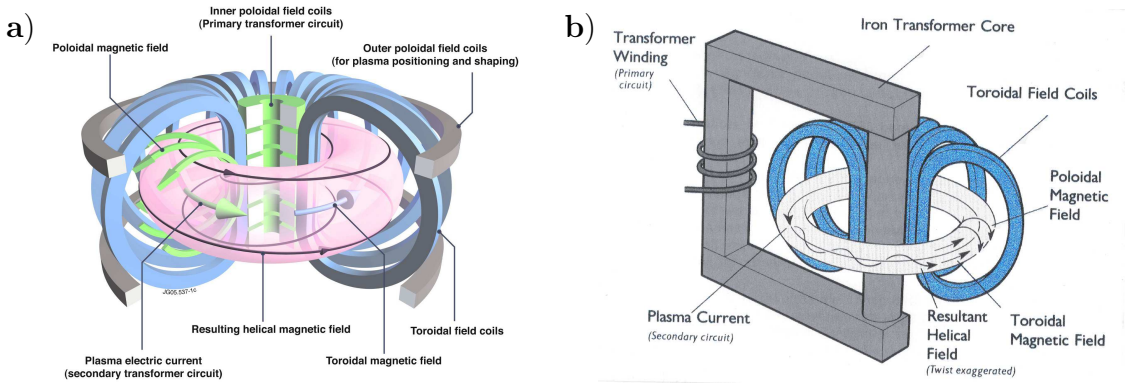

Figure 1.1: *a) Conventional tokamak design and components, b) operational principle.*

The tokamak (Russian acronym for *Toroidal chamber with magnetic coils*) concept relies on a magnetic field configuration with toroidal symmetry. A sketch of such

device is shown in Fig. 1.1. A conventional tokamak consists of a vacuum chamber, a central solenoid coil, a set of toroidal field coils and few poloidal field coils for fine plasma shaping. The operational principle is as follows. The main toroidal field coils create the toroidal magnetic field. A small amount of operational gas (D-T mixture in a fusion reactor) is injected into the vacuum chamber. Varying electric current in the central solenoid ionizes the gas and induces toroidal electric current in the plasma (the transformer principle), as plasma is a good electric conductor. This plasma current induces poloidal magnetic field and additionally heats up the plasma according to the Joule's law (usually referred to as Ohmic heating). The resultant helical field configures itself into nested closed surfaces of constant magnetic flux, and confines the hot plasma in the vessel, away of its walls. However, the necessity to vary the solenoid current limits the operation time of a plasma discharge.

Ohmic heating efficiency reduces significantly as plasma temperature increases, as the plasma resistivity follows the Spitzer relation, $\eta \sim T^{-3/2}$, so less heat is produced at high temperature. Hence, other (external) heating systems are usually applied, such as microwave radiation at electron and ion cyclotron resonant frequencies (ECR and ICR) or injection of beams of neutral particles (NBI). These can also be used to drive additional current in the plasma, partly or fully replacing the solenoid-induced plasma current, which allows for extended pulse duration, up to the regime of steady operation.

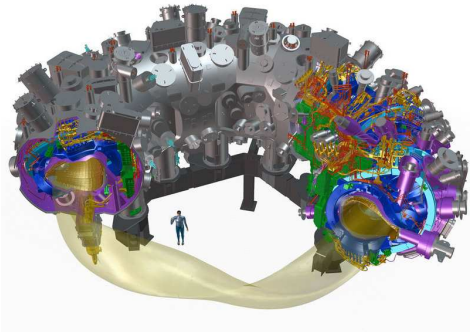

Figure 1.2: *Stellarator Wendelstein 7-X structure. The main coils are shown in blue, confined plasma – in yellow.*

The stellarator (able to deliver *Stellar* energy) concept unifies a number of toroidal magnetic confinement designs where no significant plasma current is presumed, as all the confining magnetic fields are created by external (solid) coils. The most advanced configurations feature very complex geometry of the coils, like in Wendelstein 7-X (see Fig. 1.2), that have to create a magnetic field with twisted field lines. Unlike tokamaks, stellarators do not have general toroidal rotational symmetry, but usually feature n-fold toroidal symmetry (W7-X, for example, is 5-fold toroidally symmetric).

By now the world's fusion research has advanced the most in the tokamak direction, and the first international thermonuclear experimental reactor (ITER) is a

tokamak. In the following, we will focus on toroidally symmetric tokamak plasmas, though several processes are similar in tokamaks and stellarators.

1.2 Transport models for tokamak plasmas

In a tokamak, plasma temperature of around 20 keV and density of around $10^{20}\,\mathrm{m}^{-3}$ has to be achieved in the plasma core, but in the vicinity of the vessel wall the temperature has to be maintained lower than the wall melting point. Therefore, any process that leads to a transfer of particles and energy from the core towards the wall, across the magnetic field, is unfavorable, as it reduces the confinement quality and lowers the maximum achievable plasma pressure in the core. Energy transport is historically the main concern, as well as the means to reduce it and increase the core plasma pressure and the energy confinement time. But there are other transport-related problems. Differences in particle transport of various ion species (main fuel species, product alpha-particles and/or impurity species) establish radial profiles of their densities, which affect reactor efficiency and should be controlled. For example, alpha-particles have to be transported out of the core, as they dilute the fuel and lower the fusion rate; impurities seeded at plasma edge in order to enhance radiation and decrease temperature of the "exhausted" plasma must not penetrate the core, as they would cool it down. Transport of angular momentum is another important process to understand and control, as inducing plasma toroidal and poloidal rotation helps stabilize instabilities and reduce energy transport. Theoretical understanding is a key in every aspect here, that allows us to predict and control plasma parameters. This requires the construction of an adequate mathematical model of the plasma, as well as the means to compute the relevant quantities from it, such as heat conductivity or viscosity.

Plasma is a highly dynamical system with an enormous number of degrees of freedom (of the order of number of particles, $\sim 10^{20}$) and a wide range of characteristic times or frequencies. The smallest and fastest scale is the electron gyration, with typical frequency about 10^{11} Hz and radius around 0.1 mm, on the other end is the global transport scale with frequency of the order of 10 Hz and size around 1 m. The motion of an individual particle is governed by electric and magnetic fields, but redistribution of particles also changes this field. The analytical solution of a system of equations including all particles and field equations does not seem possible. But even for a numerical solution with modern supercomputers such task is too demanding. A more effective approach is statistical (also referred to as *kinetic*), solving the general kinetic equation

$$\frac{dF}{dt} = \frac{\partial F}{\partial t} + \frac{d\vec{x}}{dt} \cdot \frac{\partial F}{\partial \vec{x}} + \frac{d\vec{v}}{dt} \cdot \frac{\partial F}{\partial \vec{v}} = C(F)$$

for a 6-dimensional probability distribution function (6D phase-space has 3 spatial and 3 velocity dimensions). The PDF $F(\vec{x}, \vec{v}, t)$ at a given point of the 6D phase-space defines the number of particles at the given position $\vec{x}$ with the given velocity $\vec{v}$. The

temporal resolution of the PDF solution should be higher than the fastest physical time scale in the system, that is the electron gyrofrequency. Hence, one needs $\sim 10^{11}$ time steps to see global transport variations, which, provided the adequate space and velocity resolution, is computationally extremely expensive and proves impractical.

A technique has been developed to perform a coordinate transformation, which eliminates the fast electron gyration and reduces the phase-space dimensionality to five. Instant position of a particle is substituted with a gyroperiod-averaged position, and the equation of motion is reformulated. When performed correctly, this allows one to describe the motion of gyrating particles at a longer time scale, but keeping all the necessary information on the gyro-orbit parameters [1]. Such approach is called *gyrokinetic*, it is widely used in plasma studies. Still, the general gyrokinetic (GK) equation is non-linear, and simulating the whole plasma volume (global simulation) is very expensive computationally, yet it provides a good insight into fine processes in the plasma. The GK equation may be also solved on a limited radial extend, for a single flux tube, which however leads to the elimination of some effects [2]. Assuming the deviations from the equilibrium Maxwellian distribution are small and solving only for the fluctuating part, as well as linearizing the GK equation helps reduce the computational cost, but somewhat limits the application range to the plasma regions far from the edge of the confined volume. The linear solution can be corrected on the basis of linear to non-linear comparison for some specific cases, so that the result of such corrected linear (referred to as *quasi-linear, QL*) approach agrees well with that of non-linear. This way reasonably accurate transport coefficients can be obtained at low computational cost.

Usually the quantities of interest like density of plasma species or energy fluxes, are related to the so-called velocity moments of the distribution function, where a n-order moment is

$$\mu_n = \int d^3\vec{v}\,\vec{v}^n F.$$

These relations are presented in table 1.1, where $\vec{u}$ is the local mean plasma velocity.

If one takes moments of the whole kinetic equation, one gets macroscopic equations that describe a fluid. In order to obtain a fully consistent description, one needs infinite number of moments, since every n-order moment depends on the (n+1)-order. However, in practice only the moments up to the third order are used (see table1.1), obtained with approximated higher order moments, the so-called closure condition. The modeling approach based on solving the gyrokinetic moment equations without computing the GK distribution function itself is called *gyrofluid*. Depending on the choice of the closure condition, it may include also kinetic physical effects such as wave-particle interaction.

Development and usage of simplified transport models like quasi-linear gyrokinetic and gyrofluid are essential for simulations of the plasma evolution during discharges with given parameters. While non-linear global gyrokinetic simulations of tokamak plasmas require many hours of operation on multi-processor supercomputers,

Order	Quantity	Expression
0	Number density	$n = \int d^3\vec{v}\, F$
1	Particle flux	$\vec{\Gamma} \equiv n\vec{u} = \int d^3\vec{v}\, \vec{v} F$
2	Stress tensor	$\bar{\bar{\Pi}} = \int d^3\vec{v}\, m\vec{v}\vec{v}\, F$
2	Pressure tensor	$\bar{\bar{P}} = \int d^3\vec{v}\, m(\vec{v}-\vec{u})(\vec{v}-\vec{u})\, F$
3	Energy flux	$\vec{Q} = \int d^3\vec{v}\, \frac{mv^2}{2}\, \vec{v} F$
3	Heat flux	$\vec{q} = \int d^3\vec{v}\, \frac{m}{2}(\vec{v}-\vec{u})^2\, (\vec{v}-\vec{u}) F$

Table 1.1: *Lower order velocity moments of the distribution function that correspond to measurable quantities [3]*

relatively simple QL transport models run within few seconds on an average processor and represent workhorses of tokamak plasma transport modelling.

1.3 About this thesis

This work is dedicated to theoretical studies of few selected transport problems presenting unresolved issues for fusion research.

The first one is the energy confinement time behavior in the L-mode plasmas[1]. The confinement quality is usually estimated by a ratio between the energy stored in plasma and the loss power, called the energy confinement time:

$$\tau_{\mathrm{E}} = \frac{W}{P_{loss}} = \frac{\frac{3}{2}\sum_a \int n_a T_a dV}{P_{heat} - P_{rad}} \tag{1.1}$$

It has been observed in many tokamaks that the energy confinement of Ohmically heated L-mode plasmas scales linearly with the plasma density [4] until a critical value is reached, after which the confinement stays constants or even degrades, see [5] and references therein. The two regimes are called Linear and Saturated Ohmic Confinement (LOC and SOC). It has been suggested to link them to a shift in turbulence regime from TEM-dominated to ITG–dominated, that modifies transport [6–8]. Experimentally it is very difficult to reliably define the dominant turbulent mode [9]. Hence, in order to support or oppose this hypothesis, integrated plasma simulations are necessary that include realistic models of heat and particle transport, focusing on distinguishing transport properties of the TEM and ITG turbulent modes. A direct comparison to

[1] low-confinement mode of operation, as opposed to the high-confinement mode (H-mode), when the formation of the edge transport barrier reduces edge turbulent transport and enhances core plasma pressure

experimental measurements for model parametrization to different plasma conditions would ensure the validity of this study.

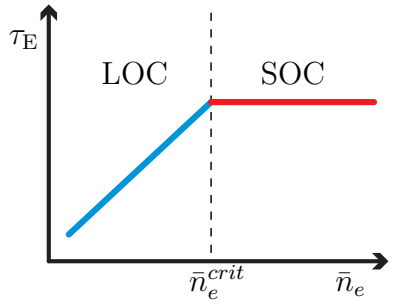

Figure 1.3: *Sketch of τ_E as a function of mean density in Ohmically heated plasmas*

The second issue is the nature of plasma intrinsic toroidal rotation. It has been found that the toroidal plasma can achieve a finite toroidal rotation velocity without any external source of torque in many tokamaks [10–16]. This phenomenon is now known as intrinsic rotation and it is believed to be caused by a component of the stress tensor not related to either viscosity or pinch. It has been shown, that a plasma at rest, i.e. having the toroidal angular velocity $\omega_\phi = 0$ and its radial gradient $\partial\omega_\phi/\partial r = 0$ (thus no toroidal momentum diffusion and convection), still possesses a certain residual stress, that tends to accelerate the plasma. This part of the stress tensor is usually related to a violation of the spatial symmetry of the distribution function, which would lead to net turbulent momentum transport and cause plasma toroidal flows. From the observations it follows that the character of the plasma intrinsic rotation strongly depends on the magnetic field, current and collisionality, and is found to twice flip the rotation direction in the core – from co- to counter-current and back again – as the density grows. Many residual stress mechanisms have been investigated numerically, on the basis of gyrokinetic or fluid theory [17–24]. Their predictions usually deliver specific quantities like the rotation velocity gradient or the residual stress for arbitrary plasma configuration. A general theory of the residual stress should catch this alternating behavior naturally. Moreover, revealing the conditions of such rotation transitions can be the key to understanding its origin. Therefore, the analysis and modelling of momentum transport in purely L-mode discharges without auxiliary NBI heating (which introduces unwanted external torque) is needed.

Both problems concern Ohmically heated L-mode plasmas and might be physically related, as the critical density of the LOC–SOC transition was found to be close to the value at which the spontaneous plasma toroidal rotation flips from co– to counter–current. Both also require an accurate, mode-specific model of turbulent transport. Along with self–consistent evolution of plasma profiles, such as temperature and density, this poses a demanding simulation task. While modern gyrokinetic codes allow such simulations [25, 26] only at enormously high computational costs, a faster and easier yet sufficiently comprehensive way is implemented in this work. Here, the theoretical investigation is done by means of integrated modeling of tokamak plasmas with

the ASTRA transport modeling system, coupled to quasi-linear gyrofluid transport model TGLF and neoclassical transport model NEO.

The thesis is organized as follows. Chapter 2 discusses some main properties of a plasma in a tokamak, and what types of motion occur in a magnetized plasma. Transport processes are described in detail, with particular stress on turbulence-driven transport. In the end of this chapter an overview of the transport modeling software used in this work is given. Chapter 3 presents the ASDEX Upgrade tokamak parameters, where the experimental data have been acquired, which are used for reference and boundary conditions of the simulations. These data are also described, providing some detail on the diagnostic tools, measurement processing techniques, as well as the parameter range they cover. Chapter 4 presents the simulations setup and results of the LOC-SOC transition modelling. The analysis of simulated plasma properties and their comparison to the measurements is provided. Emphasis is given to the core turbulence characteristics, and the relations between the microinstabilities and the global plasma confinement parameters. Chapter 5 applies a similar approach to the problem of plasma intrinsic rotation generation. The discussed mechanism is presented with a simple fluid model, however a more sophisticated version of it is used in the simulations. The relations between model parameters are investigated in detail, making a link between the observed quantities and the core turbulence regime. Section 5.7 provides the results of boron impurity density simulations, validating the assumption of its radially constant concentration, which is used in the rest of this work. Chapter 6 summarizes the results of this work and provides some outlook.

Chapter 2

Theory of transport in tokamak plasmas

Plasma can be defined as an ionized state of matter, and its behavior is dominated by collective effects due to long-range electrostatic and magnetic interactions. It should therefore contain a significant fraction of unbound charged particles (usually electrons and positive ions), i.e. be at least partially ionized. The ionization degree, at which a gas starts to behave like plasma, is around 1%. In practice, a piece of ionized matter must fulfil several criteria in order to be considered a plasma. It is called magnetized if an external magnetic field is strong enough to introduce a distinct anisotropy in plasma motion. Magnetic field geometry plays an essential role in magnetic confinement fusion, as it defines stability and confinement quality of plasma in fusion machines. They are designed in such a way to possibly reduce particles and energy losses, which largely depend on particle trajectories. Additionally, large pressure gradients in fusion plasmas lead to various microinstabilities and associated to them turbulent state, which presents a transport channel of major concern. Various types of microinstabilities, as well as the related transport processes, are also reviewed in this chapter.

2.1 Magnetized plasma in tokamaks

2.1.1 Basic plasma parameters

In a plasma, the average electric charge density is close to zero, which is ensured by electrostatic forces between particles. This property is called quasineutrality. Consider a piece of plasma with n electrons per volume unit and the same number of (hydrogen) ions [27]. Assume that because of thermal motion a density fluctuation δn appeared and caused charge separation over a distance λ. The electric field potential ϕ follows the Poisson's equation $\Delta\phi = -e\,\delta n/\varepsilon_0$, where an approximation can be made $\Delta\phi \approx \delta\phi/\lambda^2$ with $\delta\phi$ the potential difference over the charge separation distance. This gives a

relation

$$\delta\phi \approx \frac{e\,\delta n}{\varepsilon_0}\,\lambda^2$$

The potential energy $e\,\delta\phi$ should be of the order of the kinetic energy T, since the fluctuation is thermal, so for the fluctuation amplitude it can be written

$$\frac{\delta n}{n} \sim \frac{\varepsilon_0 T}{ne^2\lambda^2}.$$

This consideration gives an expression for a typical charge separation scale λ_D, called the *Debye radius*:

$$\lambda_D = \sqrt{\frac{\varepsilon_0 T}{ne^2}} \tag{2.1}$$

On the scale of a typical plasma size L the relative charge imbalance is $\delta n/n \sim \lambda_D^2/L^2$. Hence, quasineutrality follows from $L \gg \lambda_D$.

Electrons are two orders of magnitude more mobile than ions, so they react faster to neutralize the charge separation, while ions can be considered at rest. The time it takes can be computed from fluid equations, but we use a simple consideration here. Since $e\,\delta\phi \approx T_e$, the reaction time is $\lambda_D/v_{th,e}$, the separation distance over the electron thermal velocity. Inverse of this is the characteristic frequency, called the *plasma frequency*:

$$\omega_p = \frac{v_{th,e}}{\lambda_D} = \sqrt{\frac{T}{m_e}}\sqrt{\frac{ne^2}{\varepsilon_0 T}} = \sqrt{\frac{ne^2}{\varepsilon_0 m_e}} \tag{2.2}$$

Coulomb interaction increases the concentration of negative charges around the positive and vice versa, thus the electric potential of a given charge decreases faster than the Coulomb's law. This effect is known as *Debye shielding*. The characteristic length here can be shown to be λ_D, and the potential decreases with distance as

$$\phi = \frac{q}{r}\exp\left(-\frac{r}{\lambda_D}\right)$$

From this we can set a condition under which the collective behavior due to long-range interaction is statistically important. This means that each particle should feel many others, i.e. that the number of particles inside a sphere with radius λ_D is much more than one. This can be expressed by introducing the *plasma parameter* Λ:

$$\Lambda = \frac{4\pi}{3} n\lambda_D^3 \gg 1$$

In typical fully ionized fusion plasmas $\Lambda \approx 10^7$.

Events of long-range Coulomb interaction between particles of plasma are referred to as *Coulomb collisions*. Unlike in mechanical "hard-sphere" collisions of neutral particles, the interaction strength varies slowly with the distance, and in most cases particles are deflected only slightly from their initial direction. If the condition $\Lambda \gg 1$

is fulfilled, a particle constantly interacts with others, and a hard collision frequency as inverse mean time between sequential collisions does not make much sense. Instead, an effective collision frequency can be introduced, the inverse of the time of the trajectory deviation by a right angle $\pi/2$ [28]. For species with arbitrary charges eZ_a and eZ_b the collision frequency can be written as

$$\nu_{ab} = \frac{nZ_1^2 Z_2^2 e^4 \ln\Lambda}{4\pi\varepsilon_0 m^2 v^3} \tag{2.3}$$

Here, $m = m_a m_b/(m_a + m_b)$ is the reduced mass and v is the relative velocity, which is normally of the order of the thermal velocity of the lighter species. The logarithm $\ln\Lambda$ is called the *Coulomb logarithm*, it depends weakly on plasma parameters and for typical fusion plasmas $\ln\Lambda \approx 15$. Electron-ion collision frequency ν_{ei} is an important quantity and taking $v = v_{th,e}$, can be written as

$$\nu_{ei} = \frac{nZ_i^2 e^4 \ln\Lambda}{4\pi\varepsilon_0 m_e^{1/2} T_e^{3/2}} \tag{2.4}$$

This parameter defines the electrical conductivity of the plasma, high collision frequency means high resistivity. Collisions also establish thermal equilibrium within the same species, and relatively high ν ensures that the equilibrium velocity distribution function is Maxwellian. Note, that $\nu_{ee} \approx \nu_{ei}$, and ν_{ii} is about two orders of magnitude smaller, but ion thermal equilibrium is enhanced by electron-ion collisions. The latter are also responsible for the energy exchange between electrons and ions, which is particularly important when only electrons receive external heating (for example, in Ohmic heating regime of tokamak operation). The *equipartition power* reads

$$P_{ei} = 3\nu_{ei} n_e \frac{m_e}{m_i}(T_e - T_i) \sim \frac{n_e^2 Z_i^2 (T_e - T_i)}{m_i T_e^{3/2}}. \tag{2.5}$$

This collisional effect redistributes energy between species and tends to equalize electron and ion temperatures at high density.

2.1.2 Motion of charged particles in magnetic field

Charged particles in magnetic field $\mathbf{B}$ are subjected to the Lorentz force, that is

$$F_L = q\mathbf{v} \times \mathbf{B}, \tag{2.6}$$

with q the charge and $\mathbf{v}$ the vector velocity of the particles. In a uniform magnetic field the velocity component parallel to the field $v_\parallel$ is unaffected, and the perpendicular component $v_\perp$ constantly wraps around the field direction, so an arbitrary particle follows a helical trajectory, staying on a single magnetic field line (see Fig. 2.1, a). Periodic motion around a magnetic field line is usually referred to as *gyration* or *gy-*

romotion. Gyration frequency Ω_c (cyclotron frequency) and radius ρ_L (called Larmor radius) are expressed as

$$\Omega_c = \frac{qB}{m}, \qquad \rho_L = \frac{mv_\perp}{qB} \tag{2.7}$$

Due to higher mass, ions gyrate slower and with larger radius than electrons. The condition for a magnetized plasma can be then expressed as $\Omega_c \gg \nu$, i.e. particles perform many gyrations between sequential collisions. Additionally, the Larmor radius should be much smaller than a typical geometric dimension of the plasma, $\rho_L \ll L$. Both conditions should be fulfilled for all species. For convenient formulation, a small parameter δ can be introduced, which is expressed and constrained as

$$\delta \sim \frac{\rho_L}{L} \ll 1, \qquad \delta \sim \frac{\nu}{\Omega_c} \ll 1. \tag{2.8}$$

The latter condition also implies $\nu \sim v_{th}/L$, A magnetized plasma is highly anisotropic. Particles move freely along the magnetic field lines at thermal velocities, but in the transverse direction the motion is strongly constrained to the magnetic field lines. Thermal and electrical conductivities of fusion plasmas in the parallel and perpendicular directions are different by many (around ten) orders of magnitude. This anisotropy is the basic idea of the magnetic confinement of plasmas. This is also the reason why the most successful configurations are toroidal: field lines can be closed on themselves, and particles experience no edge losses.

As outlined in Sec. 1.2, the fast time scale of gyromotion can be separated from slower scales by a coordinate transformation. The exact particle position is then reformulated in terms of the position of the center of gyration (*guiding center*) and the gyroangle. One can then average over the gyroangle to remove the fast time scale. Usually in the discussion of particle trajectories we will use the guiding center position instead of the actual particle position.

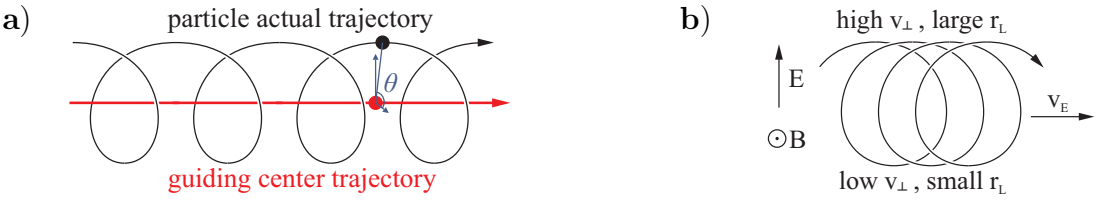

Figure 2.1: *a) Gyromotion and the guiding center-gyroangle representation. b) Mechanism of a perpendicular drift on the example of $E \times B$ drift.*

The presence of a uniform electric field modifies the particle motion. In general, it is decomposed as $\mathbf{E} = \mathbf{E}_\perp + E_\parallel$. The parallel component $E_\parallel$ can accelerate electrons and ions ($mdv_\parallel/dt = qE_\parallel$), but their ability to stream along the B field limits the magnitude of possible generated electric field due to Debye shielding effect. However, collisions make the (mainly electron) response to induced electric potential delay, so some small parallel electric field can appear. When induced by the tokamak central solenoid (see Fig. 1.1), it creates the toroidal plasma current.

The perpendicular electric field $\mathbf{E}_\perp$ exerts electric force, but because of gyromotion this leads to a net drift in the direction perpendicular to both $\mathbf{E}_\perp$ and $\mathbf{B}$. Particles are accelerated on one side of the orbit (upwards) and pass a longer distance transverse to $\mathbf{E}_\perp$, then decelerated on the other side (downwards) and pass shorter distance back to the initial phase, see Fig. 2.1, b). Important is, since both gyromotion and electric force directions are charge dependent, the electrons and ions drift together. This electric drift is called $E \times B$ *drift*, its velocity is

$$\mathbf{v}_E = \frac{\mathbf{E} \times \mathbf{B}}{B^2}, \tag{2.9}$$

where B is the magnetic field magnitude. This is similar to *the Hall effect*, which is however related to the current $\mathbf{J} \times \mathbf{B}/en$, and $J = 0$ in a plasma.

Drift velocity might arise from any force transverse to the background magnetic field, and the general expression reads

$$\mathbf{v}_F = \frac{\mathbf{F} \times \mathbf{B}}{qB^2}. \tag{2.10}$$

Note, that $\mathbf{F} = q\mathbf{E}$ is the only charge dependent force, all the others would move opposite charges in opposite directions. This can be related to magnetic field gradient or curvature. The corresponding drifts are referred to as *grad-B* and *curvature* drifts. Grad-B drift arises due to changing Larmor radius when the magnetic field magnitude is different on opposite sides of the gyration trajectory, therefore it depends also on ρ_L via the perpendicular velocity. Curvature drift is a centrifugal effect and the related "force" is $mv_\parallel^2/R$ with R the curvature radius. These two drifts can be expressed as:

$$\mathbf{v}_{\nabla B} = \frac{mv_\perp^2}{2q} \frac{\nabla B \times \mathbf{B}}{B^3}, \qquad \mathbf{v}_c = \frac{mv_\parallel^2}{q} \frac{(\mathbf{B} \cdot \nabla \mathbf{B}) \times \mathbf{B}}{B^4}. \tag{2.11}$$

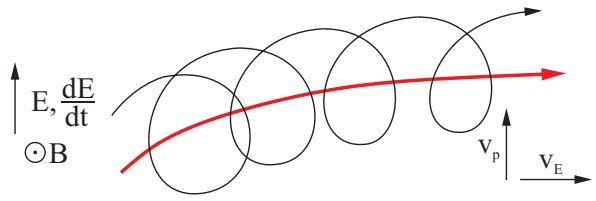

Figure 2.2: *Polarization drift: increase of $E_\perp$ magnitude in time leads to additional particle drift v_p perpendicular to v_E.*

A slow variation of $\mathbf{E}_\perp$ in time ($\omega_{\Delta E} \equiv d_t E/E \gg \Omega_c$) leads to another kind of drift, the *polarization* drift (Fig. 2.2). It is a small additional contribution to $E \times B$ drift, but along the direction of $\mathbf{E}_\perp$. When a particle follows the gyro-orbit, it undergoes acceleration and deceleration by the electric field, but since its magnitude varies in time, the two are not fully compensated, which leads to a net drift velocity. The effect is proportional to the gyroperiod, which is much longer for ions, and the drift

direction depends on the gyromotion direction, which introduces charge-dependence. The polarization drift velocity reads

$$\mathbf{v}_p = \frac{m}{qB^2}\frac{d\mathbf{E}_\perp}{dt}. \tag{2.12}$$

Unlike the others, this drift does not appear explicitly in gyrokinetic theory, but emerges on a particle level from the Poisson equation.

In slowly changing magnetic field, so that $\omega_{\Delta B} \equiv d_t B/B \gg \Omega_c$, one can find a related conserved quantity, an invariant of motion. It is the *magnetic moment*

$$\mu = \frac{mv_\perp^2}{2B} = const. \tag{2.13}$$

Technically, its variation over one gyroperiod is of the order $(\omega_{\Delta B}/\Omega_c)^2$, so it is only conserved on a relatively fast time scale, therefore it is an *adiabatic invariant*. As a consequence, the magnetic flux (magnetic field times area) enclosed by a gyro-orbit $\psi = \pi\rho_L^2 B \sim \mu$ is also adiabatically conserved. This has an important consequence on the particle motion.

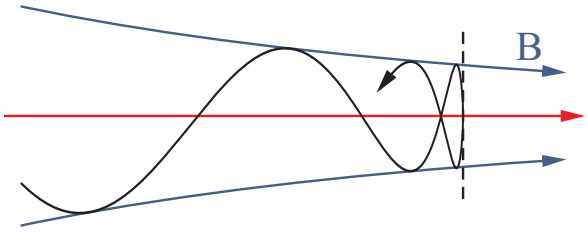

Figure 2.3: *The magnetic mirror effect: denser magnetic field lines (blue) correspond to increased magnetic field, at some point the parallel velocity vanishes and the particle is reflected.*

Assume no parallel electric field and low collision frequency, so the kinetic energy

$$T = \frac{m}{2}\left(v_\parallel^2 + v_\perp^2\right) = const. \tag{2.14}$$

Take a charged particle moving towards increasing B. From Eq. (2.13) it follows that $v_\perp^2 \sim B$, so as B increases, $v_\parallel$ is reduced. At some point all the kinetic energy consists in perpendicular motion, and a particle can not move further in the parallel direction and gets reflected back (see Fig. 2.3). This effect is called a *magnetic mirror* and can be seen similar to a gravity pendulum, but with the magnetic potential energy instead of the gravitational one. Its importance for magnetic confinement devices is discussed in Sec. 2.3.2.

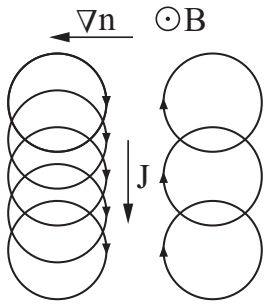

Figure 2.4: *Origin of diamagnetic current*

There exists another important kind of drift motion, which is however not a single-particle drift but a collective ef-

fect. In the presence of a perpendicular density gradient, there are more gyrating particles up the gradient than down (Fig. 2.4), leading to a finite current in the binormal direction, perpendicular to both $\mathbf{B}$ and ∇n. Finite temperature gradients have the same effect, just due to higher velocity of gyrating particles on one side. The resulting current is the *diamagnetic* or *magnetization* current $\mathbf{J}_{dia}$, which also leads to a motion of plasma particles as a whole (fluid velocity), the diamagnetic drift, opposite for electrons and ions:

$$\mathbf{J}_{dia} = \frac{\nabla p \times \mathbf{B}}{B^2}, \qquad \mathbf{v}_{dia} = \frac{\nabla p \times \mathbf{B}}{qnB^2} \tag{2.15}$$

Since a pressure gradient is always present in a confined plasma, electrons and ions are subjected to constant net motion across it in opposite directions. This plays a central role in determining the macroscopic plasma equilibrium.

2.1.3 Tokamak magnetic geometry and equilibrium

As stated in Sec. 2.1.2, a magnetized plasma is highly anisotropic, and the magnetic field with toroidally closed configuration is required to keep charged particles from rapid loss along the field lines. In practice, as described in Sec. 1.1, a combination of toroidal and poloidal magnetic fields is applied. The magnetic field of a tokamak can be expressed as

$$\mathbf{B} = \mathbf{B}_\varphi + \mathbf{B}_p = I(\psi)\nabla\varphi - \frac{1}{2\pi}\nabla\psi \times \nabla\varphi, \tag{2.16}$$

where ψ is the poloidal magnetic flux and ϕ is the toroidal angular coordinate. $I(\psi) = RB_\varphi$ is a "poloidal current function" with R the major radius of the torus. Note that $\nabla\varphi$ simply denotes the toroidal direction and B is independent on the toroidal angle, i.e. axisymmetric.

In toroidal magnetic topology, there can be defined surfaces such that for every point $\mathbf{B} \times \nabla B = 0$, i.e. magnetic field vector is tangential to the surface. Then each of them can be characterized by the poloidal magnetic flux it encloses. These are called the *flux surfaces*. By definition the flux surfaces do not intersect, they are *nested*, meaning they form a shell structure. Magnetic flux surfaces can have various shapes, so it is convenient to work in a coordinate system linked to them instead of fixed geometrical coordinates. The poloidal flux ψ or $\Psi = \psi/2\pi$ can be used as a radial coordinate, to label the given flux surface. The toroidal coordinate is usually the toroidal angle φ, and the poloidal coordinate θ, such that $\mathbf{e}_\theta = \mathbf{e}_\psi \times \mathbf{e}_\phi$ is tangential to the flux surface and orthogonal to the toroidal direction. Hence, a usual set of magnetic flux coordinates is (ψ, θ, φ).

An important characteristic quantity is the ratio of the toroidal to the poloidal magnetic flux, called the *safety factor* q. For the axisymmetric field it is expressed as

$$q = \frac{d\varphi}{d\theta} \simeq \frac{rB_\phi}{RB_\theta}, \tag{2.17}$$

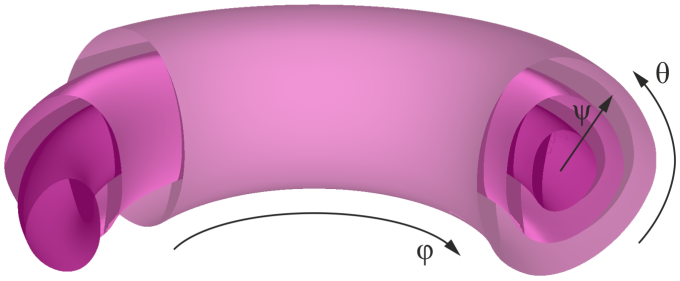

Figure 2.5: *Magnetic flux coordinates and nested surfaces.*

where the latter ratio is an approximation for circular poloidal cross-section of a tokamak, with r the local radial coordinate value and R the major radius. The factor q can be understood as the number of toroidal turns a magnetic field line on a given flux surface makes over one poloidal turn. For most flux surfaces q is irrational, meaning a field line never closes on itself, but rather densely fills the flux surface. Considering high anisotropy in parallel and perpendicular directions the poloidal and toroidal transport become as fast as parallel, while radial remains slow. Hence, many plasma parameters such as current density or kinetic pressure are constant on a given flux surface, they are *flux functions*. Surfaces of rational q are also called *resonant*, since they amplify fluctuations with integer number of wavelengths along the magnetic field line on this surface. This effect is significant only for ratios of small numbers (1,2,3), and in these cases some global instabilities may appear. The name "safety factor" refers to the condition of overall plasma stability that at the plasma edge $q \geq 2$. In a conventional tokamak $q \approx 1$ at the magnetic axis and monotonically increases towards the edge.

A magnetic field is able to confine a plasma by opposing the kinetic pressure of plasma with the magnetic pressure and the magnetic tension. At steady state the plasma is said to be in equilibrium with the magnetic field. The governing perpendicular pressure balance equation reads

$$\nabla_\perp \left(p + \frac{B^2}{2\mu_0} \right) - \frac{B^2}{\mu_0} \mathbf{b} \cdot \nabla \mathbf{b} = 0, \tag{2.18}$$

where $\nabla_\perp$ is the operator of gradient perpendicular to $\mathbf{B}$, and $\mu_0 = 4\pi \times 10^{-7}$ is the magnetic constant. Here, the gradient of kinetic pressure p is balanced by the gradient of magnetic pressure $B^2/2\mu_0$, as well as by the curvature tension of the magnetic field. In order to visualize the latter, one an imagine magnetic field lines as bent rubber straps or strings that tend to straighten back. Both confining terms arise from the $\mathbf{J} \times \mathbf{B}$ Lorenz force, where $\mathbf{J}$ is the current due to drifts (except for the electric drift) and magnetization of the plasma with finite pressure gradient. An important quantity is the ratio of plasma kinetic pressure to the magnetic pressure, β:

$$\beta = \frac{2\mu_0 p}{B^2}. \tag{2.19}$$

Ideally one wants to keep β as high as possible and achieve higher pressure with lower B (hence lower cost), but plasma can become unstable at high β. The stability limit depends on many parameters such as plasma current and plasma shape. In conventional tokamaks $\beta \approx 1\%$, while the maximum achieved in spherical tokamaks is about 40%.

In toroidally symmetric geometry the equilibrium is described by the Grad-Shafranov equation:

$$\Delta^* \psi = -\mu_0 R^2 \frac{dp}{d\psi} - \frac{1}{2} \frac{d(RB_\varphi)^2}{d\psi}, \tag{2.20}$$

with Δ^* the elliptic operator, the curvilinear spatial second derivative. Solving this equation allows to find the 2D equilibrium flux surfaces in the poloidal cross-section of a tokamak. More details on plasma equilibrium and stability can be found in [29, 30].

One important remark remains to be made here regarding the safety factor q minimum value in the plasma core. The density of induced plasma current is naturally peaked, since higher core temperature means higher electric conductivity. Consequently, q also naturally behaves monotonically. However, a very peaked current density profile drives q on the axis below unity, and plasma with $q < 1$ is unstable. The core current density aims to flatten and establish $q > 1$ everywhere, and the current density redistribution would happen abruptly. This leads to an outburst of hot plasma from inside the $q = 1$ surface outwards, which is seen as a sudden drop of core electron temperature close to the axis and a sudden increase of it around mid-radius. After a drop the core temperature starts growing again, until the next drop. This cyclic behavior is known as the saw-tooth instability, since the temperature measurement signal looks like a saw, with a period of around 10 ms. It is rather unfavorable in a tokamak reactor, so advanced operational scenarios aim at keeping $q > 1$ everywhere by driving additional toroidal current.

2.2 General transport problem

As outlined in Sec. 1.2, transport of particles, energy and momentum across the magnetic field from the plasma core to the edge is a major concern in fusion research and the main topic of this work. The spatial distributions of macroscopic quantities like density, mean velocity or temperature are defined by an equilibrium between the sources, sinks and fluxes of the transported quantities. In turn, the fluxes usually depend on the shape of the radial profiles in a non-linear way. The relationship between the kinetic profiles and the fluxes is the crucial element, which allows the determination of the kinetic profiles in the transport problem. It has to be described by a physically comprehensive model comprising collisional and turbulent transport processes.

Though there exist some differences between transport channels in tokamak plasmas (particle, momentum and heat), the transport problems can be formulated in a similar way. For a transported scalar quantity Q, like particle density, toroidal mo-

mentum or energy, the general 3D transport equation has the form

$$\frac{\partial Q}{\partial t} + \nabla \cdot \vec{\Gamma} = S_Q, \tag{2.21}$$

where Γ is the flux vector of Q and S_Q is the local source and sink term. In order to describe an equilibrium plasma state, the solution is searched for the stationary form of this equation, when the flux exactly balances the sources and sinks.

A generic decomposition of the flux term can be given as:

$$\vec{\Gamma} = -D\vec{\nabla}Q + \vec{v}Q + \vec{R}. \tag{2.22}$$

Here, the term $-D\vec{\nabla}Q$ describes diffusion, i.e. a tendency of any internal gradients to level off on a macroscopic scale. It originates from the Second Law of Thermodynamics, a law of non-decrease of entropy of a closed system. The minus sign denotes transport in the direction opposite to the gradient, to where there is less Q. The transport coefficient before the gradient term is called *diffusivity*. The term $\vec{v}Q$ describes convection, i.e. macroscopic flow of matter, and the amount of matter (or heat) transported is proportional to its local concentration. The direction of convective flux can vary for different phenomena. The third term is not directly proportional to Q or ∇Q. It is rather specific to momentum transport, where it represents the non-diagonal part of the momentum stress tensor and is called the residual stress. While the decomposition (2.22) may look arbitrary or like a first-order Taylor expansion (Fick's model), it is in fact exact for gyrokinetic turbulence in the local limit. Note, that the equation (2.22) is non-linear, as D, $\vec{v}$ and $\vec{R}$ in general also depend on Q and ∇Q, for example, via growth rates and frequencies of turbulence modes, and the solution can only be found numerically. Despite the non-linearity, for the equation (2.21) in the stationary form this solution is normally unique, since diffusive processes dominate.

Solving the transport problem means assigning the transport coefficients, sources and sinks for all transported quantities in a plasma and solving the equations of the sort (2.21). Due to the toroidal symmetry of tokamaks, as well as the fact that the transported quantities such as the electron density are flux functions, a general slow transport problem may be formulated as one-dimensional in the radial direction, concerning only the transport across flux surfaces. The coordinate system implemented in the following is (ρ, θ, ζ), where the toroidal angle $\zeta = -\phi$ and the variable used for flux surface labeling is ρ, which has the dimensionality of length, defined as

$$\rho = \sqrt{\frac{\Phi}{\pi B_0}} \quad \text{with} \quad \Phi = \frac{1}{2\pi}\int_V (\vec{B}\cdot\nabla\zeta)d^3x. \tag{2.23}$$

Here, Φ is the toroidal magnetic flux enclosed by the given flux surface. The volume V of this flux surface is defined as

$$V = \int_0^\rho d\rho \int_0^{2\pi} d\zeta \int_0^{2\pi} \sqrt{g}\, d\theta = 2\pi \int_0^\rho d\rho \int_0^{2\pi} \sqrt{g}\, d\theta, \tag{2.24}$$

with g being the determinant of the metric tensor $g = (\nabla\rho\nabla\theta\nabla\zeta)^{-2}$. Given that, the flux surface average of a function can be written down as

$$\langle Q \rangle = \frac{\partial}{\partial V} \int_0^{\rho} d\rho \int_0^{2\pi} d\zeta \int_0^{2\pi} \sqrt{g}\, Q\, d\theta = 2\pi \frac{\partial \rho}{\partial V} \int_0^{2\pi} \sqrt{g}\, Q\, d\theta. \tag{2.25}$$

The net flux Γ of a vector $\vec{h}$ through a magnetic surface can be expressed as

$$\Gamma = \int \nabla \cdot \vec{h} dV = \langle \vec{h} \cdot \nabla V \rangle = \frac{\partial V}{\partial \rho} \langle \vec{h} \cdot \nabla \rho \rangle \tag{2.26}$$

As a function of ρ, the net flux $\Gamma = \Gamma(\rho)$ can be decomposed in accordance with (2.22) and presented as

$$\Gamma(\rho) = \frac{\partial V}{\partial \rho} \left(\langle |\nabla \rho| \rangle (vQ + R) - \left\langle (\nabla \rho)^2 \right\rangle D \frac{\partial Q}{\partial \rho} \right) \tag{2.27}$$

The partial derivatives of V with respect to ρ and vice versa take into account the geometry of the flux surfaces, which is required for a correct reduction of the problem to one dimension.

The time derivative of the quantity Q by definition is taken at constant ρ. In general, if the background magnetic field varies with time, the relation between Φ and ρ also varies, and a time derivative at constant Φ is given by

$$\left.\frac{\partial Q}{\partial t}\right|_{\Phi} = \left.\frac{\partial Q}{\partial t}\right|_{\rho} + \frac{\partial Q}{\partial \rho} \left.\frac{\partial \rho}{\partial t}\right|_{\Phi} = \frac{\partial Q}{\partial t} - \frac{\rho \dot{B}_0}{2B_0} \frac{\partial Q}{\partial \rho} \tag{2.28}$$

Now that all the ingredients have been discussed, a 1D transport equation can be constructed. The exact form of it depends on the transported quantity. An example for the electron density is given below, where the notation $V' = \partial V / \partial \rho$ is used:

$$\frac{1}{V'} \left(\frac{\partial}{\partial t} - \frac{\dot{B}_0}{2B_0} \frac{\partial}{\partial \rho} \right) (V' n_e) + \frac{1}{V'} \frac{\partial}{\partial \rho} (V' \Gamma_e) = S_e. \tag{2.29}$$

In the steady state, when $\partial Q / \partial t = 0$, equations of the kind (2.29) describe a balance between sinks, sources and the radial flux. But in different transport channels the significance of each term may vary. For instance, in plasmas without NBI heating/torque input the density source is located at the edge, so the radial profile is defined by the equilibrium between convective and diffusive processes. A similar situation occurs in the momentum transport channel, but the residual part can also provide a significant contribution. On the other hand, the source of thermal energy is distributed along the radial coordinate, but the convection plays no role.

2.3 Collisional and neoclassical transport

This section discusses the nature and properties of transport processes in magnetized toroidal plasmas due to the trajectories of plasma particles and their modification by collisions.

2.3.1 "Random walk" collisional transport

Consider a gas, where a particle at thermal motion collides with other particles, and each collision randomly changes its direction of motion. This phenomenon is also known as Brownian motion. Denote λ the average distance a particle passes between two collisions (*mean free path*), and τ the average time period between two collisions. Since after each i collision the displacement Δx_i direction is random, after a large number of collisions N a particle mean displacement $\langle \Delta x \rangle = \sum_i \Delta x_i = 0$. However, the mean square distance from the initial point is finite,

$$\left\langle (\Delta x)^2 \right\rangle = \sum_i (\Delta x_i)^2 = N\lambda^2.$$

Then, after the time $\Delta t = N\tau$ the mean square distance will be

$$\left\langle (\Delta x)^2 \right\rangle = \frac{\lambda^2}{\tau}\Delta t = D\Delta t,$$

where $D = \lambda^2/\tau$ is defined as the diffusion coefficient. So, in order to find the diffusion rate, one has to identify λ and τ.

On a fast timescale the motion of charged particles in a strong magnetic field is constrained to gyro-orbits. Collisions lead to net diffusion if the center of mass of two colliding particles shifts in the perpendicular plane when the particles jump to new orbits, and its displacement is the effective λ value. Due to energy and momentum conservation and since the gyration direction is the same, a Coulomb collision of alike particles does not change their center of mass position. This means that alike particles might exchange orbits and velocity leading to energy transport, but on the average no particle diffusion occurs.

Particles of different charge gyrate in opposite directions, and the mean square displacement of the center of mass of two unlike particles colliding can be shown to be

$$\lambda^2 = 2\frac{v^2 m_r^2}{|q_1||q_2|B^2}, \qquad \text{with } m_r = \frac{m_1 m_2}{m_1 + m_2} \text{ the reduced mass.}$$

In the case of electrons and single-charged ions the mass ratio is high enough to take $m_r \approx m_e$ and $v \approx v_{th,e}$, so the expression for λ^2 becomes

$$\lambda^2 = 4\frac{m_e T_e}{e^2 B^2}.$$

Taking the effective intercollision time τ equal the inverse effective electron-ion collision frequency ν_{ei} from Eq. (2.4), one can obtain the diffusion coefficient for particle density in the form

$$D_n = 4\nu_{ei}\frac{m_e T_e}{e^2 B^2} \sim \nu_{ei} r_{L,e}^2 \tag{2.30}$$

Note that there is a single D_n for electrons and ions. Because of quasineutrality condition they diffuse at the same rate, such diffusion is therefore called *ambipolar*.

Collisional diffusion is the main mean of particle diffusion in a neutral gas or liquid. These states of matter have been studied long before the plasma, so collisional transport in a plasma is called classical. With typical fusion reactor parameters, the classical diffusion coefficient takes the value about $10^{-5}\,m^2/s$. This is five orders of magnitude lower than experimentally observed values, which are of the order of $1\,m^2/s$.

Similar approach can be used to estimate thermal diffusivity χ, which enters the expression for heat flux:

$$\mathbf{q} = -n\chi\nabla T. \tag{2.31}$$

Unlike with particle diffusion, here alike particle collisions matter, and thermal diffusivities for electrons and ions are different:

$$\chi_e = \frac{\nu_{ee}}{4}\frac{v_{th,e}^2}{\Omega_{c,e}^2} \sim \nu_{ee} r_{L,e}^2, \qquad \chi_i = \frac{\nu_{ii}}{4}\frac{v_{th,i}^2}{\Omega_{c,i}^2} \sim \nu_{ii} r_{L,i}^2 \tag{2.32}$$

By this estimation, $\chi_i \sim \chi_e\sqrt{m_i/m_e}$, and the total classical thermal diffusion is hence mostly governed by ions. For reactor conditions the classical $\chi \approx 10^{-3}\,m^2/s$, which is also much lower than experimental $1\,m^2/s$.

2.3.2 Neoclassical transport

The above considerations assumed straight magnetic field lines and ignored parallel motions of particles. In magnetic confinement devices the magnetic field lines are twisted, the toroidal magnetic field strength decreases from the torus center as $B_\varphi \sim 1/R$ (the inner side of the torus is therefore called the *High Field Side*, HFS, while the outer is the *Low Field Side*, LFS). Hence, particles do not stay pinned to a single field line but drift across the field, as described in Sec. 2.1.2. Moreover, following the parallel direction, particles experience variation of the B magnitude, and some particles may be reflected back at some point, if their parallel velocity is not high enough (the mirror effect). Particles that cannot complete a full poloidal turn are *trapped* on the outer side of the torus, while the others can *pass* to the HFS. The two fractions have clearly distinguishable transport properties.

In a helical magnetic field, a particle is subjected to both curvature and grad-B drifts (2.11), the combination of their vertical components can be written [31] using

the expression for q (2.17) as:

$$v_D = \frac{m}{2eRB_\varphi}\left(v_\perp^2 + 2v_\parallel^2\right) \sim \frac{mv^2}{2eRB_\varphi}(2 - \sin^2\alpha), \tag{2.33}$$

where $\alpha =$ is the particle *pitch angle*, defined as $\sin\alpha = v_\perp/v$. It can be shown that trapped particles have $\alpha > \alpha_{crit}$, where α_{crit} is such that

$$\sin^2\alpha_{crit} = \frac{B_{min}}{B_{max}} = \frac{1-\epsilon}{1+\epsilon}, \tag{2.34}$$

defined through the local inverse aspect ratio $\epsilon = r/R$ in the approximation of a circular cross-section. The trapped fraction can then be obtained as $f_T = \sqrt{2\epsilon}$ and for a conventional tokamak edge with $\epsilon = 0.3$ can reach as much as 75%.

The drift vertical velocity (2.33) direction depends on the particle electric charge. A passing positive ion with $v_\parallel > 0$ starting from the LFS midplane, $\theta = 0$, would shift outwards to a maximum displacement δ_p at the HFS, $\theta = \pi$, but then return to the initial flux surface when back to $\theta = 0$. If the particle charge or $v_\parallel$ sign is opposite, the shift is inward. A collision would change the particle average radial position by a step of the order of δ_p. The distance δ_p can be estimated from the drift velocity and the poloidal transit frequency ω_{tr} that takes the form

$$\omega_{tr} = \frac{v_\theta}{r} = \frac{v_\parallel}{Rq}, \tag{2.35}$$

so the average radial displacement due to the drift, given $v_\parallel \gg v_\perp$, is

$$\delta_p = \frac{v_D}{\omega_{tr}} = \frac{\left(v_\perp^2 + 2v_\parallel^2\right)}{2R\,\Omega_c} \cdot \frac{R\,q}{v_\parallel} \approx 2\frac{qv_{th}}{\Omega_c} = 2qr_L. \tag{2.36}$$

The diffusion coefficient can be computed in a similar way as in the classical case, using the effective collision frequency:

$$D_n^p = \delta_p^2\nu_{ei} = 4q^2r_L^2\nu_{ei} = 4q^2D_n^{CL} \tag{2.37}$$

Similar considerations apply to heat transport, resulting in $\chi^p \sim q^2\chi^{CL}$. Transport due to the passing particles is known as the Pfirsch-Schlüter transport.

As noted above, trapped particles transport properties are different, namely, their diffusivity is much higher than for passing particles. The reason for that is, due to lower $v_\parallel$ it takes more time to complete a full "banana" orbit, meaning a trapped particle has higher chances to undergo a collision and switch orbit. In addition, low $v_\parallel$ allows this at smaller scattering angles, so the effective collision frequency is higher than ν_{ei}. In order to compute the diffusion coefficients, one needs to know the characteristic time (or frequency) scale and the step size.

Following the same logic as before, the frequency of interest is the *bouncing*

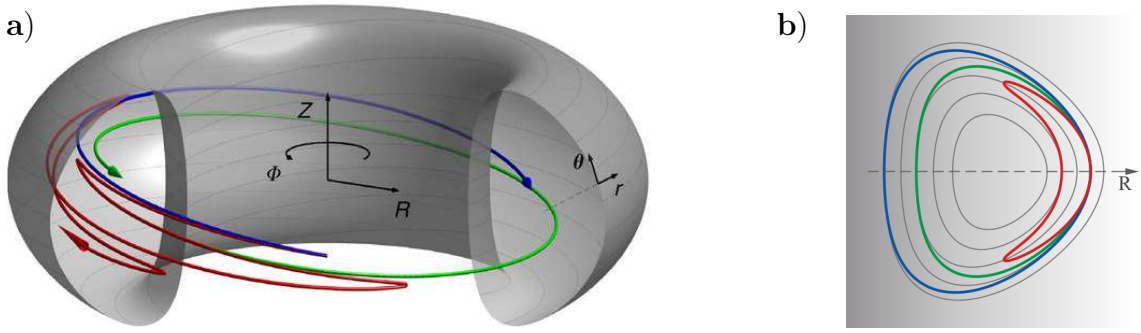

Figure 2.6: *a) Neoclassical trajectories in toroidal geometry. Blue and green lines correspond to outward and inward shift, respectively; red line shows bouncing trajectory of a trapped particle, the "banana" orbit. b) Poloidal projections of neoclassical trajectories with the same color code, grey background denotes the magnetic field magnitude.*

frequency $\omega_b = 2\pi/\tau_b$. Since $v_\parallel$ flips sign twice over the bouncing period τ_b, the average parallel velocity is roughly $\bar{v}_\parallel = v_\parallel/2$, so the average bouncing frequency is

$$\omega_b = \frac{v_\parallel}{2Rq} = \frac{\omega_p}{2}. \tag{2.38}$$

The radial step size calculation reasoning is also similar. As $v_\parallel \ll v_\perp$, one can take $v \sim v_\perp$, and the expression for the radial displacement over one half of the banana orbit becomes

$$\delta_b = \frac{\left(v_\perp^2 + 2v_\parallel^2\right)}{2R\,\Omega_c} \cdot \frac{2R\,q}{v_\parallel} \approx \frac{q\,v_{th}^2}{v_\parallel} = \sqrt{\frac{3}{2\epsilon}}\,q\,r_L \tag{2.39}$$

In order to define the effective collision frequency, one can find that the required scattering angle is of the order of $\sqrt{2\epsilon}$, and the collision frequency then $\nu_{\text{eff}} = \nu_{ei}/\epsilon$. It is now possible to compose the diffusion coefficient for trapped particles. It contains the factor f_T, as it only applies to the trapped fraction:

$$D_n^b = f_T\,\delta_b^2\,\nu_{eff} = \sqrt{2\epsilon}\,\frac{3q^2 r_L^2}{2\epsilon}\,\frac{\nu_{ei}}{\epsilon} = \frac{3}{\sqrt{2}}\,\frac{q^2}{\epsilon^{3/2}} D_n^{CL} \tag{2.40}$$

For the conditions close to plasma edge ($q = 3$, $\epsilon = 1/4$) it is about 100 times the classical collisional diffusion.

Heat diffusivities from trapped particles diffusion feature the same factor $q^2/\epsilon^{3/2}$ but different numerical multipliers:

$$\chi_e = 0.89\frac{q^2}{\epsilon^{3/2}}\chi_e^{CL}, \qquad \chi_i = 0.68\frac{q^2}{\epsilon^{3/2}}\chi_i^{CL}. \tag{2.41}$$

An important note: the argumentation above is valid for plasmas where particles can actually complete the banana orbit, i.e. the collision frequency is much lower than the bouncing frequency, $\nu_{\text{eff}} \ll \nu_b$. The ratio of these two frequencies is the

non-dimensional quantity *collisionality* $\nu_* = \nu_{ei}/\nu_b$, which scales as $\sim n/T^2$. For fusion plasmas collisionality is usually 10^{-1}-10^{-3}, so this condition is well fulfilled. If the collisionality $\nu_* \sim 1$, the trapped particles fraction is notably reduced, and the neoclassical transport occurs in the Pfirsch-Schlüter regime.

2.4 Turbulent transport

Transport due to single particle trajectories is important in many aspects, but in the conditions of significant gradients in density and temperature in the plasma core it is not dominant. These gradients present a source of free thermodynamic energy, which leads to a formation of turbulent convective structures. These turbulent vortices are very effective in mixing extended radial regions of plasma, resulting in high transport rates.

If the plasma beta is low, so that the electromagnetic effects are weak, as is the case in L-mode plasmas of AUG, the dominant turbulence is electrostatic. In the plasma core various electrostatic modes can exist. They can be differentiated by:

- The species that determine the mode dynamics: electrons or ions, which also defines the direction of mode propagation;
- The energy source they feed on: while in general it represents a gradient of the equilibrium distribution function, the actual source can be a gradient in the electron density, electron temperature or ion temperature;
- The spatial and temporal scales they occupy: typical $k_y\rho_i$ between 0.1-1.0 for ion modes and 0.3-50 for electron modes, typical frequencies of the order of few tens of kHz.
- The effect they have on the macroscopic profiles.

At the plasma edge it becomes difficult to define particular turbulent modes, as the driving gradients are so large that the non-linear dynamics prevails, and no linear structure is conserved [32]. In this work we focus on the core turbulence, and this section discusses the properties of some electrostatic modes, which belong to the class of drift wave modes.

2.4.1 Drift wave instability

Drift waves appear in magnetically confined plasmas, in both toroidal and linear geometry. It requires a pressure gradient across the magnetic field direction, which is inevitable if the plasma is purposefully confined. It can involve both parallel and perpendicular dynamics and therefore has a three-dimensional nature (unlike, for example, interchange instability, which can be considered in the perpendicular plane only).

There are several ways the drift wave instability can be realized in the toroidal geometry of a tokamak, representing various instability modes. The most common are: the ion temperature gradient mode (ITG), the electron temperature gradient mode (ETG) and the trapped electron mode (TEM). In the plasma conditions studied in this work the two crucial modes are ITG and TEM.

Basic instability mechanism

In the description of basic principles of the drift waves we assume for simplicity only a density gradient and perturbations at a constant temperature [33]. Consider plasma with the external magnetic field in z direction and a density gradient in x direction, where a small positive perturbation of ion density δn_i appears. This means higher concentration of positive electric charge and an increase of electrostatic potential by $\delta\phi$. The potential bump induces the electric field directed away from it, and $E \times B$ convection starts in the (x,y) plane around the bump (see Fig. 2.7). Electrons are attracted to the potential excess to establish the Boltzmann density distribution

$$n_e = n_0 \exp\left(\frac{e\phi}{T_e}\right), \tag{2.42}$$

and due to high anisotropy in electric conductivity the electron flow is mainly in the parallel direction z. Note, that in this picture the perturbation size $\delta x \gg \lambda_D$, while perturbations with $\delta_x \leq \lambda_D$ are immediately balanced locally. Hence, quasineutrality holds, and no significant charge separation is allowed. In this case, the perturbation amplitude

$$\tilde{n}_e = n_0 \left[\exp\left(\frac{e\phi}{T_e}\right) - 1\right] \tag{2.43}$$

can be truncated, considering $e\phi \ll T_e$, to

$$\tilde{n}_e \simeq n_0 \frac{e\tilde{\phi}}{T_e}. \tag{2.44}$$

This implies adiabatic electron response, i.e. density and potential perturbation occur simultaneously and at the same point.

The ion continuity equation in the approximation of slow parallel motion

$$\frac{\partial n}{\partial t} + u_{E\times B,x} \nabla_x n = 0 \tag{2.45}$$

can be rewritten using the definition of $u_{E\times B,x} = \nabla_y \phi / B$ and remembering the electron diamagnetic drift expression

$$u_{dia,e} = -\frac{\nabla_x n_e}{n_e} \frac{T_e}{eB}, \tag{2.46}$$

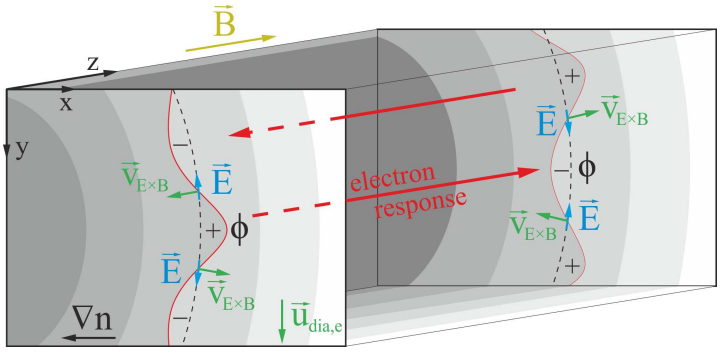

Figure 2.7: *Electron parallel dynamics connects density and potential perturbations and leads to their propagation along y at $u_{dia,e}$. Shades of grey denote density*

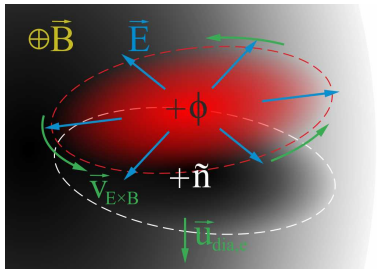

Figure 2.8: *Drift waves growth and transport mechanism with finite phase shift δ*

as well as the quasineutrality condition (2.44), eventually yielding

$$\frac{\partial n}{\partial t} + \frac{1}{B}\nabla_y \phi \cdot u_{dia,e} \frac{n_e e B}{T_e} = 0 \qquad \Longrightarrow \qquad \frac{\partial \phi}{\partial t} + u_{dia,e} \nabla_y \phi = 0. \tag{2.47}$$

Assuming a harmonic form of the perturbation, one can make the substitutions $\partial/\partial t \to -i\omega$ and $\partial/\partial y \to ik$, and rewrite the expression (2.47) as the dispersion relation for drift waves:

$$\omega \equiv \omega_{dia,e} = k_y u_{dia,e}. \tag{2.48}$$

It shows that a harmonic potential perturbation propagates in the electron diamagnetic direction, along y coordinate. This dispersion relation is actually modified by accounting for finite ion inertia and the presence of polarization drift, which leads to

$$\omega = \frac{k_y \omega_{dia,e}}{1 + k_y^2 \rho_s^2}, \tag{2.49}$$

where $\rho_s = c_s/\Omega_{c,i}$ is the *sound Larmor radius* with $c_s = (T_e/m_i)^{1/2}$ the ion sound speed in the plasma. In this model, the wave is undamped and the perturbation amplitude is constant.

In order for the instability to grow the adiabatic approximation should be broken, and finite dissipation (for instance, due to collisions or Landau damping) should be taken into account. This results in a delay or positive phase shift between the potential and the density bumps, which formally modifies the expression (2.44) for each wavelength k into

$$\tilde{n}_{e,\mathrm{k}} \simeq N \frac{e\phi_{\mathrm{k}}}{T_e} \left(1 - i\delta_{\mathrm{k}}\right). \tag{2.50}$$

Here, the potential maximum is delayed from the density maximum. The $E \times B$ flow hence carries more density towards the maximum (see Fig. 2.8), and the perturbation

grows as $e^{\gamma_k t}$ with the (linear) growth rate

$$\gamma = \frac{\nu_{ei} m_e}{k_\parallel^2 T_e} \omega_{dia,e}^2 k_y^2 \rho_s^2 \tag{2.51}$$

Large perturbation amplitude also leads to significant net transport of density down the density gradient, across the magnetic field. The transport mechanism is closely related to the instability growth mechanism.

Ion temperature gradient mode

The ITG mode is a type of a drift wave instability in magnetically confined plasmas, defined by ion dynamics and driven by the gradient of the ion temperature. The toroidal ITG mode is one of the most important sources of turbulent transport in tokamaks, as it forms meso-scale structures that efficiently mix up significant regions of plasma, transporting energy and particles towards the plasma edge. It is the main contributor into ion heat conductivity, also affecting the electron channel, especially at high density. Fig. 2.9 presents the poloidal structure of a simulated global linear ITG potential perturbation. It shows an ideal mode structure, but the real non-linear turbulent eddies of the ITG mode are much smaller.

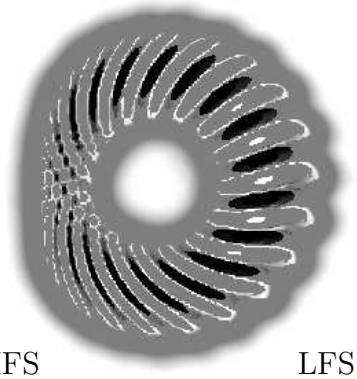

Figure 2.9: *ITG linear global potential perturbation (Y.Camenen, NF 2011).*

We can obtain the system of equations that describes ITG dynamics in a tokamak by taking velocity moments of a gyrokinetic equation for the fluctuating part $f = F - F_M$ of the ion distribution function (a detailed derivation can be found in [34]):

$$\frac{\partial f}{\partial t} + \vec{v}_{gc} \cdot \nabla f + \vec{v}_E \cdot \nabla f - \frac{\vec{b}}{m} \left(\mu B + \nabla \mathcal{E}\right) \frac{\partial f}{\partial v_\parallel} = -\vec{v}_E \cdot \nabla F_M - \vec{v}_{gc} \cdot \frac{Ze \nabla \langle \phi \rangle}{T} F_M \tag{2.52}$$

with the gradient of the Maxwellian decomposed as

$$\nabla F_M = \left[\frac{1}{L_n} + \left(\frac{\mathcal{E}}{T} - \frac{3}{2} \right) \frac{1}{L_T} \right] F_M \tag{2.53}$$

Neglecting the non-linear term $\vec{v}_E \cdot \nabla f$ and making further simplifying assumptions (simple magnetic geometry, no centrifugal effects, ..), we arrive to a set of fluid equations:

$$\begin{aligned}
\hat{\omega}\tilde{n} + 2\tilde{n} + 2\tilde{T} + 4(U + \hat{k}_\parallel)\tilde{u} &= \phi \left[\tfrac{R}{L_n} - 2 \right], \\
\hat{\omega}\tilde{u} + 4\tilde{u} + 2(U + \hat{k}_\parallel)\tilde{n} + 2(U + \hat{k}_\parallel)\tilde{T} &= \phi \left[U' - 2(U + \hat{k}_\parallel) \right], \\
\hat{\omega}\tilde{T} + \tfrac{4}{3}\tilde{n} + \tfrac{14}{3}\tilde{T} + \tfrac{8}{3}(U + \hat{k}_\parallel)\tilde{u} &= \phi \left[\tfrac{R}{L_T} - \tfrac{4}{3} \right], \\
\text{and the quasineutrality condition: } Z\tilde{n}\tau &= \phi.
\end{aligned}$$

Here Z is the ion charge, $\tau = T_e/T_i$, U and U' are the toroidal velocity and its gradient, and the following notation is used:

$$\frac{1}{L_x} = \frac{\nabla x}{x}; \quad \hat{\omega} = \frac{\omega}{\omega_D}, \quad \hat{k}_\parallel = -\frac{k_\parallel v_{th}}{4\omega_D} \text{ with } \omega_D = -\frac{k_\theta T}{eBR}, \quad \phi = \frac{e\tilde{\phi}}{T_e}.$$

Assuming no parallel dynamics, i.e. $\tilde{u} = 0$, and $Z = 1$, we simplify this system to relate only the density and temperature fluctuation to the gradients:

$$\begin{aligned} \hat{\omega}\tilde{n} + 2\tilde{n} + 2\tilde{T} &= \phi\left[\tfrac{R}{L_n} - 2\right], \\ \hat{\omega}\tilde{T} + \tfrac{4}{3}\tilde{n} + \tfrac{14}{3}\tilde{T} &= \phi\left[\tfrac{R}{L_T} - \tfrac{4}{3}\right], \\ \tilde{n}\tau &= \phi. \end{aligned}$$

Now, in order to understand the basic dynamics of the ITG mode, we will take only the dominant terms, so that the system is reduced to

$$\begin{aligned} \hat{\omega}\tilde{n} + 2\tilde{T} &= 0, \\ \hat{\omega}\tilde{T} - \tfrac{R}{L_T}\phi &= 0, \\ \tilde{n}\tau &= \phi. \end{aligned}$$

The mechanism is as follows: the initial temperature perturbation generates a perturbation in density, that is neutralized by passing electrons, which implies an electrostatic potential. The $E \times B$ flow mixes cold and hot regions, which enhances the initial perturbation.

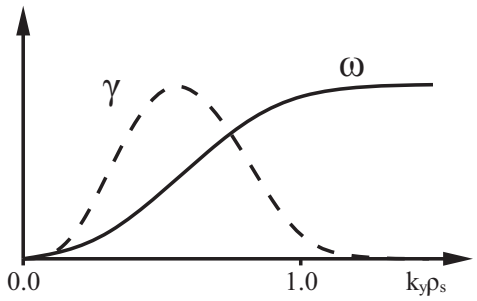

Figure 2.10: *Linear growth rate γ and real frequency ω of a typical ITG mode*

The ITG mode normally forms turbulent vortices of the size of few ion Larmor radii in the poloidal cross-section, $k_y\rho_i \approx 0.1 - 1$. Above the higher limit $k_y\rho_i \approx 1$ the turbulent motion is smeared out by faster ion gyration, below the lower limit $k_y\rho_i \approx 0.1$ the eddies are damped by the Landau damping mechanism and also can be easily split into smaller structures.

A similar mechanism exists for the electrons, giving rise the the ETG mode, which occupies the range of spatial scales from $k_y\rho_i \approx 10$ to the electron Larmor radius scale. This mode contributes substantially to the electron heat transport channel at $T_i/T_e > 1$, which does not happen in Ohmically heated plasmas studied in this work.

Here, the ETG drives only around 1% of the total electron heat flux, and hence is of no particular interest.

Trapped electron mode

The TEM mode is another type of instability in magnetically confined plasmas. It is driven by both electron temperature and density gradients, and in low-β plasmas represents the most important energy transport channel for electrons. It occupies the k_θ domain similar to the ITG mode, but propagates in the opposite poloidal direction. The TEM mechanism is also similar to that of the ITG. The latter owes its properties to the mass of ions, that makes them slow in the parallel direction. Electrons are much lighter and faster, but on the average this is valid only for the passing particles. Trapped electrons bounce along the "banana" orbits (magnetic mirror effect, see Fig. 2.6) back and forth, and while their mean square parallel velocity $< v_\parallel^2 > \sim v_{th}^2$, the mean parallel velocity $< v_\parallel >= 0$. This makes them as slow (on the average) as the ions, giving rise to a similar instability mechanism. As in the ITG case, Fig. 2.11 shows an ideal linear mode structure in the poloidal plane.

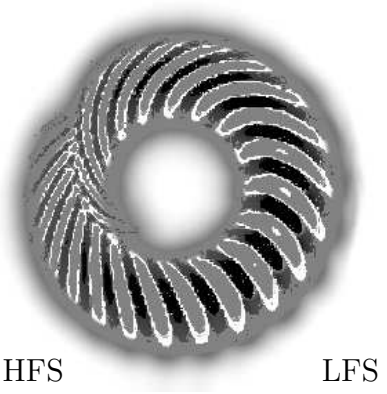

Figure 2.11: *TEM linear global potential perturbation (Y.Camenen, NF 2011).*

The system of equations for the TEM is obtained in the same way as that for the ITG. We take the velocity moments of the gyrokinetic equation in a linearized form and assume harmonic perturbations in density and temperature. Then for a generic species j:

$$\begin{aligned} \left(-\omega+\omega_{Dj}\right)\tilde{n}_j+\omega_{Dj}\tilde{T}_j-\tau_j\omega_{Dj}\left[\tfrac{1}{2}\tfrac{R}{L_n}-1\right]\phi &= 0, \\ \left(-\omega+\tfrac{7}{3}\omega_{Dj}\right)\tilde{T}_j+\tfrac{2}{3}\omega_{Dj}\tilde{n}_j-\tau_j\omega_{Dj}\left[\tfrac{1}{2}\tfrac{R}{L_T}-\tfrac{2}{3}\right]\phi &= 0. \end{aligned}$$

The quasineutrality condition with f_t the fraction of trapped electrons reads:

$$n_i = n_{et} + n_{ep} \;\Rightarrow\; \tilde{n}_i = f_t\tilde{n}_e + (1-f_t)\phi,$$

where for the passing electrons we assume $\tilde{n}_e = \phi$.

In total, we have 5 equations with 5 unknown variables [35]. In order to focus on the TEM only, we assume no ion temperature fluctuations $\tilde{T}_i = 0$, and switch off the corresponding equation. The resulting system reads:

$$\begin{aligned} -\hat{\omega}\tilde{n}_i-\tfrac{1}{\tau}\tilde{n}_i+\left[\tfrac{1}{2}\tfrac{R}{L_n}-1\right]\phi &= 0, \\ -\hat{\omega}\tilde{n}_e+\tilde{n}_e+\tilde{T}_e+\left[\tfrac{1}{2}\tfrac{R}{L_n}-1\right]\phi &= 0, \\ -\hat{\omega}\tilde{T}_e+\tfrac{7}{3}\tilde{T}_e+\tfrac{2}{3}\tilde{n}_e+\left[\tfrac{1}{2}\tfrac{R}{L_{T_e}}-\tfrac{2}{3}\right]\phi &= 0, \\ \tilde{n}_i-f_t\tilde{n}_e-(1-f_t)\phi &= 0. \end{aligned}$$

Here, the frequency $\hat{\omega}$ is normalized to the electron drift frequency ω_{De}. Two driving terms can be seen: the density gradient and the electron temperature gradient. The properties of modes driven by the two mechanisms are slightly different, but normally a combined effect takes place. TEM driven by the temperature gradient can create inward particle flux, which leads to high density peaking factor $n_e(core)/\bar{n}_e$. It will be shown in the following sections that this peaking effect may be an indicator of TEM activity. The typical range of TEM spatial scales are similar to those of ITG, but not restricted by the ion Larmor radius.

There are some other fundamental differences between TEM and ITG modes. In the low-k limit the ITG is subjected to Landau damping that limits its growth rate. In turn, TEM is not affected because of zero mean parallel velocity of trapped electrons. On the other hand, TEM strongly depends on the fraction of deeply trapped electrons f_T (i.e. those following the banana orbits for a sufficiently long time), hence it is very sensitive to plasma collisionality. If the collision frequency is of the order of the bouncing frequency or higher, f_T decreases and the TEM mode is stabilized. In addition, trapped electrons tend to pump up the ITG mode, so it is stronger at higher trapped fraction.

2.4.2 Transport driven by microinstabilities

The mechanism of transport by turbulent eddies can be understood from Fig. 2.8: the convective cell of circulating $E \times B$ flow connects regions of plasma with different density and temperature. The inward and outward fluxes are unbalanced, so on the average plasma is transported down the pressure gradient.

In general, the radial convective particle and heat fluxes in the presence of a fluctuating electrostatic potential can be defined locally as

$$\Gamma = \left\langle \int \mathrm{d}^3 v \, \tilde{f} \, \frac{\mathbf{b} \times \nabla \tilde{\phi}}{B} \cdot \mathbf{e}_\rho \right\rangle, \qquad Q = \left\langle \int \mathrm{d}^3 v \, \mathcal{E} \, \tilde{f} \, \frac{\mathbf{b} \times \nabla \tilde{\phi}}{B} \cdot \mathbf{e}_\rho \right\rangle, \tag{2.54}$$

where tilde marks the fluctuating part, $\mathcal{E}$ is the kinetic energy and $\langle . \rangle$ denotes ensemble averaging over a small spatial domain and some characteristic time of few fluctuation periods. The net radial flux can then be obtained by integrating over a flux surface. Note that the contribution from magnetic field fluctuations can be considered negligible in the case of low-β L-mode plasmas, which are simulated in this work.

It can be shown that the turbulent flux is proportional to density and temperature gradients, and can be characterized by a diffusion-like law. Taking, for example, the expression for the particle flux Γ (2.54) and rewriting it as

$$\Gamma = \left\langle \frac{ik\tilde{\phi}^*}{B} \tilde{n} \right\rangle = \langle \tilde{v}_{E,r} \tilde{n} \rangle \,, \tag{2.55}$$

we can make use of the continuity equation $\omega \tilde{n} + \nabla \cdot \tilde{v_E} n = 0$ and the incompressibility

condition $\nabla \cdot \tilde{v_E} = 0$ to obtain the relation $\tilde{n} = \tau_c \tilde{v}_E \nabla n$ with τ_c the correlation time of a turbulent vortex. Substitution of it to the formula for Γ yields

$$\Gamma = -\left\langle \frac{k^2 \tilde{\phi}^2}{B^2} \tau_c \right\rangle \nabla n = -D \nabla n, \tag{2.56}$$

where the expression D involves averaging over all turbulent scales over the flux surface. A similar approach is applicable to the heat flux, which appears to be proportional to the temperature gradient. In general, the fluctuating part of the distribution function is proportional to the gradient of the equilibrium distribution (2.53), due to the $E \times B$ flows in the case of turbulent transport or the magnetic drifts in the case of neoclassical transport.

It is useful to introduce some reference diffusivities similar to those used in classical transport theory, and then express turbulent diffusion in their terms. If the actual diffusion equals a reference one with some constant factor, it is said that it follows this particular scaling. The first one is the *Bohm diffusivity*

$$D_B = \rho_s^2 \Omega_{c,i} = \frac{T_e}{eB}, \tag{2.57}$$

first observed experimentally (to a numerical factor) by David Bohm and colleagues in 1949. Technically, it describes diffusion with characteristic step size of one Larmor radius ($\rho_s = m_i v_{th,e}/qB$ is the so-called sound Larmor radius, since it contains ion mass and electron velocity, similar to the expression for ion sound speed) in a characteristic time of one gyroperiod. Another diffusivity scaling can be obtained by using the time step proportional to the inverse growth rate of the turbulence, $\gamma \sim c_s/a$. Considering that $\rho_s = c_s/\Omega_{c,i}$, one arrives to

$$D_{GB} = \rho_s^2 \Omega_{c,i} \frac{\rho_s}{a}, \tag{2.58}$$

with $a \gg \rho_s$ being some characteristic scale length (plasma minor radius, logarithmic gradient of density or temperature) used for normalization. It is called *gyroBohm diffusivity* as it is the Bohm diffusivity reduced by one normalized gyroradius. It appears naturally when solving linearized kinetic equation for the distribution function in the local limit.

By comparing expressions (2.32), (2.41) and (2.58) one finds the approximate ratio of neoclassical and turbulent heat diffusivities

$$\frac{\chi_{NC}}{\chi_{GB}} \sim q^2 \nu_{ii} \frac{a}{c_s}, \tag{2.59}$$

and for typical tokamak parameters $\chi_{NC}/\chi_{GB} \ll 1$.

2.4.3 Scale separation

Strongly magnetized fusion tokamak plasma exhibits various types of dynamics on a wide range of spatial and temporal scales. The fastest time scales are of the order of

10^{11} Hz, these are the plasma frequency ω_p and the electron cyclotron frequency Ω_c (a little lower is the ion cyclotron frequency, $\sim 10^9$ Hz, which also relates to the fast scale), therefore they govern quasineutrality preservation and gyromotion. The scales of orbit frequencies are 2-3 orders of magnitude slower, and the collision frequencies are slower by another 2-3 orders, $\sim 10^3$-10^4 Hz. Frequencies about 10 Hz and lower present the so-called confinement time scale, at which global profiles of pressure and other quantities establish. Theoretical treatment of all scales at once is impractical, as different processes dominate at different frequencies and length. The example of effective averaging over gyromotion has been given above, and a somewhat similar approach can be used to separate other scales from one another.

However, unlike the exact gyrokinetic dimensional reduction method, others are approximate and rely on the small parameter δ (perturbation theory approach), similar to that given by Eq. (2.8). Generally, it is set as

$$\delta \sim \frac{\rho_L}{L} \sim \frac{\omega}{\Omega_c} \sim \frac{v_d}{v_{th}} \ll 1. \tag{2.60}$$

Here, ω corresponds to the confinement time scale ($\nu_c/\omega \sim 1$ is assumed), and v_d is the velocity related to $E \times B$ and magnetic drifts. The distribution function can then be expanded as $f = f^{(0)} + f^{(1)} + f^{(2)} + ...$, where $f/f^{(n)} \sim \delta^n$. Equations for different scales can then be solved independently (scale separation principle).

In neoclassical theory it is assumed that the time variation of the distribution function is of the order δ^2, so no fast evolution of local parameters is allowed. The zero-order term $f^{(0)} = F_M\left(n(r), T(r), \phi(r)\right)$ is the equilibrium Maxwellian and has no dependence on the parallel coordinate s, therefore describing plasma pressure and electrostatic potential as flux functions. First order equations for the kinetic equation moments govern the plasma pressure equilibrium and flows of plasma parameters within flux surfaces that are divergence-free. It is only the second order of the δ expansion that introduces radial fluxes and time variation of flux functions, so by the theory construction the radial transport occurs at time scales comparable to the confinement time scale.

If one allows for faster time variations, so that $\partial f/\partial t \sim \delta$, one comes to an interplay between drifts and radial fluxes, as they now appear at the same scale. This brings up waves with typical frequencies in the range of 10^4 Hz, which can become unstable and grow in amplitude, leading to turbulence formation. This phenomenon is knows as *drift waves*, and it is the most effective transport channel in the core of low-β tokamak plasmas. The plasma edge may feature other important transport mechanisms, such as MHD modes, but this work is mainly focused on core transport.

Different treatment of time evolution of the distribution function in the two theories does not automatically make one of them wrong. It is simply the scale separation principle in action: each phenomenon is considered at its typical scale. Here, it is assumed that neoclassical motion does not affect the microinstabilities and vice versa, and in fact there have been studies that found the interaction between the two small

in the local limit [36]. Hence, in this work the turbulent and neoclassical transport are summed up linearly.

2.5 Transport modeling software

Modeling transport in a plasma requires solution of a system of transport equations of the type (2.21) and equations that relate the transported quantities to each other. The primary quantities of interest are densities and temperatures of each particle species. The plasma current density and flow velocity are also simulated, although not as routinely since they do not enter directly in the prediction of plasma confinement (but they can affect it through interaction with turbulence). Despite the general problem being three-dimensional, parallel and perpendicular directions can be decoupled due to the high anisotropy of magnetized plasma. In a tokamak, finite pitch angle of magnetic lines projects the parallel direction to both toroidal and poloidal directions, so transport over a flux surface is much faster than that between flux surfaces (radial). This makes only the radial transport relevant for plasma confinement, which is the main (energy) transport-related issue. This applies to the regions of plasma within closed flux surfaces, while in the open field lines region (scrape-off layer near the walls) parallel transport becomes of the first importance.

The transport modelling may be approached in two different ways. If the aim is to compute fluxes from given (e.g. measured) profiles, the modeling is *interpretive*. In this case no sophisticated physical model is necessary, direct solution of the system of equations gives the fluxes. This might be useful, for example, when determining parametric dependencies of the transport coefficients. If, on the other hand, both profiles and fluxes are to be computed from first principles given basic discharge conditions (engineering parameters like the magnetic field, total current, average density, heating power or fueling), the modeling is called *predictive*. One then needs an independent physical transport model able to predict fluxes given the plasma conditions, and the solver of transport equations returning profiles upon providing the fluxes from the model. This process is iterated until the profiles and fluxes are consistent with each other, i.e. in equilibrium.

In this work the predictive modeling is specifically addressed, with interpretative modeling using for comparison. The transport solver used is the ASTRA system, which embeds the TGLF transport model for turbulent transport. Neoclassical transport coefficients are obtained either by means of analytic expressions as described in [37] (in the energy confinement modeling), or with NEO code (in the intrinsic rotation modelling). These tools are discussed in detail below.

2.5.1 ASTRA

ASTRA stands for Automated System for TRansport Analysis, it is a software which started to be developed in the late 1980s in the Kurchatov Institute and still continues

nowadays. It is a flexible programming system able to create numerical codes for predictive or interpretative transport modeling, stability analysis and experimental data processing. ASTRA organizes the transport code in a modular manner, which makes it easy to include and exclude pieces of physical description and construct a model adjusted for a given problem. Its main operational regime is interactive, so that the user can observe the plasma parameters as they evolve, and adjust the simulation parameters or even the model in the process.

With the focus on transport processes in the plasma core (confined regions), the three-dimensional problem is effectively reduced to one radial dimension. However, the magnetic equilibrium geometry is at least two-dimensional, as tokamaks feature approximate toroidal symmetry. The basis of a transport code built by ASTRA consists of a 2D equilibrium solver and a set of 1D transport equations with closure conditions (totalling to the so-called 1.5D system of equations). The coordinate systems implemented in the equilibrium solver is cylindrical (r, φ, z) with the polar axis aligned to the major axis of a torus. Transport equations are formulated in the coordinate system (a, θ, ζ) with the toroidal angle $\zeta = -\varphi$, linked to the magnetic geometry, which covers only the confined plasma, up to the separatrix. More details can be found in [38, 39]

The basic set of transport equations includes equations for the electron density, electron temperature, ion temperature and the poloidal flux ψ:

$$\begin{cases} \dfrac{1}{V'}\left(\dfrac{\partial}{\partial t} - \dfrac{\dot{B}_0}{2B_0}\dfrac{\partial}{\partial \rho}\right)(V' n_e) + \dfrac{1}{V'}\dfrac{\partial}{\partial \rho}\Gamma_e = S_e, \\ \dfrac{3}{2}(V')^{-5/3}\left(\dfrac{\partial}{\partial t} - \dfrac{\dot{B}_0}{2B_0}\dfrac{\partial}{\partial \rho}\right)\left[(V')^{5/3} n_a T_a\right] + \dfrac{1}{V'}\dfrac{\partial}{\partial \rho}\left(q_a + \dfrac{5}{2}T_a\Gamma_a\right) = P_a, \\ \sigma_{\parallel}\left(\dfrac{\partial \psi}{\partial t} - \dfrac{\rho \dot{B}_0}{2B_0}\dfrac{\partial \psi}{\partial \rho}\right) = \dfrac{J^2 R_0}{\mu_0 \rho}\dfrac{\partial}{\partial \rho}\left(\dfrac{\Gamma_2}{J}\dfrac{\partial \psi}{\partial \rho}\right) - \dfrac{V'}{2\pi\rho}(j_B S + j_C D), \end{cases} \tag{2.61}$$

where $a = e, i$ is the species label. The electron flux Γ_e and heat fluxes q_e and q_i are total fluxes through a surface of constant ρ. In the basic set there is no equation for the ion density, sine it is usually defined by the electron density, ion charge and the impurity content (if any) via the quasineutrality condition. The set can also be expanded to include separate equations for impurity density or fluid plasma velocity.

The fluxes in Eq. 2.61 are expressed in terms of thermodynamic forces and a matrix of transport coefficients:

$$\begin{pmatrix} \dfrac{\Gamma_e}{n_e} \\ \dfrac{q_e}{n_e T_e} \\ \dfrac{q_i}{n_i T_i} \end{pmatrix} = -\left\langle (\nabla\rho)^2 \right\rangle V' \begin{pmatrix} D_n & D_e & D_i & C_n \\ \chi_n^e & \chi_e & \chi_i^e & \chi_E^e \\ \chi_n^i & \chi_e^i & \chi_i & \chi_E^i \end{pmatrix} \begin{pmatrix} \dfrac{1}{n_e}\dfrac{\partial n_e}{\partial \rho} \\ \dfrac{1}{T_e}\dfrac{\partial T_e}{\partial \rho} \\ \dfrac{1}{T_i}\dfrac{\partial T_i}{\partial \rho} \\ \dfrac{E_{\parallel}}{B_p} \end{pmatrix} \tag{2.62}$$

In order to solve the direct problem at least some of the transport matrix terms must be computed. Of particular interest are the "diagonal" terms D_n, χ_e and χ_i, as well as the particle pinch term C_n. In this work the neoclassical contribution to these quantities is computed with simplified analytical expressions (in the energy confinement study) and with the neoclassical code NEO treated as an external module for ASTRA; the contributions from turbulent transport are computed by the TGLF transport model, also implemented as a module.

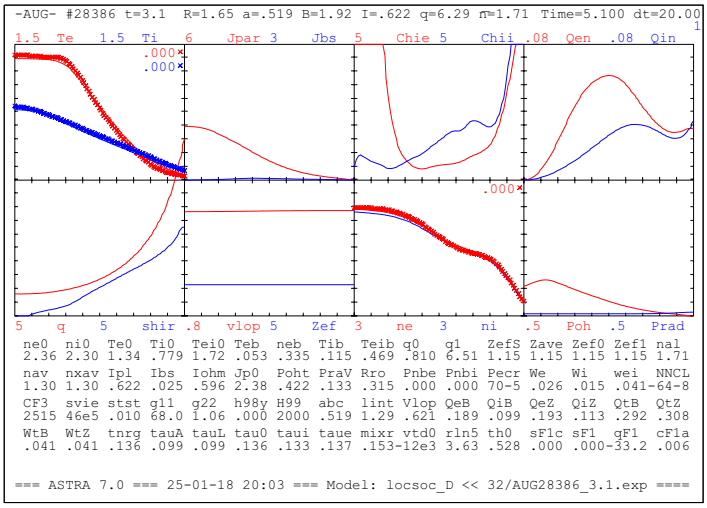

Figure 2.12: *Example of ASTRA interface window without control buttons*

The operational interface of ASTRA in the interactive regime is shown in Fig. 2.12. It is a window presenting the key simulation parameters (simulated shot number and time, major and minor radii of the plasma, toroidal magnetic field, plasma current, maximum safety factor and the average electron density), up to 128 radial profiles of various characteristics and a list of single-valued quantities. It allows to modify the graphic mode, control values of variables and constants, as well as some other features. In Fig. 2.12 the first of the total eight adjustable pages of figures is shown, featuring (top row of figures) the profiles of simulated electron and ion temperatures plotted against the measurements (shown with crosses); the total current and its bootstrap fraction; electron and ion heat conductivities; electron and ion heat fluxes; also (bottom row of figures) the safety factor and the magnetic shear; loop voltage and the effective charge; electron and main ion density against the experimental electron density; the Ohmic heating and radiated power profiles.

2.5.2 TGLF

TGLF stands for Trapped-Gyro-Landau-Fluid, this is a quasi-linear gyrofluid transport model [40, 41], an improved version of previously successful GLF23 model [42]. It is based on a system of velocity moment equations of the gyro-averaged kinetic equation. The closure at the level of the heat fluxes (3rd order moment) is performed, which

effectively keeps kinetic effects, in particular, Landau damping. The model treats trapped and passing electrons together in a unified system of equations and couples both to the ions, which makes it valid from the lowest wavenumbers of the trapped ion mode up to the electron Larmor scale. Adjusted and verified against gyrokinetic codes (GKS, GYRO), it offers comparable accuracy at much lower computational costs, allowing for fast and comprehensive transport simulations.

The basic linearized electrostatic gyrokinetic equation has the form [43]:

$$\left(\frac{\partial}{\partial t} + v_{\parallel}\nabla_{\parallel} + i\omega_{dv}\right)\tilde{F} = \left(-v_{\parallel}\nabla_{\parallel} - i\omega dv + i\omega_{*}^{T}\right) F_0 J_0 \frac{e\tilde{\phi}}{T}. \tag{2.63}$$

Here, $\tilde{F}(X_{gc}, E, \mu)$ is the fluctuating gyro-averaged distribution function, $\tilde{\phi}$ is the electrostatic potential. On the left hand side, $\partial\tilde{F}/\partial t$ is the mode frequency $-i\omega\tilde{F}$, the term $v_{\parallel}\nabla_{\parallel}\tilde{F}$ represents the parallel transport, $i\omega_{dv}\tilde{F}$ includes perpendicular transport due to curvature and centrifugal drifts. The equilibrium $E \times B$ drift is not included in the equation, it enters the solution directly by turbulence spectrum modification (shift in k_r). The fluctuating $E \times B$ drift acting on the $\tilde{F}$ is a non-linear term absent in a quasi-linear formulation. The right hand side contains the parallel and perpendicular electric forces, as well as the drive term, where ω_{*}^{T} is a combination of Maxwellian gradients R/L_n and R/L_T. The Bessel functions J_0 account for finite Larmor radius (FLR) effects.

The transport model is formulated in terms of parallel and total velocities ($v_{\parallel}$, v). Six moment equation are derived from Eq. 2.63 for each species, for the density n, parallel velocity $u_{\parallel}$, parallel $P_{\parallel}$ and total P_T pressure, parallel $Q_{\parallel}$ and total Q_T energy fluxes. For trapped particles, only three moments are kept (n^t, $P_{\parallel}^t$, P_T^t), with the parallel gradient operator and the odd moments set to zero. The system is closed by expressing higher order moments as linear combinations of the listed six, with coefficients obtained through fitting to non-linear gyrokinetic simulation results. The saturated amplitudes for the fluctuating fields are expressed via a saturation rule, which is built using the linear growth rates and frequencies (it is quite complex, details can be found in [41]).

The model validity

Quasi-linear approach is based on the assumption that the non-linearity that determines the turbulent motion is small, and the linear structure of the turbulent modes retains. This assumption has been tested with non-linear gyrokinetic simulations and proven valid for the plasma core, inside 0.8-0.9 of the minor radius [44–46]. The modes can grow linearly at the time scale of the inverse growth rate γ, and the mixing length transport scaling $\chi \sim \gamma/k_{\perp}^2$ holds. The linear flux spectra are converted to non-linear using fitting coefficients, the quasi-linear weights, defined for each scale to match the results of non-linear simulations.

The fluid approximation is compensated by the accurate account for wave-

particle resonances in the closure of the equations. The kinetic effects are derived analytically and computed numerically, so that the kinetic response is recovered by the gyrofluid model. The fact that TGLF fluxes are very close to those computed with GYRO confirms the validity.

2.5.3 NEO

The NEO code [47] provides a first principles based calculation of the neoclassical transport coefficients directly from solution of the distribution function. It solves a hierarchy of equations derived by expanding the drift-kinetic equation (DKE) in powers of $\rho_{*,i}$, the ratio of the ion gyroradius to the system size, giving an exact solution for the usual second-order neoclassical fluxes. NEO extends previous numerical studies by including the self-consistent coupling of electrons and multiple ion species and the calculation of the first-order electrostatic potential via coupling with the Poisson equation.

The DKE for the total distribution function $f_a(\epsilon, \mu)$ is taken in the form

$$\frac{\partial f_a}{\partial t} + (v_\parallel \mathbf{b} + v_D + v_E) \cdot \nabla f_a - \frac{Z_a e}{m_a}(v_\parallel \mathbf{b} + v_D) \cdot \nabla \Phi \frac{\partial f_a}{\partial \epsilon} + \dot{\mu} \frac{\partial f_a}{\partial \mu} = C_a + S_a \quad (2.64)$$

with a the species index, S_a containing sources of particles, momentum, energy; C_a is the nonlinear collision operator $C_a = \sum_b C_{ab}(f_a, f_b)$, which couples the dynamics of all species entering the simulation. The collision operator is taken in its full form.

Particle and heat diffusion coefficients can be computed in an easier way, with the expressions derived in [37], but NEO is used due to its ability to compute such quantities as the poloidal velocities of ion species.

Note, that while the drift-kinetic and gyrokinetic equations may look similar, there is a fundamental difference between them, namely that the distribution function that enters the latter is gyro-averaged. This introduces the effects of finite Larmor radius of particles, which has a particular importance on turbulent motion by effectively smearing the fluctuations on the scales smaller than the Larmor radius. This makes the gyrokinetic theory superior to the drift-kinetic formulation. But the use of gyrokinetic equation for neoclassical transport calculations is much more computationally demanding, and since the FLR effects have little importance for neoclassical trajectories, the DKE is a good option when solving for the neoclassical transport.

Chapter 3

Experimental basis

The simulations performed in this work are based on experimental measurements of plasma in the ASDEX Upgrade tokamak. This chapter provides an overview of the machine, as well as gives detailed information on plasma conditions, measurements methods and results.

3.1 ASDEX Upgrade

ASDEX Upgrade (AUG) is a medium-size tokamak with tungsten plasma facing components located in Garching near Munich, Germany. The geometric parameters of AUG are: plasma major radius $R = 1.65\,\mathrm{m}$, minor radius $a = 0.5\,\mathrm{m}$, plasma volume $V = 14\,\mathrm{m}^3$. The maximum achievable toroidal magnetic field on the axis $B_t = 3.1\,\mathrm{T}$, the maximum induced plasma current $I_p = 1.4\,\mathrm{MA}$, however the usual operation parameters are 2.5 T and 1 MA. The electron density can reach $10^{20}\,\mathrm{m}^{-3}$. The maximum power of plasma heating is 31 MW that includes ECRH (4 MW), ICRH (6 MW) and NBI (20 MW) auxiliary heating systems, supplementing the inductive Ohmic heating (up to 1 MW). This makes the highest P/R ratio, i.e. power over the linear size, among the tokamaks worldwide.

The set of plasma diagnostics installed at AUG is very diverse, the total number exceeds 30. These exploit various operating principles: spectroscopy (active and passive, from radio to soft X-ray), reflectometry, interferometry, motional Stark effect polarimetry, penetrating measurements with Langmuir probes, bolometry, thermography, visible-light cameras and some others.

3.2 The AUG Ohmic Database

Ohmic plasma discharges in tokamaks exhibit a rich phenomenology with complex parameter dependencies and present a challenging area for theoretical description. A series of L-mode discharges with predominantly Ohmic heating has been conducted in AUG over the recent years. Those featured various values of the toroidal magnetic

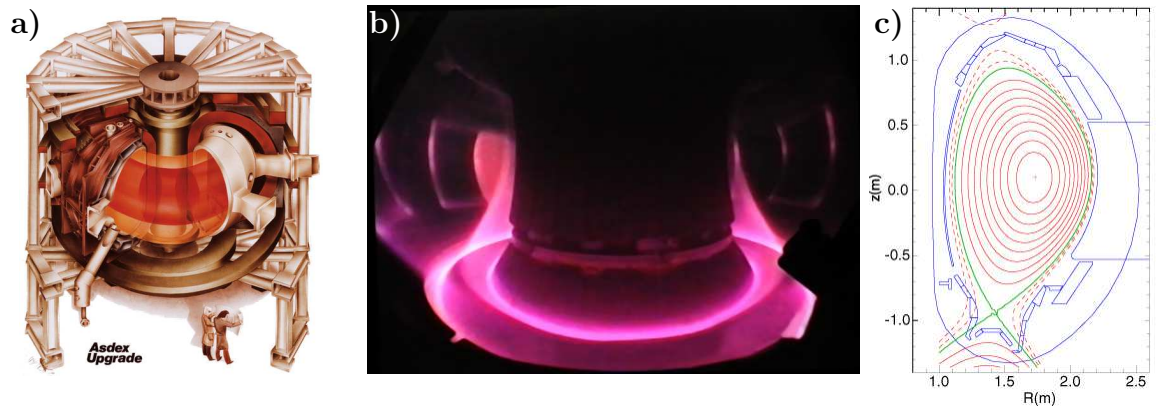

Figure 3.1: *a) Sketch of the ASDEX Upgrade tokamak: plasma, plasma vessel, magnetic field coils and support structure [IPP, J. Weber]. b) Visible light from plasma during a discharge in AUG. Central regions of the plasma emit in the invisible spectrum range up to soft x-ray. c) Poloidal cross-section with flux surfaces*

field and the plasma current and had the electron density varied over the discharge duration. Hence, a significant area of plasma parameter space has been covered. Measurements of the most relevant plasma parameters, such as electron density, electron and ion temperatures, impurity content and toroidal rotation velocity in those conditions, provide a good experimental basis and modelling reference for the study of transport processes. The measurements data has been organized into a database, the ASDEX Upgrade Ohmic Database [13], which consists of 186 data points from 14 different discharges.

Initial analysis of the database has identified two particularly convenient subsets of data: 17 points with $B_t = 1.91\,\mathrm{T}$, $I_p = 0.62\,\mathrm{MA}$ and n_e ranging from $1.1 \times 10^{19}\,\mathrm{m}^{-3}$ to $3.1 \times 10^{19}\,\mathrm{m}^{-3}$; 16 points at $B_t = 2.51\,\mathrm{T}$, $I_p = 1.04\,\mathrm{MA}$ with n_e increasing from $1.5 \times 10^{19}\,\mathrm{m}^{-3}$ to $4.6 \times 10^{19}\,\mathrm{m}^{-3}$, which is the highest density of the whole database. The choice to have pairs of discharges provides a more complete density variation than possible within a single plasma shot. Both subsets have linear and saturated phases of the energy confinement time, as well as alternating sign of the core toroidal rotation direction. Using these for detailed analysis allows us to investigate not only how the considered transport phenomena depend on the density, but also their scaling with the plasma current, which has been reported from various experiments.

3.2.1 Collected measurements

The information contained in the database is acquired with various plasma diagnostics. This section shows how the data is treated before it is used in the simulations.

The electron density comes from the IDA, Integrated Data Analysis that combines measurements of DCN laser interferometry, lithium beam spectroscopy, O-mode reflectometry and optional Thomson scattering spectroscopy. The reason for such combination is that the lithium beam diagnostics has high spatial resolution at the plasma

edge and in SOL, but its use is limited to these regions. On the other hand, laser interferometer measures the line integrated density over the whole plasma volume, but its spatial resolution is constrained by the number of active laser beams. IDA combines the two to gain from the advantages of both, it also interpolates the interferometry reconstructed profile for higher spatial resolution in the plasma core. Its temporal resolution is also very high, 1 μs.

Even if the operational conditions are steady, the plasma itself is not, being subjected to various types of fluctuations. The most prominent one in L-mode is that related to sawteeth instability that affects mainly T_e and slightly n_e. Since those fluctuations are much faster than the transport time scale, it is reasonable to average the profiles over several sawteeth periods. However, the operational conditions vary with time, so a too long averaging period would mix different plasma regimes. Here, with the sawteeth period of around 30 ms, the averaging period equal to 40 ms is used. The effect of the sawteeth on the plasma profiles is taken into account in the simulations.

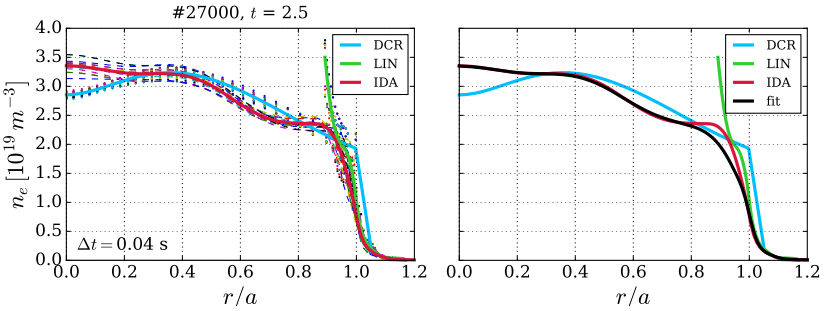

Figure 3.2: *Averaging over several measurements for each of DCR, LIN and IDA diagnostics (left) and comparison of raw and fit IDA profiles (right)*

An example of profiles handling is given in Fig. 3.2. The left plot shows several individual profiles of DCR (laser interferometry), LIN (lithium beam spectroscopy) and IDA in the temporal range $t = 2.5 \pm 0.02$ s and the averaged profiles. LIN profile is consistent with other diagnostics around the last close flux surface ($r/a = 1$), but overestimates the density amplitude further inside the plasma. DCR profiles are not particularly reliable, since they are a result of the reconstruction of integrated measurements. It is also a little misaligned at the edge, resulting in a shift of the profile "pedestal" outside of the separatrix. Unfortunately, more reliable diagnostics that can return the whole density profile (such as fast swept reflectometer) were not available at the time of these experiments. IDA density profiles feature the core region elevated over DCR and the edge "step" as an artifact of the DCR-LIN polynomial combination due to LIN overestimation. While in H mode such step may occur naturally due to the edge transport barrier, it is not expected in L mode plasmas, which is supported by higher quality measurements in more recent discharges [48]. In order to eliminate this step, a smoothing has been applied on IDA profiles, by means of the linear low-pass

filter `scipy.signal.filtfilt` of the `scipy` library for Python. The smoothing parameters are chosen such that the profiles are modified as little as possible except for the problem edge region. The resulting "fit" is shown in the right plot of this figure, together with diagnostic profiles averaged over 0.04 s period.

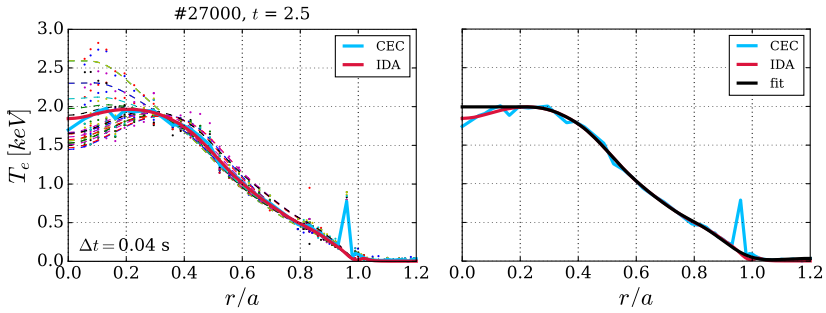

Figure 3.3: *Averaging over several measurements for CEC and IDA diagnostics (left) and comparison of raw and fit IDA profiles (right)*

The results of similar approach to T_e data of the integrated data analysis tool are presented in Fig. 3.3. The main data source in this case is the electron cyclotron emission (ECE) diagnostics marked as CEC. From the left plot one can clearly see the saw-tooth temperature oscillations. Averaged profile features a small dip at the axis, which is flattened out for simplicity (fit in the right plot), especially because there is no mechanism in the model to produce hollow temperature profiles. It may be caused by the sawteeth activity and some central radiation, however no significant radiation from the plasma core is observed.

Ion temperature and toroidal rotation velocity measurements are performed with charge exchange recombination spectroscopy (CXRS) diagnostics. It is based on the exchange of electrons between impurity species ions of plasma and injected neutral atoms (with NBI heating system) of the main plasma species (deuterium). Boron has been selected as the signal species, since the tokamak wall is routinely boronized (coating of tungsten walls with boron leads to the plasma confinement improvement), so boron is always present in the plasma. An injected neutral atom penetrates deep into the plasma and exchanges an electron with a boron ion. This electron falls to lower energy levels and emits radiation at certain wavelengths. Spectroscopy of radiation from a specific point of intersection of the NBI beam with a flux surface can give the temperature (half-width of the Gauss peak) and the velocity (Doppler shift of the peak) of boron at that flux surface. Deuterium temperature is assumed equal to boron temperature, since the temperature equilibration time between different ion species is much shorter than the transport time scale. The toroidal velocity of deuterium can be computed assuming neoclassical velocity difference, as discussed in Sec. 5.3.

However, while it helps measure the temperature, NBI introduces some significant heating power, so the temperature rises. It also allows to measure the rotation velocity, but introduces a lot of torque, which leads to plasma acceleration. In order to reduce these effects and in general influence the plasma as little as possible,

NBI is shot in short blips when used for diagnostic purposes only. Each blip lasts for $\sim 15\,\mathrm{ms}$, and the intervals between the blips are around $0.3\,\mathrm{s}$. A series of 1 to 5 CXRS measurements (the exposure time can be different) is performed during each blip, which is necessary to reconstruct the velocity profile of unperturbed plasma by back-extrapolation of measured velocity profiles (the technique is described in [13]). The effect on ion temperature is normally rather small, so a simple averaging over the single series can be made. An example of such approach is shown in Fig. 3.4. A combination of two diagnostics is used for the T_i: CEZ (core, toroidal view) and CPZ (edge, poloidal view). The toroidal velocity measurements are obtained with CEZ only. Colored dots and lines show the measurements in three sequential CXRS measurements. Thick black line is then the resulting profile obtained with averaging for T_i and backward extrapolation for V_ϕ.

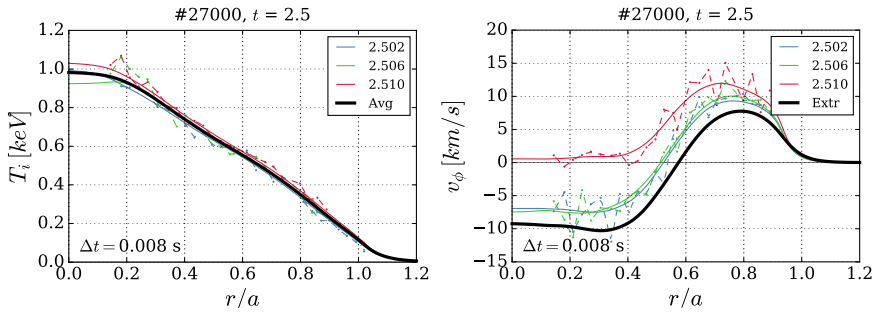

Figure 3.4: *Ion temperature averaged (left) and toroidal velocity back-extrapolated (right) from three sequential NBI blips*

In the lower current cases there are 5 sequential measurements available for profile reconstruction in both discharges, but during the shot #27001 only a single measurement per blip was done, meaning no extrapolation of the velocity profile is possible. A workaround may be to notice that each blip shifts the profile by 2-3 km/s on average, and add an artificial shifted profile after the existing one. An example is presented in Fig. 3.5, which compares two similarly shaped velocity profiles. On the left, three blips are given, while on the right there is one real measurement and one artificial. The difference between the extrapolation result and the first blip profile is very similar in both cases. When the simulation results are presented (Sec. 5.4), the experimental profiles used as a reference are produced with real measurements only, and the simulated profiles representing the discharge #27001 are lower then the measurements, roughly coinciding with the artificially obtained profiles shown here.

Another experimental quantity necessary for transport simulations is the so-called effective charge

$$Z_{\mathrm{eff}} = 1 + \frac{1}{n_e} \sum_i n_i Z_i (Z_i - 1), \tag{3.1}$$

where the summation goes over all species with Z_i being the ionization degree (ion charge). The contribution increases quadratically with the atomic number, but the

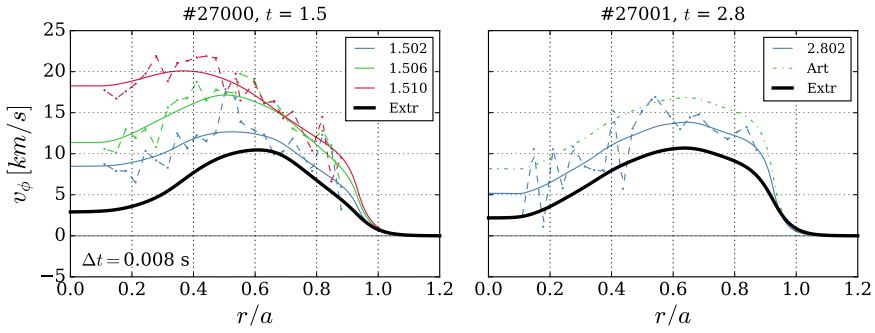

Figure 3.5: *Toroidal velocity profile extrapolated from three real NBI blips (left) compared to a similarly shaped profile made using one artificial shifted profile (right). Note that the two correspond to the lowest and the highest density in the high current scan.*

concentration of heavy ions is normally rather low, and they are usually not fully ionized at moderate plasma temperatures. The most straightforward way to compute the effective charge is given by the expression (3.1), i.e. by knowing concentration densities of all ion species, or at least the major ones. Alternatively, one can exploit the fact that Z_{eff} affects, for example, plasma electric conductivity and the amount of synchrotron radiation, so its averaged value can be obtained from the loop voltage (and known plasma current) or from bolometric measurements of the bremsstrahlung. Unfortunately, the bremsstrahlung measurements are often corrupted by reflections, and low-Z impurity measurements by CXRS are not always available in discharges using NBI blips only to measure plasma rotation. On the other hand, the loop voltage is routinely measured with high temporal resolution.

During the selected discharges the available Z_{eff} measurement methods did not prove absolutely reliable and consistent at each data point. Therefore, it has been decided to develop a scaling law of Z_{eff} as a function of the plasma current I_p and the mean electron density n_e, using all available data. Considering the importance of Z_{eff} for the turbulence regime, introducing a simple smooth function instead of scattered data points is intended to reduce the overall uncertainty for the turbulence simulations.

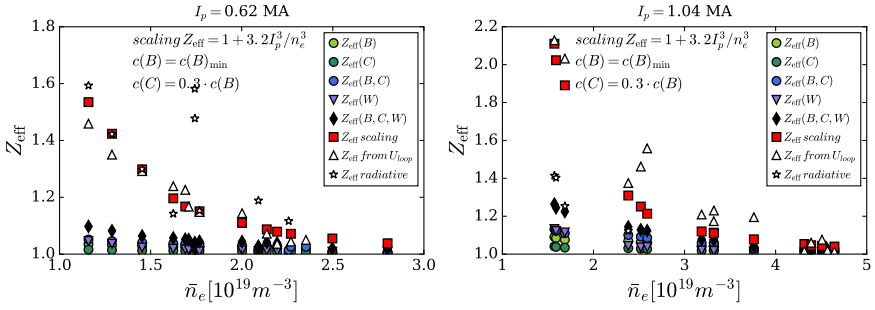

Figure 3.6: *Zeff estimated with various methods and the proposed scaling, for both data subsets*

Figure 3.6 summarizes the available measurements analysis and requires some

clarification. $Z_{\text{eff}}(X)$ is the effective charge computed from measured concentration of X ions. Both carbon and boron concentrations are minimum values measured with CXRS, but carbon concentration measurements were less reliable, so it is approximated as 30% of boron. Tungsten is estimated from radiation spectrum measurements, "radiative" Z_{eff} comes from bolometric data. Estimation from the loop voltage U_{loop} makes use of the Spitzer resistivity formula

$$\eta_S = \frac{\pi Z e^2 m^{1/2} \ln \Lambda}{(4\pi\varepsilon_0)^2 T^{3/2}} \tag{3.2}$$

with a modification due to neoclassical parallel transport included. All the data sets show direct proportionality to the plasma current and inverse – to the electron density. The estimation from combined impurity content is somewhat lower than what bolometry and loop voltage suggest, but it only provides the minimum value. A fit to the data has been found in the form

$$Z_{\text{eff}} = 1 + 3.2 I_p^3 / n_e^3, \tag{3.3}$$

with I_{p} the total plasma current in MA and $\bar{n}_{\text{e}}$ the line averaged electron density in $10^{19} m^{-3}$. It is valid for both data subsets and is used throughout this work.

Another point that Fig. 3.6 suggests is that boron is the most abundant impurity, since it contributes the most to Z_{eff}. Hence, boron was chosen as the only impurity species in the simulations, because having more species increases the computational costs significantly.

3.2.2 Data subset parameters

As specified previously, the data available from the database include profiles of electron density, electron and ion temperature and boron toroidal velocity, as well as values of the magnetic field, plasma current and the effective charge Z_{eff}. This section presents and discusses some important trends of the listed parameters for the chosen subsets of data: shots #28386, #28243 with $I_p = 0.6\,\text{MA}$ and #27000, #27001 at $I_p = 1.0\,\text{MA}$. The two will be referred to as low and high current case, respectively.

Fig. 3.7, (*a*) shows six profiles of electron density versus the normalized geometric coordinate r/a, as it evolves during the shots at the high current. Sub-figures (*b, c, d*) present the corresponding profiles of electron and ion temperatures and the toroidal velocity. The legend marks profiles by shot number and time slice. With the increase of mean density the electron temperature gradually decreases, so the electron pressure stays roughly constant, while ion temperature shows almost no variation at low density, followed by a slight decrease at higher densities. Such behavior can be explained in terms of the energy exchange between electrons and ions, which is proportional to the electron density. Electrons gain energy by the Joule heating, while ions are only heated by electron-ion collisions, so in the core always $T_e > T_i$ (outside $r/a \approx 0.8$ in Ohmic

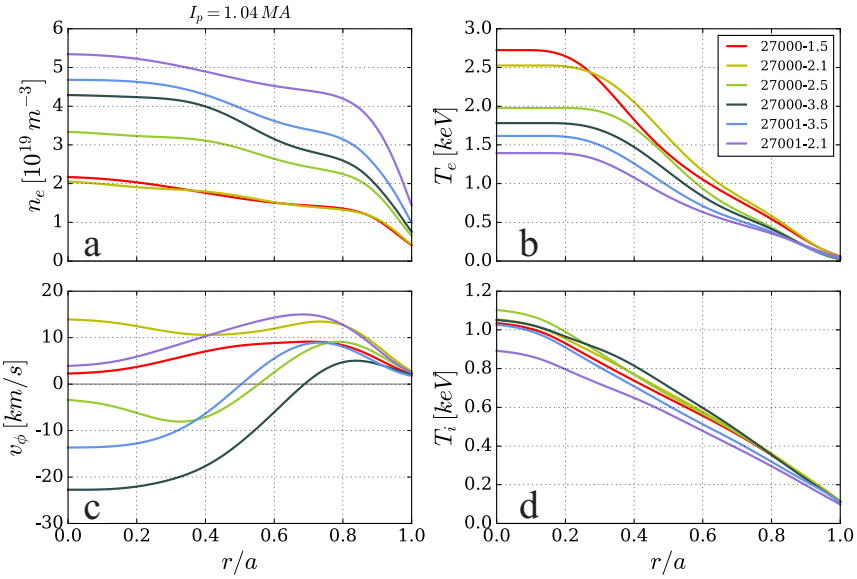

Figure 3.7: *Plasma profiles at* $I_p = 1.0\,\mathrm{MA}$

plasmas $T_i > T_e$ due to edge radiative losses and different stiffness of electron and ion transport). With the density increase, electrons transfer more energy to the ions, which keeps T_i constant at decreasing T_e. However, at high density T_e is reduced even farther and since the core $T_i/T_e < 1$, the ion temperature decreases.

The toroidal rotation velocity profile exhibits a lot of variation: it is all positive (co-current) at low density, then the core rotation reverses its direction to counter-current as n_e increases, but at even higher density the core rotation reverses back to co-current. Edge velocity stays rather the same slightly co-current, so what drives the core velocity direction change is the varying velocity shear (radial gradient) around the mid-radius.

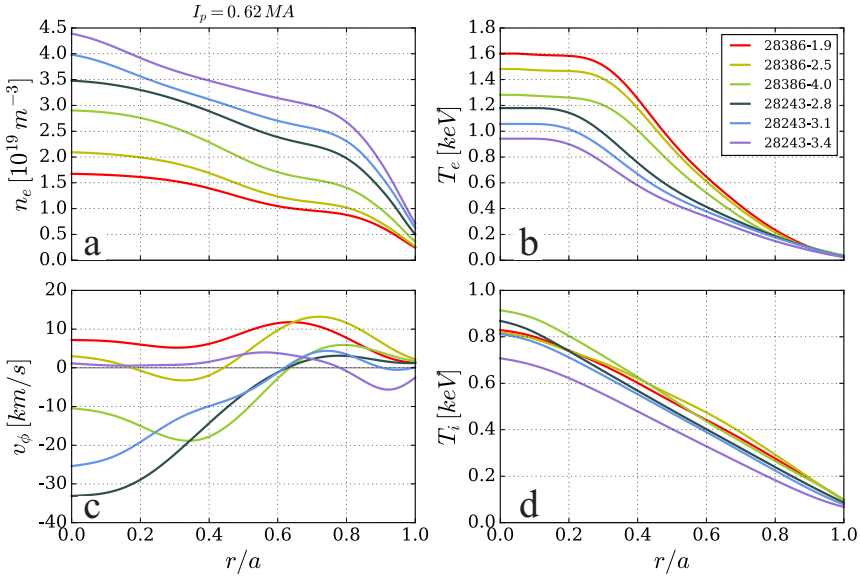

Figure 3.8: *Plasma profiles at* $I_p = 0.6\,\mathrm{MA}$

In the low current case (Fig. 3.8) the picture is very similar, but the density and

temperature ranges are shifted to lower values, which is natural as the Ohmic heating power is also lower. Another notable difference is the change in edge rotation direction at high density.

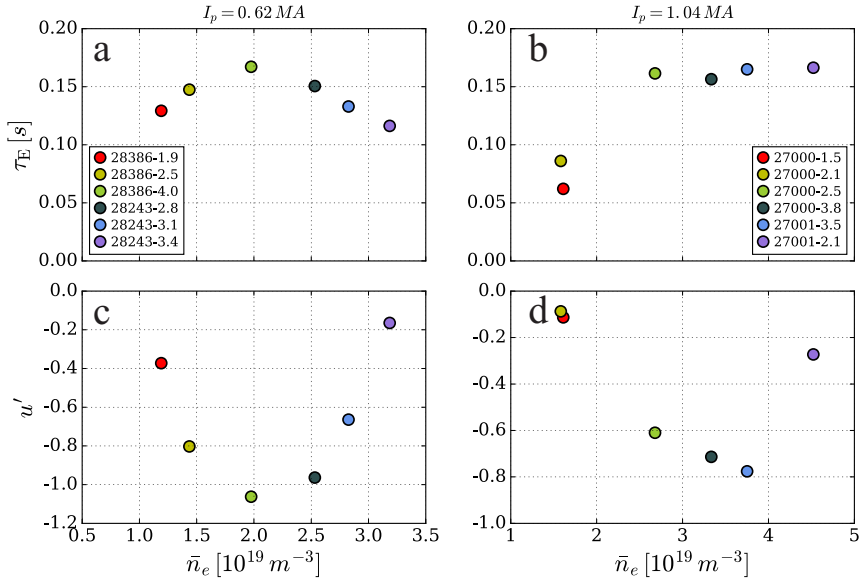

Figure 3.9: *Energy confinement time and normalized rotation gradient as functions of mean electron density*

Fig. 3.10 brings up the two major problems related to L-mode Ohmically heated plasmas on the example of the two data subsets under discussion. The first one in the energy confinement time τ_E trend transiting from linear to saturated phase (a and b). The second is the core toroidal rotation direction double reversal, shown in terms of normalized toroidal velocity gradient $u' = -Rv'_\phi/v_{th,i}$ averaged over the mid-radius, $r/a = 0.4..0.6$ (c and d). The problems consist in finding a satisfactory explanation of the observed plasma behavior.

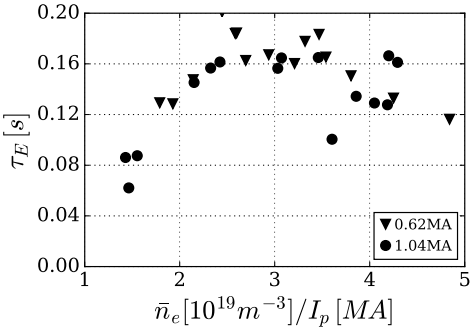

Figure 3.10: *Energy confinement time for both low and high current versus n_e/I_p*

Note, that the critical density for both phenomena is about the same value and depends on the plasma current. In fact, the low and high current cases can be combined into a single figure, when plotted against the ratio n_e/I_p, and the trends seem to coincide well. The same applies to the effective charge scaling, which suggests that all these processes are somehow related.

The density and current-dependent representation is phenomenological and may not reflect the physical nature of the phenomena. These "engineering" parameters might act through affecting the electron temperature and collisionality, which plays an essential role defining the transport regime, or the heat flux and impurity concentration that impact turbulent transport properties. Either way, the problems posed are related to energy and momentum transport, and finding solutions requires thorough transport modelling of the plasmas in L-mode conditions.

Chapter 4

Energy confinement time modelling

This chapter presents the setup and results of transport simulations of L-mode Ohmic plasmas presented in the previous section, with deuterium as main plasma species, in ASDEX Upgrade geometry. The experimental basis of the modeling consists of two subsets comprised of two discharges each, which have been described described in detail in the previous section.

This part of the work (published as [49]) aims at investigating the link between turbulence regime (TEM or ITG-dominant) and plasma energy confinement. It has been suggested [6–8] that the energy confinement time τ_{E} scales linearly with mean electron density (Linear Ohmic Confinement regime, LOC) when turbulence is dominated by TEM, and saturates (Saturated Ohmic Confinement regime, SOC) when ITG dominates the transport. In order to confirm it or provide an alternative explanation, one needs to be able to directly relate the turbulence mode shift to the confinement regime transition. It is extremely difficult to actually "measure" the presence of TEM or ITG in a plasma [9], but it is possible to make such relation in simulations. Model parametrization with real plasma conditions then allows us to make conclusions regarding the real turbulent state, provided the turbulence model is correct.

The TGLF transport model is an appropriate tool for such an application. It returns turbulence characteristics and fluxes of PDF velocity moments given the local plasma conditions. The heat conductivities χ can be compared to those computed from experimental profiles by the power balance relations (for the species a):

$$\chi_a(\rho) = -\frac{625\, Q_a}{n_a \dfrac{\partial T_a}{\partial \rho} \left\langle (\nabla \rho)^2 \right\rangle \dfrac{\partial V}{\partial \rho}}, \quad \text{with } Q_a = \int_0^{\rho} \left[P_{in} - P_{out}\right] \frac{\partial V}{\partial \rho} d\rho, \tag{4.1}$$

for validation and reference. In the expressions (4.1) the radial coordinate $\rho = \sqrt{\Phi/\pi B_0}$ with Φ the toroidal flux enclosed by the given flux surface and B_0 the reference magnetic field, and V is the volume enclosed by the flux surface. In order to support the self-consistent modelling, three sets of data are compared. One comprises the experimental measurements of AUG plasmas and is referred to as "Data". Another one consists of the results of ASTRA simulations with experimental kinetic profiles and

plasma boundary, and with heat transport coefficients obtained from the power balance calculations, see formula (4.1). This one is referred to as "PB" that stands for power balance. The results of ASTRA simulations with the TGLF module and the self-consistent evolution of the kinetic profiles, yet with experimental plasma boundary (separatrix coordinates), form the third data set, which is labeled "TGLF". Both types of ASTRA simulations feature free evolution of the current density distribution, and most of the model parameters are the same.

4.1 Model description

ASTRA solves transport equations that determine the temperature and density profiles, as explained in Section 2.5.1. The self–consistent evolution of energy transport coefficients and plasma temperature profiles saturates when the heating is balanced by outward radial heat fluxes, while for the density, for which no particle source is present in the core, it results from the balance of diffusion and convection. Turbulent transport coefficients (heat conductivities χ_e and χ_i, particle diffusivity D_n and convection coefficient C_n) are computed by TGLF every fifth time step on the basis of evolving kinetic profiles in ASTRA, and are then used to compute the profiles, resulting in full self–consistency. Neoclassical transport coefficients are computed with analytical expressions [37]. The two sets of transport coefficients are then summed up linearly.

The electron diffusion and convection coefficients are balanced by a particle source at the edge, which is expressed by a gas puffing and ionization model. The puffing rate adjusts itself, so that the line integrated electron density stays equal to the experimental value. Boron is used as the only impurity species as it is intrinsic to AUG plasmas, where the wall undergoes frequent boronizations. Mean boron concentration follows the scaling $Z_{\mathrm{eff}} = 1 + 3.2 I_p^3/\bar{n}_e^3$ with I_p expressed in MA and $\bar{n}_e$ in $10^{19} m^{-3}$, and is further discussed below. The density of main plasma ions and boron impurity ions is computed from the quasineutrality condition and Z_{eff} according to the scaling.

The boundary condition for the electron density is set at the separatrix by an outflow proportional to the local density value. Boundary conditions for the temperatures are set at the separatrix, as well. Since the error bars on the edge temperature measurements are of the order of the measured values, we used a scaling that approximates the experimental values, see fig 4.1. It consists in inverse proportionality of the edge electron temperature to the edge electron density that has been shown valid [59], and $T_{i,\rho=1} = 2T_{e,\rho=1}$.

The plasma boundary shape is defined by elongation $\kappa = 1.62$ and triangularity $\delta = 0.15$. The idea was to make the simulation result depend only on the basic discharge parameters (B_t, I_p) and the average electron density $\bar{n}_e$, and not on particular experimental data, in order to eliminate measurement uncertainty variation and minor effects contributions. The implemented generalization of boundary conditions gives

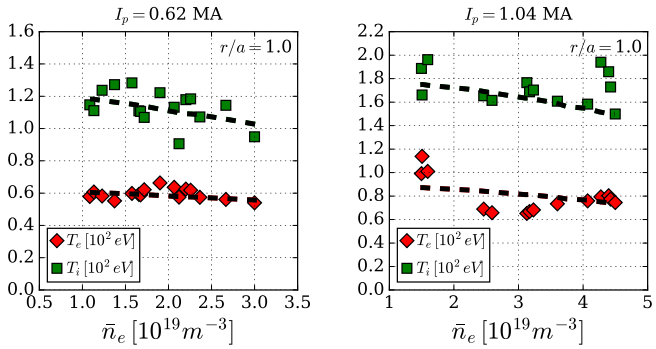

Figure 4.1: *Electron and ion temperature boundary conditions at the plasma edge. The dashed curves represent the scaling used in the modeling.*

good agreement with the measurements in the whole range of investigated plasma conditions.

The main power source is the Ohmic heating computed as

$$P_{Ohm} = I_p^2/\sigma = I_p U_{loop}, \tag{4.2}$$

with σ the neoclassical electric conductivity [50]. In the high current discharges the Ohmic power it varies in the range 0.8-1.0 MW, with the low current it is about 0.5 MW. In addition, the high current discharges feature a minor pulsed ECR heating with averaged $P_{\mathrm{ECRH}} \approx 130\,\mathrm{kW}$. Both power sources transfer energy to the electrons, while the ions gain energy via the collisional equipartition (Eq. 2.5). The effect of turbulent equipartition [51] is also included, which is however counter-directed.

The model for radiated power assumes tungsten as the main source of radiation and follows [52]:

$$P_{rad,W} = n_e n_W L_Z, \tag{4.3}$$

where $L_Z = L_Z(T_e)$ is the tungsten cooling factor, which is a polynomial fit to experimental data. The tungsten concentration is estimated to be of the order of 10^{-4} from the bolometric measurements, varying with the density as Fig. 3.6 suggests. The estimated values amount to $20 - 40\%$ of the Ohmic power (see Fig. 4.11), which is about two times higher than those measured by soft x-ray diagnostics (more details in Sec. 5.2), however the sensitivity of the confinement time in this regard has been found to be rather weak. Due to the low concentration, tungsten is considered a trace impurity and does not enter the quasineutrality condition, therefore it does not affect the densities of other species or the turbulence properties relevant for the interpretation of the simulation results. Bremsstrahlung radiation is also accounted for in the form

$$P_{br} = 5.06e^{-5} Z_{\mathrm{eff}} n_e^2 T_e^{1/2}\,\mathrm{MW}, \tag{4.4}$$

while the cyclotron radiation is found to be very small and therefore neglected.

ASTRA also computes the magnetic equilibrium and the current diffusion. The current density profile evolves freely to establish an equilibrium, which is distinguished

by a flat profile of the loop voltage. A model for the sawtooth instability (current density redistribution, similar to [53]) is used, in order to limit the current profile peaking and the subsequent decrease of q in the core. The radial position of the $q = 1$ surface is defined by the equilibrium solver, it is usually located at $r/a \approx 0.2$. The accompanying central flattening of the density and temperatures profiles is achieved with an additional term in heat conductivities and particle diffusion that vanish outside the radial position of $q = 1$. We also put an edge correction for χ_e, χ_i in the form $\alpha \cdot e^{(1-\rho)^2/\beta}$ with $\alpha = 2$ and $\beta = 0.02$. It is effectively non-zero only at $r/a > 0.8$, and accounts for edge transport not captured by TGLF. Both modifications do not affect the radial region between $r/a = 0.25$ and 0.8, where the turbulence modelling is considered valid.

The TGLF settings are as follows. We work with Miller geometry [54] and kinetic electrons. The total number of modes is 24, in the range $k_y\rho_i = 0.1-25$ (15 of them are in the short wavelength region), which is a default setting proven to represent well the real structure. The heat flux is computed from two most unstable modes per k_y. The velocity shearing effects have been tested and found to be small in these conditions, because the intrinsic $V_{E\times B}$ and $V_{\|}$ rotation velocities (no external torque injection) do not produce relevant velocity shear. This has been shown in both TGLF and GKW simulations. Hence, the shearing has been excluded from the modeling for simplicity. We use the saturation rule 1 [55], though both 0 and 1 have been tested. The major difference between the two only regards the edge region at $r/a > 0.8$, and a proper adjustment of the edge correction for χ_e, χ_i makes the results obtained with both rules very similar.

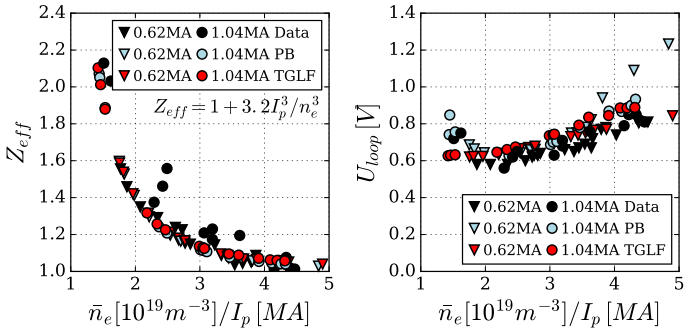

Figure 4.2: *Left: Comparison of measured Z_{eff} (Data) to the scaling (PB and TGLF) for the two plasma current values, as a function of n_e/I_p. Right: corresponding loop voltage values.*

The impurity concentration has been identified as an important quantity for ITG turbulence [56–58]. An increased impurity content leads to main ion dilution, which reduces the ITG drive. The Z_{eff} is given by a scaling depending on engineering parameters of the plasma. It is introduced in Sec. 3.2.1 and has the form

$$Z_{\mathrm{eff}} = 1 + 3.2I_{\mathrm{p}}^3/\bar{n}_{\mathrm{e}}^3 \tag{4.5}$$

with I_p the total plasma current in MA and $\bar{n}_\mathrm{e}$ the line averaged electron density in $10^{19}m^{-3}$. Note, that this scaling has been tested at a minimum $I_\mathrm{p}\bar{n}_\mathrm{e} \approx 1.5$ and is not intended to use at lower densities. Fig. 4.2 shows the scaling Z_eff values of the modeling compared to the Z_eff from the loop voltage measurements data.

Note that here and in the following, the last three points of the $I_\mathrm{p} = 0.62\,\mathrm{MA}$ data subset belong to the second discharge in the subset, #28243, which had slightly different conditions, than the first one, #28386. Presumably, the position of the $q = 1$ surface plays a role here, in the discharge #28243 it is closer to the magnetic axis. These differences are not accounted for, hence not visible, in the ASTRA–TGLF modeling, but are often present in the power balance simulation results.

4.2 Analysis of the results

4.2.1 Comparison to experimental profiles

As already mentioned, the data subsets represent density ramps at two different plasma currents, so that in each subset the plasma evolves from the LOC to the SOC regime. Figures 4.3 and 4.4 show the simulated plasma kinetic profiles in comparison with the measurements for both subsets of discharges. The profiles corresponding to the LOC phase are shown in blue, the SOC – in red, and those at the transition between the phases are drawn black.

The simulated and measured electron density profiles (subfig. *b*) demonstrate a very good agreement, and the simulated electron temperatures (*a*) deviate only slightly from the measured ones. Simulated ion temperature profiles remain the same

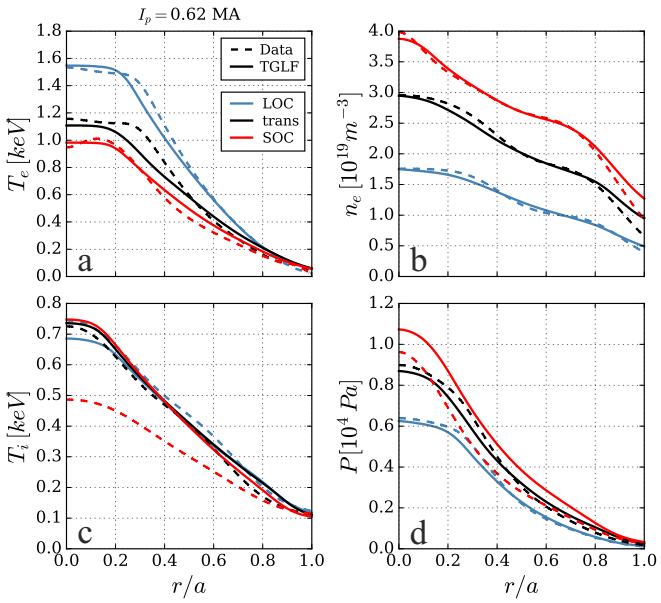

Figure 4.3: *Kinetic plasma profiles simulated with ASTRA–TGLF (solid) and the corresponding experimental measurements (dashed) in the LOC regime, at the transition critical density, and in the SOC regime for* $I_\mathrm{p} = 0.62\,\mathrm{MA}$.

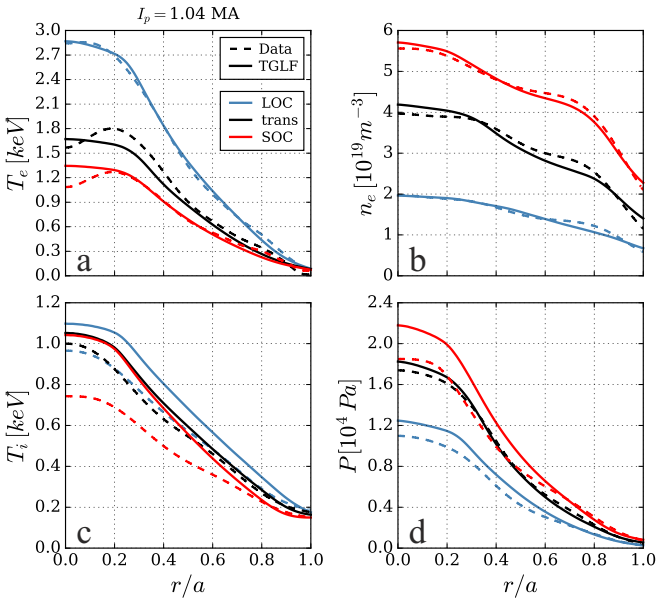

Figure 4.4: *Same as above for* $I_\mathrm{p} = 1.04\,\mathrm{MA}$.

during the density growth, and while TGLF reproduces the measurements well at low densities, a deviation appears at high density, where the observations show a decrease of T_i. This difference is significant, up to 30%. It is also reflected in the simulated pressure profiles, which are higher then the experimental ones in the SOC regime. The effect this deviation may have on the global confinement characteristics is discussed further in this section.

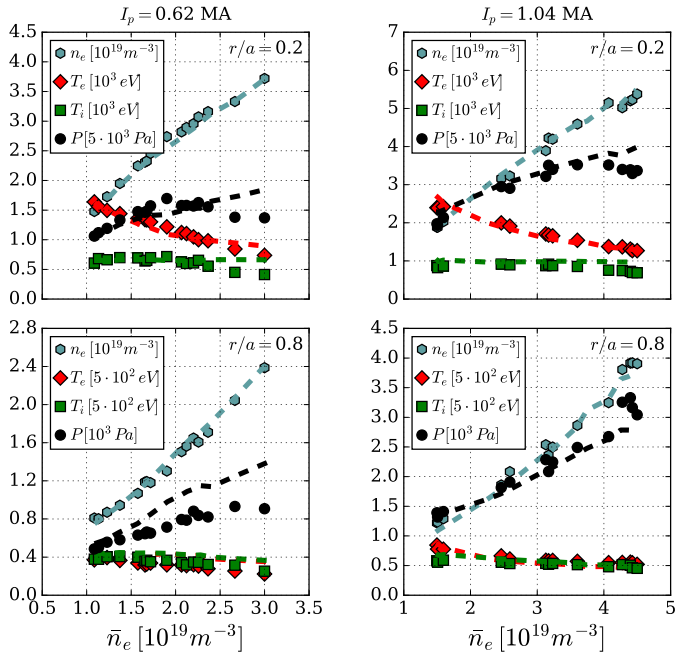

Figure 4.5: *Evolution of plasma kinetic parameters in the core* ($r/a = 0.2$, *top row*) *and at the edge* ($r/a = 0.8$, *bottom row*) *with the density growth, comparison between PB (points) and TGLF (lines) simulations with ASTRA.*

In order to look into the evolution of the kinetic profiles with the increase of the density in more detail, we show a comparison of measured and simulated values in the core, $r/a = 0.2$ and at the edge, $r/a = 0.8$, for both subsets of data, see Fig. 4.5.

The interesting part here is the evolution of the plasma pressure, which provides also the plasma kinetic energy. In the experiment, the edge pressure grows steadily together with the electron density, while in the core it saturates at a certain point. In the plasmas with $I_\mathrm{p} = 0.62\,\mathrm{MA}$ the saturation point is at around $2.0 \times 10^{19} m^{-3}$, for the plasma with $I_\mathrm{p} = 1.04\,\mathrm{MA}$ it is roughly $3.1 \times 10^{19} m^{-3}$. These points can be associated with the LOC–SOC transition critical density. It can be seen that, while the core electron temperature reduces gradually as the density increases, the core ion temperature stays rather constant before the critical density is reached, and starts to decrease after that. Therefore, the plasma energy saturation is likely caused by the ion temperature behavior.

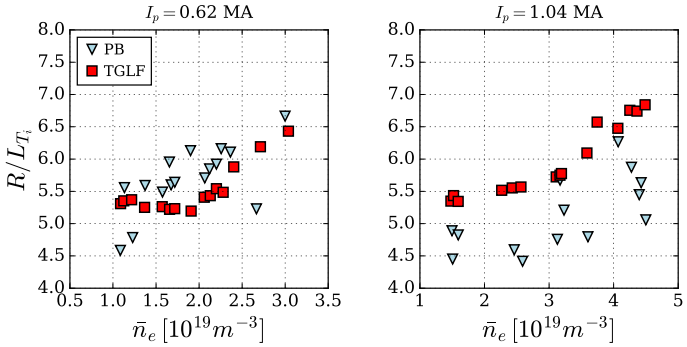

Figure 4.6: *Normalized logarithmic gradient of ion temperature R/L_{T_i}, averaged between $r/a = 0.4$ and 0.6, as a function of mean electron density.*

In the simulation, the pressure saturation at the transition density is less pronounced, because of almost no reduction in the core ion temperature, while the electron temperature and density are reproduced well. However, a modification of ion transport at the critical density can be noticed by the change in the trend of simulated R/L_{T_i}, while the values stay close to the experimental ones, see Fig. 4.6. It should be noted in this regard, that a small difference in local R/L_{T_i} over an extended radial window can produce a significant discrepancy in the core T_i, which is observed at high density.

Fig. 4.7 compares the experimental and the simulated temperature ratio T_i/T_e, averaged around mid-radius, which due to the similarity of T_e and T_i profiles is a good proxy for the global temperature ratio. There is a deviation for the case at $I_\mathrm{p} = 1.04\,\mathrm{MA}$, high density, where the value reaches 0.8 in the simulation, while in the experiment it stays at 0.7.

The effect of T_i/T_e on the frequency of the most unstable mode at this high density at a given radial position $r/a = 0.55$ is shown in Fig. 4.8. Certainly, the difference between 0.7 and 0.8 is rather small. Therefore, we consider the overall effect of the ion temperature mismatch between the modeling and the measurements to have negligible impact on the turbulence properties.

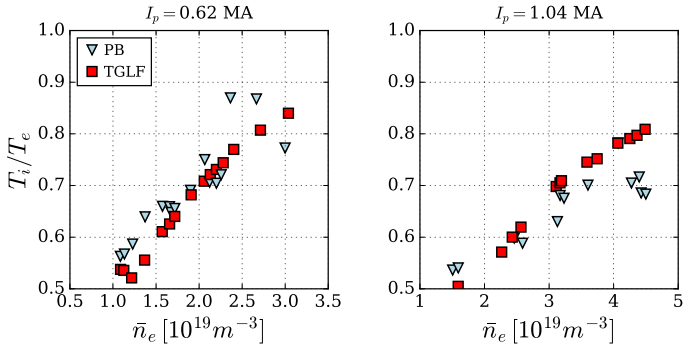

Figure 4.7: *Temperature ratio T_i/T_e, averaged between $r/a = 0.4$ and 0.6, as a function of mean electron density.*

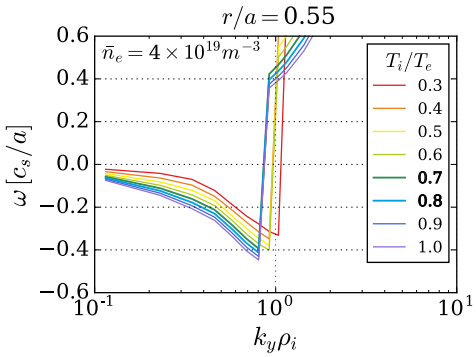

Figure 4.8: *Temperature ratio T_i/T_e effect on turbulence frequency at fixed density.*

4.2.2 Heat conductivities

We continue the analysis by comparing the electron and ion heat conductivities, χ_e and χ_i, from PB and TGLF simulations. In the power balance simulations the heat conductivities are computed from the experimental temperature profiles with Eq. (4.1). In the self-consistent modelling the total heat conductivity is a sum of the turbulent, computed by TGLF, and neoclassical contributions. In all regimes, the neoclassical contribution is approximately one order of magnitude smaller then the turbulent one. Fig. 4.9 illustrates the comparison of heat conductivities, presenting the values averaged over the radial range from $r/a = 0.4$ to 0.6.

The TGLF electron heat conductivity shows inverse proportionality to the average electron density, reducing from slightly above $1\,m^2/s$ at $1 \times 10^{19}m^{-3}$ to $0.4\,m^2/s$ at high density for both plasma currents. The power balance values show a similar trend at low and middle density values, while at high density they significantly diverge. The ion heat conductivity from TGLF demonstrates a slight decrease with the electron density increase as well, except for the very low densities, where it appears to grow. On the contrary, the power balance χ_i shows a steady increase, roughly quadratic with the average density, reaching up to $4\,m^2/s$ at the top of the density scans in both cases. It is expected from studies like [60] that χ_e is reduced when the collisionality increases, as TEM is stabilized by collisions, and the electron heat transport is driven by the ITG mode. The trend of χ_e values computed by TGLF is consistent with this picture.

The values of power balance χ_e and χ_i depend on the assumptions made for the

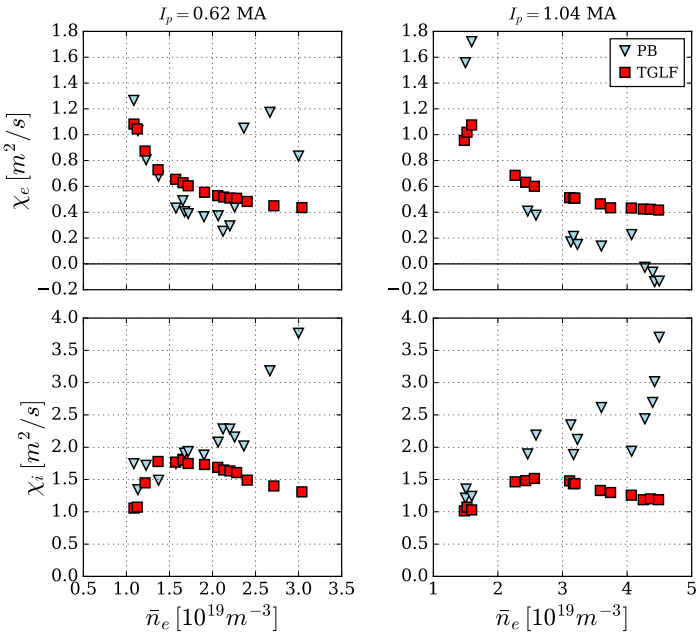

Figure 4.9: *Heat conductivities from PB and TGLF simulations, averaged between* $r/a = 0.4$ *and* 0.6 *as functions of mean electron density. Error bars on the PB points are estimated to be between* 20% *and* 50%

radiated power model and the magnetic equilibrium. In extreme cases, a variation up to 30% is observed in both directions, and the χ_e trend may vary. However, the rapid rise of χ_i at high density remains irrespective on the assumptions made on P_{rad}. From the observed overestimation of T_i by TGLF at high density one can expect that χ_i is underestimated. On the other hand, χ_e of TGLF is reasonable, but the power balance χ_i is too high to be consistent with it. Considering high sensitivity of the PB-calculated heat conductivities to the profile shapes, we believe that the actual values of χ_i are only slightly higher then the TGLF prediction.

4.2.3 Energy confinement time

The global energy confinement time for all considered discharges is displayed in Fig. 4.10, where the experimental estimate is compared to the values from PB and TGLF simulations. Despite the similarity of the kinetic plasma profiles in the experimental database and the PB modeling, the energy confinement time values do not always coincide. The reason is, first of all, in the different approaches to compute τ_E. The experimental estimate takes the total kinetic plasma energy as the stored energy, while in ASTRA it is the kinetic energy of electrons and deuterium and boron ions only (though the difference should be rather small). Also, although the Ohmic power is defined as $P_{\mathrm{Ohm}} = I_p U_{\mathrm{loop}}$ in both approaches, the loop voltage values slightly differ, as discussed in section 4.1.

Looking at the TGLF simulations results, one can see that the range of values of τ_E is recovered by the model. This implies that, as the kinetic profiles are satisfactorily

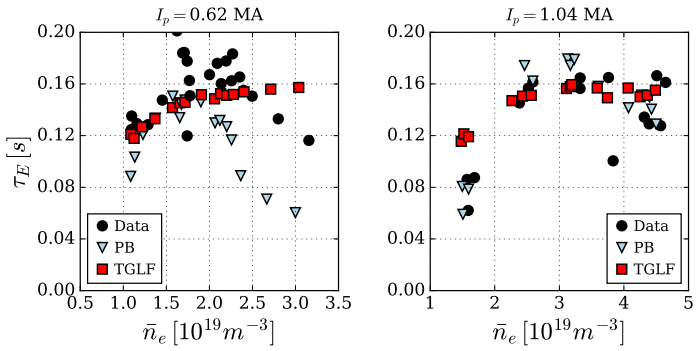

Figure 4.10: *Energy confinement time as a function of average electron density.*

reproduced (see figures 4.3, 4.4), also the net power $P_{\mathrm{Ohm}} - P_{\mathrm{rad}}$ is obtained within reasonable limits, despite uncertainties in the effective charge, loop voltage, and radiated power. Since the former two could be reasonably constrained by measurements, the radiated power approximation seems to be good, as well.

Second, the trend of τ_{E} with respect to the electron line averaged density shows both the linear and the saturated phase. Note that the saturated phase begins at lower densities ($\approx 2 \times 10^{19}$) for the lower current case, while the 1 MA case displays the transition at $\approx 3.1 \times 10^{19}$, and here the simulations and the measurements agree.

While in the higher current case the experimental confinement time in the SOC phase experiences minor to no degradation, in the lower current case it is significantly reduced after the phase transition. The simulations results do not have this feature, they show confinement time saturation at a constant level. This disagreement may arise due to the fact that χ_i^{TGLF} depends on the density much weaker than χ_i^{PB}. Ultimately, this most likely points towards a problem of too weak stiffness of the ITG transport in TGLF, which leads to an overestimation of R/L_{T_I} discussed in Sec. 4.2.1.

4.2.4 Global energy and power balance

Since the confinement time is the ratio between plasma energy and absorbed power, it is useful to look at these ingredients separately and compare the modeling results to the experimental data. In Fig. 4.11, the ASTRA-TGLF simulated Ohmic power P_{Ohm}, total radiated power $P_{\mathrm{rad\,tot}}$, total absorbed power $Q_{\mathrm{tot}} = P_{heat} - P_{rad}$ and total plasma energy W_{tot} as functions of the ratio $\bar{n}_{\mathrm{e}}/I_{\mathrm{p}}$ are compared to the results with PB.

Considering the accuracy of the agreement on the loop voltage (Fig. 4.2), the Ohmic power is reproduced with the same quality, and so is Q_{tot}, which is an important element to compute the power balance. Both are shown to moderately increase with the density. The plasma energy grows roughly linearly with the density, with simulated values higher than experimental at high densities, which is a consequence of underestimated ion transport, as shown in Fig. 4.9.

The discrepancies in the experimental and simulated W_{tot} and Q_{tot} can explain the behavior of the confinement time shown in Fig. 4.10, in particular the big deviation seen in the SOC phase for the lower current case.

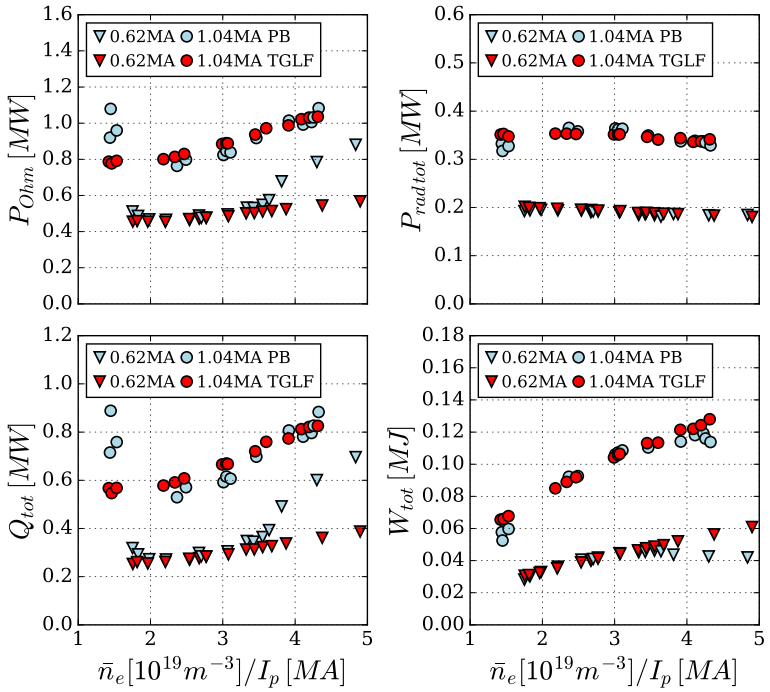

Figure 4.11: *The Ohmic power P_{Ohm}, total radiated power $P_{\mathrm{rad\,tot}}$, total absorbed power Q_{tot} and total plasma energy W_{tot} as functions of the ratio $\bar{n}_{\mathrm{e}}/I_{\mathrm{p}}$.*

4.2.5 Density peaking behavior during the density scan

L-mode Ohmic plasmas also demonstrate a change in density profile peaking behavior at different average electron densities. The profile is rather flat at very low density, it becomes peaked shortly before the critical density of the LOC-SOC transition, and reverts back towards a flatter profile as the density is further increased. The maximum peaking is found theoretically to happen at the TEM-ITG transition, while both in deep TEM or deep ITG regimes, the density profile flattens (due to outward-directed thermodiffusion in TEM and outward directed collisional pinch in ITG) [7, 12, 61]. Fig. 4.12 shows the evolution of density peaking during density ramp-ups in our plasma conditions, as defined by the ratio of the centrally averaged electron density (inside $r/a = 0.2$) to the full volume average value, and by a R/L_n averaged around the mid-radius, between $r/a = 0.3$ and $r/a = 0.7$.

Note that the highest peaking appears at the average densities below critical density of the LOC-SOC transition. This is consistent with the result that the dominant turbulence regime is already the ITG when the LOC-SOC transition takes place, whereas dominant TEM conditions can occur at densities which are below those corresponding to the maximum density peaking. However, the situation can be different in other machines, as reported in [62], which also shows that the previously thought picture TEM $\rightarrow$ ITG $\Rightarrow$ LOC $\rightarrow$ SOC does not hold as a universal mechanism.

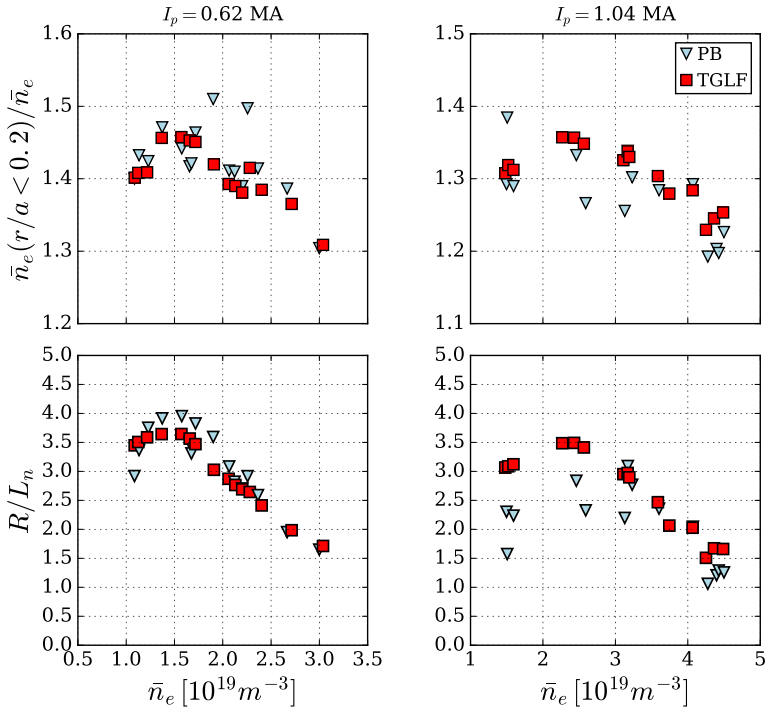

Figure 4.12: *Measures of density peaking: the ratio $n_e(core)/\bar{n}_e$ (top) and the normalized logarithmic electron density gradient averaged between $r/a = 0.3$ and $r/a = 0.7$ (bottom) as functions of average electron density, for the two plasma currents.*

4.2.6 Turbulence spectra

In order to gain a deeper understanding on how the energy transport varies during the density buildup, it is instructive to look at the spectral characteristics of the turbulence as predicted by TGLF.

For this analysis, the TGLF code is run separately, outside of ASTRA environment with data files generated by the ASTRA-TGLF modeling for specific radial points. It produces k-spectra of the real frequency of the most unstable mode $\omega(k)$ normalized to c_s/a, and the electron and ion heat fluxes $Q_{e,i}(k)$ expressed in arbitrary real units. Note that TGLF could be run directly with experimental data, though the ASTRA-TGLF self-consistent profiles are preferable due to their consistency with the heat fluxes, moreover all plasma parameters are smooth and the values are still very close to experimental. One could argue that the simulated ion temperature much exceeds the measurements, but its normalized gradient R/L_{T_i} that plays a role of turbulence drive is very close to experimental (see Fig. 4.6), except the region of high density at high current, so this does not affect the discussion on the LOC-SOC transition. In this situation, the only turbulence-relevant parameter predicted outside the experimental error bars is the temperature ratio T_i/T_e, but its impact on the turbulence is shown in Sec. 4.2.1 to not be relevant in determining the turbulence properties in the range of deviation from the measurements. The effect this and other quantities have on transport is discussed in detail in section 4.2.7.

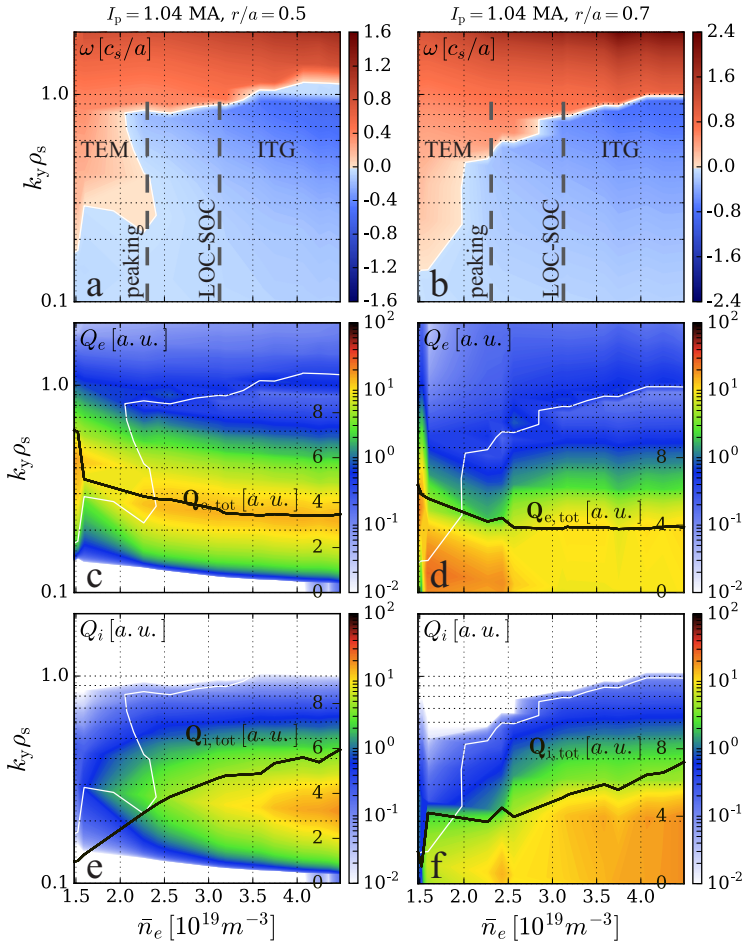

Figure 4.13: *Turbulence spectral characteristic, density scan representation*

Fig. 4.13 illustrates the turbulence spectral analysis for the data subset with $I_p = 1.04\,\mathrm{MA}$, presenting ω, Q_e and Q_i in the range $k_y\rho_s = [0.1 - 2]$. Electron heat transport due to high-k ETG turbulence has been found small according to TGLF in these plasma conditions, it does not exceed 1% of the total electron transport. Therefore, we limit the k-space shown in the plots to $k_y\rho_s < 2$. We choose the radial points $r/a = 0.5$ and $r/a = 0.7$, so that we are able to show also the radial variation of the parameters presented. The picture for the lower current case is very similar, scaled to the averaged density by the plasma current ratio. For the mode frequency ω, the sign convention is that a positive value refers to a mode rotating in the electron diamagnetic direction (e.g., TEM when the frequency is robustly positive).

It can be seen from the top plots (a, b), that the transition between TEM and ITG indeed happens along the density scan (line averaged density as a control parameter in the horizontal axis). However, the scales below $k_y\rho_s = 0.2$ seem to be dominated by ITG already at the lowest densities in the range of study, and other wavenumbers up to $k_y\rho_s = 1.0$ experience the mode transition at different values of $\bar{n}_e$. As a rule, lower k_y values transit first, since the collisional frequency is wavenumber independent, so at a fixed collisionality, electron detrapping at larger scales is more efficient [63].

Interestingly, the mode transition at scales responsible for the dominant heat transport (namely, $k_y\rho_s = [0.3 - 0.7]$) occurs close to the average density of the highest density peaking, especially at the mid-radius. At the same time, no significant variation of the ω spectrum is observed at the LOC to SOC regime transition.

The electron heat flux $Q_e(k)$ in the subplots c and d is expressed in arbitrary units ($[gB]\cdot n_e T_e^{5/2}$, which to a constant factor are watts), in logarithmic scale, in order to resolve also minor contributions of subdominant modes. The white line marks the boundary between positive and negative mode frequencies. It can be seen, especially at scales around $k_y\rho_s = 0.8$, that the electron heat flux drops by about an order of magnitude as the given scale shifts to the ITG-dominant regime. The explanation can be given as follows: TEM propagates in the electron diamagnetic drift direction, and the transport by electrons, which drift in the same direction is enhanced, it is said to be resonant; ITG propagates in the opposite direction, so the transport is reduced due to this non-resonance condition. Nevertheless, the electron heat transport channel in the ITG domain is still substantial, and the total heat flux (shown with the black line) stays relatively constant. Interesting to note, the wavenumber of the mode with highest transport activity shifts towards larger scales as the average density increases, as well as when comparing outer regions of the plasma to mid-radius position.

The ion heat flux (subplots e and f) is driven by the ITG alone, and no transport is observed outside the typical scales of ion turbulence. The subplot e shows that ITG activity starts already at the lowest density in the range of study, but the ITG mode is still subdominant there. The total heat flux in the ion channel increases steadily with the average density, much due to the increasing strength of ITG with decreasing Z_{eff}.

Fig. 4.14 illustrates the same quantities from a different perspective, presenting radial profiles of ω, Q_e and Q_i for three selected mean density values: 1.48, 2.27 and $3.17 \times 10^{19}\,\text{m}^{-3}$, with the latter two being close to the maximum peaking density and the critical LOC-SOC density, respectively. The real frequency ω is expressed in c_s/a, the heat fluxes are expressed in arbitrary units ($[gB]\cdot n_e T_e^{5/2}$). The densities are chosen such that the turbulence regime changes: from dominant TEM, through the condition of mode transition to dominant ITG. It can be seen how the scale of maximum electron heat flux goes to smaller k_y as the density increases, moving from TEM to ITG-driven. The ion heat flux is almost negligible at low density, but increases as the ITG becomes stronger. The picture at even higher density is very similar to the third one, just with larger Q_i, as can be guessed from Fig. 4.13. Note, that Q_i is reduced at $r/a \gg 0.7$ at intermediate and high densities, this is an effect of backward energy transfer from the ions to the electrons, since $T_i > T_e$ there.

This analysis confirms the relation of the TEM-ITG dominant turbulent mode transition to the density peaking phenomenon. At the same time, we find no proof that this mode transition impacts the global confinement and, more specifically, leads to the energy confinement time saturation. Rather, it seems that when the ITG-driven ion heat flux reaches a certain value, the confinement does not improve anymore. Similar conclusions have been made in [13, 26], however other works (for example, [64, 65])

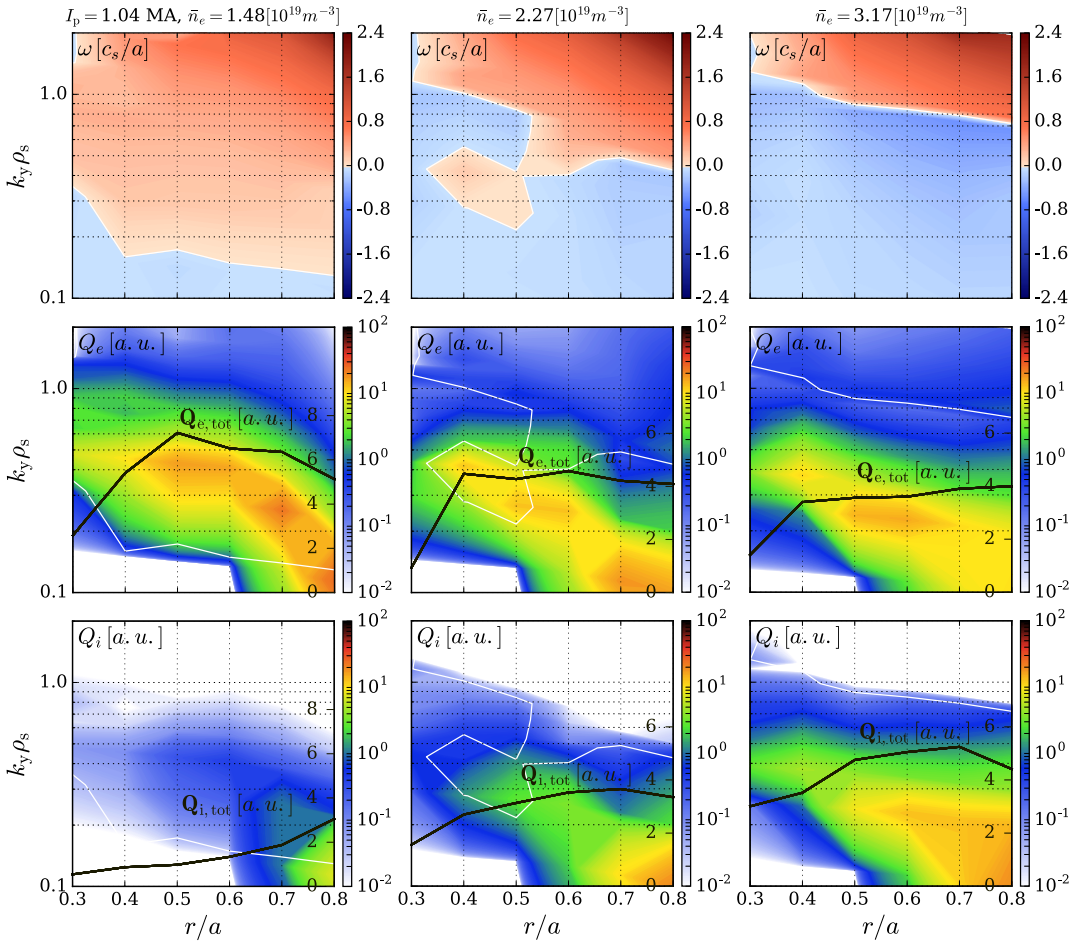

Figure 4.14: *Turbulence spectral characteristics, radial representation*

report TEM-ITG transition and the τ_E saturation at the same density value, and others [66] even in the opposite order.

4.2.7 Sensitivity analysis of heat fluxes

In order to complement the study of heat transport in the electron and ion transport channels, we perform a sensitivity analysis of these quantities to various plasma parameters. The aim here is to clarify whether the LOC-SOC behavior in terms of ITG and TEM-ITG transition is governed by a single dominant parameter, or by a combination of many. Since the average electron density and the plasma current (that influences also the magnetic equilibrium) seem to be the main actuators, we fix one of them by the choice of data points, and investigate their impacts separately.

First, we define a data point (I) in the subset with $I_p = 0.62$ MA in the beginning of the SOC phase, so that in the subset with $I_p = 1.04$ MA there exist a data point (II) with the same average density, but in LOC phase. We then find a third point (III) in the lower current subset, so that its confinement time equals that of point II (see Fig. 4.15). During the self–consistent ASTRA–TGLF simulations for each of these

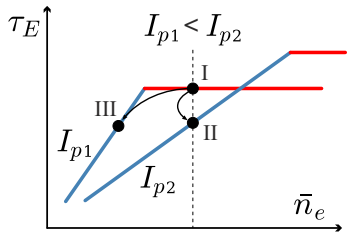

Figure 4.15: *Substitution scheme*

three data points a TGLF input file is produced, that corresponds to a specific radial location (here $r/a = 0.5$). These input files contain all the physics parameters needed to run the code, like safety factor, magnetic shear, normalized temperature and density gradients, species density concentrations etc. We than take the data file for the point II and replace one of the parameters with that from the point I, keeping all the others unchanged. As a result, we simulate plasma conditions of the LOC regime, with one of the parameters from the SOC. Running the TGLF code with this modified input file and comparing the outcome in terms of heat fluxes, one can see which parameters are mostly responsible for the transition between the LOC and SOC plasma turbulence regimes. The same is done with the LOC data of the point III. This way we arrive to two sets of modified plasma conditions and the heat fluxes obtained accordingly.

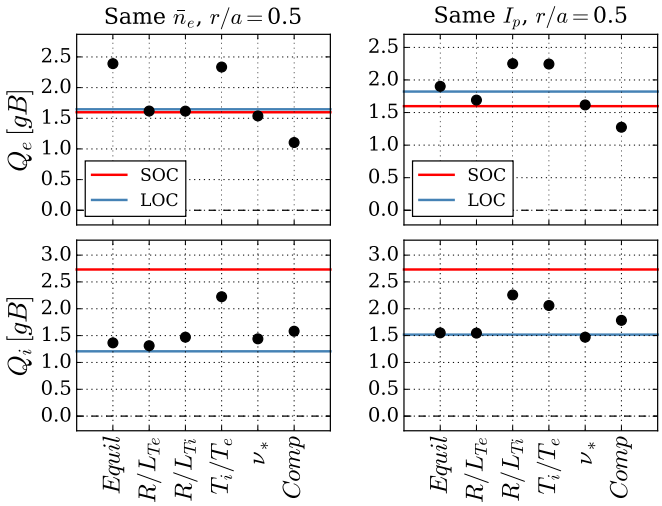

Figure 4.16: *Sensitivity of electron and ion conductivities to single parameter variation.*

Fig. 4.16 presents the result of this exercise, showing relative variations of the electron and ion heat fluxes in gyro–Bohm units. The lines mark the heat fluxes of nominal plasma conditions: red corresponds to the SOC regime of I, blue on the left ("Same $\bar{n}_e$") is the LOC of II, blue on the right ("Same I_p") represents the LOC of the data point III. Note that the electron heat flux (in gB units) is almost at the same level in all three conditions. The replaced parameters are: magnetic equilibrium and plasma geometry (*Equil*), normalized logarithmic gradients of electron and ion temperatures, the temperature ratio, collisionality, and the plasma composition (*Comp*), that includes species densities and density gradients. The black dots show the heat fluxes levels in

the conditions when this parameter is replaced. A dot that lies on the blue line means that this replacement has no effect. An important remark: if one replaces all of these parameters at once, both the electron and the ion heat fluxes appear at the red lines.

The following conclusions can be drawn:

1. Having different currents or different densities does not have a direct impact on the transport levels, as the plots look very similar, except for the effect of changed equilibrium on the electron heat flux when the averaged density is fixed, which is however expected.

2. Reducing the electron-ion temperature difference raises Q_e due to TEM destabilization, whereas increasing the collisionality has the opposite effect. R/L_{T_i} affects ITG-driven electron heat transport. The *Comp* factor impacts Q_e via the electron density gradient, that is smaller in SOC.

3. Q_i is influenced the most by R/L_{T_i} and $T_\mathrm{i}/T_\mathrm{e}$ factors that have effect on ITG stability, and by the impurity concentration (Z_eff) embedded in the *Comp* factor. High impurity content means dilution of main ion species that reduces the ITG drive at lower average electron densities.

We can conclude here that the temperature ratio is an important factor leading to a destabilization of both major turbulent modes and the increase of the corresponding heat fluxes. The normalized gradient of ion temperature R/L_{T_i}, as well as the effective charge Z_eff have a particular impact on ITG turbulence, the variation of these parameters over the density scans leads to an increase in ion heat flux and the LOC-SOC regime transition. At the same time, the electron heat flux has no preferential change. The role of Z_eff in determining a correct behavior of the ITG along the LOC-SOC transition has been previously investigated [56–58], and the following section presents an additional study of it in the context of this work.

4.3 Effect of impurity content on turbulence and confinement

In order to show the effect of the impurity concentration on turbulence more explicitly, and inspired by numerous experiments on achieving so-called Improved Ohmic Confinement (IOC) phase in Ohmic plasmas (for example, as described in [67,68]), we have also conducted ASTRA-TGLF simulations with various levels of impurity content which will affect the value of Z_eff. We use the same modeling approach as discussed in section 4.1. With fixed Z_eff dependence on $\bar{n}_e$ and flat Z_eff radial profile, we investigate the range from $Z_\mathrm{eff} = 1$, i.e. pure deuterium plasma, to $Z_\mathrm{eff} = 4$ in the Ohmic plasmas with $I_\mathrm{p} = 1.04\,\mathrm{MA}$. The results can therefore be directly compared to those presented above for the same plasma current. Note that while values with $Z_\mathrm{eff} \geq 3$ are hardly

realistic with boron impurities alone, they may be seen as an extension of the realistic range, which shows that the trend of energy confinement improvement has its limits.

Fig. 4.17 compares the energy confinement time τ_{E} and the mid-radius R/L_n as functions of the average electron density for the plasma with the experimental Z_{eff} scaling discussed in pervious sections (shown with black squares), to those of plasmas with fixed Z_{eff} values (colored circles). It can be seen from the τ_{E} plot that, with increasing boron content, the linear phase extends itself to higher densities, and the τ_{E} saturation becomes less pronounced. Plasmas with high Z_{eff} feature higher resistivity, which leads to higher Ohmic power and, consequently, higher electron and ion temperatures. The best confinement at high density is reached with $Z_{\mathrm{eff}} \approx 3$, when no saturated phase can be distinguished anymore. At even higher Z_{eff} the reduced ion density limits the stored energy W_{tot}, and despite the ITG turbulence suppression the confinement quality decreases. The shift of the R/L_n peak to higher density with the Z_{eff} increase serves as an indicator for the corresponding shift in the dominant turbulent mode transition, as discussed in section 4.2.5.

Fig. 4.18 presents ω, Q_{e} and Q_{i} at the radial position $r/a = 0.7$ in the range $k_{\mathrm{y}}\rho_{\mathrm{s}} = [0.1 - 2]$, obtained with pure deuterium plasma, $Z_{\mathrm{eff}} = 1.0$ (on the left), and with significant impurity content, $Z_{\mathrm{eff}} = 3$ (on the right) that corresponds to the best τ_{E} as shown in Fig. 4.17. Figure 4.18 can be compared with Fig. 4.13 (b,d,f), which represents the same spectral characteristics at the same radial location for plasmas with experimental Z_{eff} scaling and can be considered as a reference. In pure deuterium plasma the ITG takes over already at a very low density, otherwise the plasma behavior is similar to the case of experimental Z_{eff} scaling. With $Z_{\mathrm{eff}} = 3$ the ion dilution effect stabilizes the ITG. The increased T_e reduces the equipartition power, so at high density the temperature ratio T_e/T_i stays higher and provides an additional ITG stabilization. The increased R/L_{T_e} enhances the electron heat flux, so TEM dominates the energy transport up to significantly higher densities. Despite the Ohmic power is higher, larger Q_e at low density slightly decreases the confinement time. At the same time, ITG is strongly suppressed, so Q_i grows slowly with the density, and the linear trend holds in

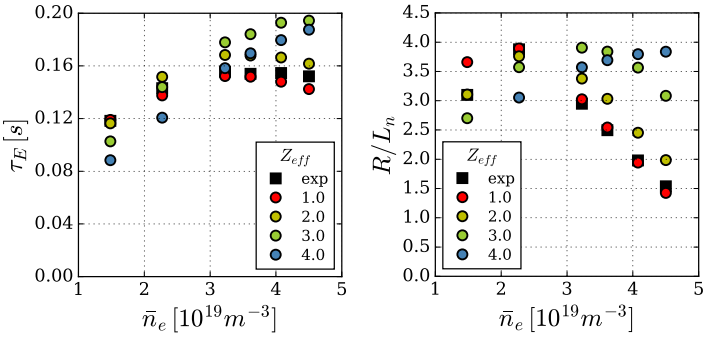

Figure 4.17: *Energy confinement time τ_{E} and the normalized logarithmic electron density gradient R/L_n averaged within the radial range $r/a = 0.4 - 0.6$ as functions of average electron density, for different Z_{eff} values.*

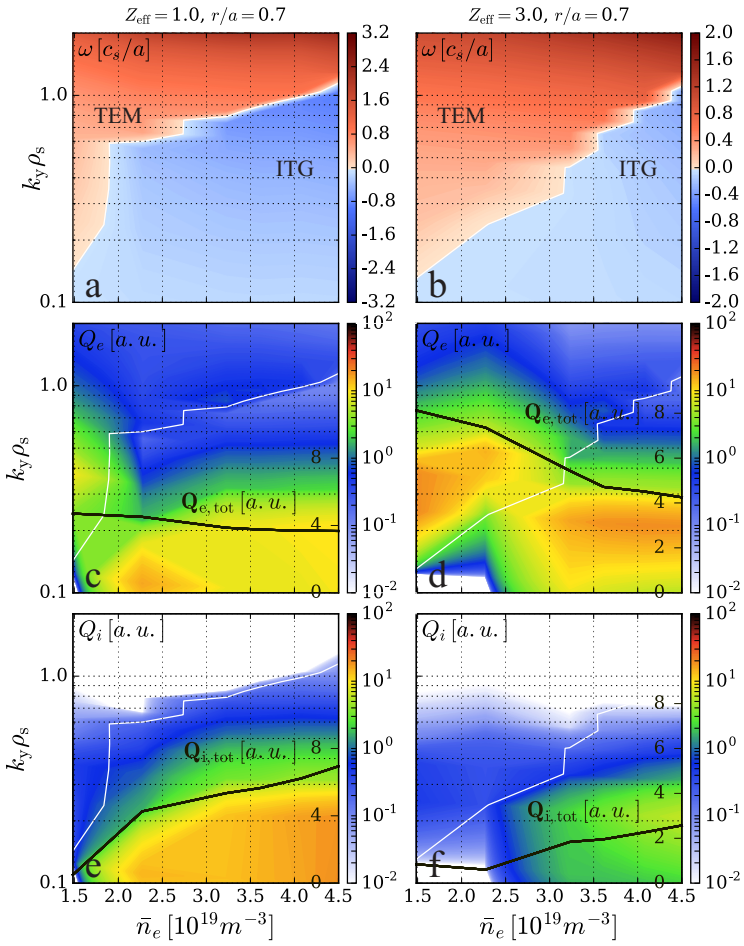

Figure 4.18: *Turbulence spectra with* $Z_{\rm eff} = 1$ *(a,c,e) and* $Z_{\rm eff} = 3$ *(b,d,f).*

a wider range of densities.

With high impurity concentration, the dominant turbulent mode transition and the confinement regime modification are still well separated in the parameter space. For example, in the plasma with $Z_{\rm eff} = 3$ at $\bar{n}_e = 3.5 \times 10^{19}$ the heat transport in both electron and ion channels is already dominated by ITG, but the ion heat flux is still small, and the plasma is still in the linear confinement regime. It can be concluded that what defines the saturation of $\tau_{\rm E}$ is the ion heat flux, which in the case of high-$Z_{\rm eff}$ IOC regime is reduced by main ion dilution.

4.4 Conclusions on energy confinement modelling

In this work it has been shown that TGLF, embedded in the ASTRA transport solver, is able to reproduce the energy confinement time saturation in L-mode plasmas as observed in AUG. The confinement scaling transition from linear to saturated has been studied in detail, at two values of the plasma current. In both cases, the plasma core at low density is dominated by TEM turbulence, while ITG mode is instead stable.

Ion channel of turbulent heat transport is weak. With the increase of density, TEM is suppressed by higher collisionality, ITG enhances and starts to dominate both electron and ion heat transport channels. Switching of different k_y-scales between TEM and ITG dominance occurs gradually both along the radial coordinate and the density scan, with the mid-radial region switching the last (see Fig. 4.14 for details). At this point, the maximum in electron density peaking is observed. The saturation of energy confinement time happens at higher density, which does not support the paradigm of direct influence of the turbulence regime on the confinement scaling. The critical densities of TEM-ITG and, later, LOC-SOC transitions are roughly proportional to the plasma current value. On the other hand, one can think of a situation when the TEM mode is strong for some reason, and a critical Q_i is reached before the TEM-ITG transition.

The LOC phase can be explained by a reduction of electron transport as the coupling between ion and electron temperatures becomes stronger. The absolute heat loss rate stays constant, while the energy content increases. This holds even after the ITG becomes dominant.

The transition to the SOC phase is a consequence of a number of factors. The T_e-T_i coupling becomes strong and the T_e reduces, as more heat is transferred to the ions. The increase of R/L_{T_i} and the reduction of the impurity concentration leads to the ITG mode enhancement, ion heat transport is strongly stiff and effectively exhausts the thermal energy.

The impurity content is confirmed to be an essential ingredient here, it acts through dilution to stabilize the ITG at lower densities, when impurities are more abundant. The observed scaling of the confinement time transition density as a function of plasma current thus reflects the dependence of Z_{eff} on plasma density and current itself. Additional impurity seeding thus can shift the plasma to the IOC phase, by reducing turbulent heat flux via ITG stabilization, which is clearly demonstrated by the simulations.

Chapter 5

Intrinsic toroidal rotation modeling

A lot of attention has recently been drawn to the observation, obtained from many machines, of the sustainment of a sizeable plasma toroidal rotation in the absence of any external source of momentum. This intrinsic plasma rotation has been found [10–16] to develop a significant velocity gradient around mid-radius with the increase of density (and collisionality), with a pronounced counter-current velocity in the core. However, at even higher collisionality the velocity profile relaxes back to co-current and roughly flat (see Sec. 3.2.2). It can be shown that such behavior can only arise from a component of the stress tensor not related to either viscosity or convection (referred to as the residual stress). From a theoretical point of view, this finite residual stress can appear only when parallel symmetry is broken. In an axisymmetric torus this translates to the breaking of the poloidal symmetry in the fluctuations or in the equilibrium. Several symmetry breaking mechanisms have been proposed recently [17–24]. In some of these, the stress on a given flux surface depends on the local parameters, while the background is considered constant; others are global, meaning they require a radial variation of plasma profiles, which immediately breaks the radial symmetry and, consequently, the poloidal symmetry, as the two are linked via the drifts. Several local mechanisms have been tested with AUG parameters and found to be weak [69], hence a global mechanism is believed to dominate. At the same time, it has been demonstrated in [70] that the most prominent global effect is the radial shearing of background equilibrium profiles [20]. It introduces the radial shear in the magnetic drift frequency, which is related to the mode frequency, and the poloidal tilting of turbulent eddies. The resulting asymmetry in the k_r spectrum gives rise to a non-zero poloidally averaged parallel wave number $\hat{k}_{\|}$ that leads to a finite residual stress. This section shows the results of the work aimed to estimate the tilt angle $\hat{\theta}_0$ values that suffice to explain the observed toroidal rotation profiles.

5.1 Residual stress scaling

The toroidal momentum transport model used in this work has been described in [71], where a solution is obtained for the mean parallel velocity $u_\parallel$ taking into account contributions from diamagnetic and poloidal flows in addition to the usual $E \times B$ contribution. We make use of the radial coordinate $\rho = \sqrt{\Phi/\pi B_0}$ with Φ the toroidal flux enclosed by a given flux surface and B_0 the reference magnetic field. The radial flux of toroidal angular momentum then has the following form:

$$\left\langle R\frac{B_\varphi}{B}\Pi_{\parallel\rho}|\nabla\rho|\right\rangle = \frac{R_0^2 B_0}{I}\langle|\nabla\rho|^2\rangle\left[-\rho_m\chi_\parallel\frac{\partial u_\parallel}{\partial\rho} + \rho_m V u_\parallel + \delta_{neo}\right] + \\ + \left\langle R\Pi^{res}_{\varphi\rho}|\nabla\rho|\right\rangle, \tag{5.1}$$

where $\Pi_{\parallel\rho}$ is the parallel stress tensor, δ_{neo} contains diamagnetic and poloidal flow contributions and $\Pi^{res}_{\varphi\rho}$ is the residual part of the stress tensor, angular brackets denote flux surface averaging. In the following we will refer to the last term as the residual flux and denote it with Γ_R. Note that the effect of δ_{neo} has been already studied and found too small to explain the observed rotation gradient in the given conditions [69].

The nature and structure of the residual stress can be derived from the linearized gyrokinetic equation for the fluctuating part of the distribution function $\tilde{f}$ that reads

$$\partial_t\tilde{f} + v_\parallel\nabla_\parallel\tilde{f} + \mathbf{v}_{E,0}\cdot\nabla\tilde{f} + \mathbf{v}_d\cdot\nabla\tilde{f} + \dot{v}\nabla_v\tilde{f} = -\tilde{\mathbf{v}}_E\cdot\nabla F_M - \tilde{\dot{v}}_\parallel\nabla_v F_M \tag{5.2}$$

Assume that $\tilde{f}\left(\rho,\theta,\varphi,v_\parallel,\mu\right)$ is symmetric under $(\theta, v_\parallel) \to (-\theta, -v_\parallel)$ transformation. This means that modes with positive and negative $k_\parallel$ have equal amplitudes, and the flux surface average $\langle k_\parallel\rangle = 0$. As shown below, such symmetry brings the residual stress to zero. Hence, in a real plasma that displays finite intrinsic rotation the parallel symmetry must be broken. The degree of asymmetry can be characterized by the Bloch shift parameter θ_0 defined as $\theta_0 = -k_r/(\hat{s}k_\theta)$ (more technical details in [20, 73]). It can be seen as an angle by which the turbulent eddies are turned (on the average over the flux surface) from the radial direction. It also shows the resulting shift of the maximum of the potential fluctuations in the poloidal direction (see Fig. 5.1). The mean $\langle k_\parallel\rangle$ also depends on θ_0, but the analytic form of this dependence is unknown.

Taking velocity moments of the equation (5.2) (a more detailed derivation can be found, for example, in [34]), we arrive to a set of fluid equations:

$$\omega\tilde{n} + 2\tilde{n} + 2\tilde{T} + 4(u+\hat{k}_\parallel)\tilde{w} = \left[\frac{R}{L_n} - 2\right]\phi, \tag{5.3}$$

$$\omega\tilde{w} + 4\tilde{w} + 2(u+\hat{k}_\parallel)\tilde{n} + 2(u+\hat{k}_\parallel)\tilde{T} = \left[u' - 2(u+\hat{k}_\parallel)\right]\phi, \tag{5.4}$$

$$\omega\tilde{T} + \frac{4}{3}\tilde{n} + \frac{14}{3}\tilde{T} + \frac{8}{3}(u+\hat{k}_\parallel)\tilde{w} = \left[\frac{R}{L_T} - \frac{4}{3}\right]\phi, \tag{5.5}$$

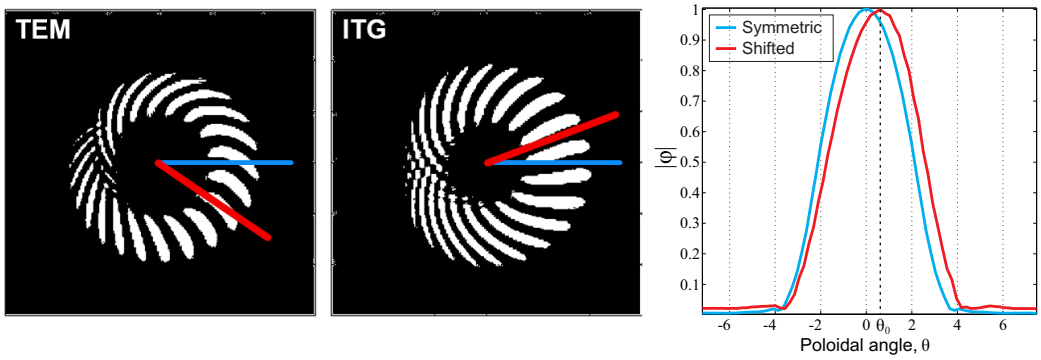

Figure 5.1: *Tilting angle illustration in terms of turbulent eddies in the poloidal cross-section for two turbulent modes (TEM and ITG simulations from [20]) and the distribution of potential fluctuations over the extended poloidal angle (from GKW [69])*

where we exploit the following notation and normalizations:

$$u' = \frac{R^2}{v_{th}}\frac{d\Omega}{dr}, \quad u = \frac{R\Omega}{v_{th}}, \quad \hat{k}_\parallel = -\frac{k_\parallel v_{th}}{4\omega_D} \text{ with } \omega_D = -\frac{k_\theta T}{eBR}. \tag{5.6}$$

The combination of equations (5.3) and (5.4) yields

$$\tilde{w}\left[\omega + 4\left(1-\hat{u}^2\right)\right] = \left[u' - \hat{u}\left(\frac{R}{L_n} - \frac{\omega}{\tau}\right)\right], \tag{5.7}$$

where $\hat{u} = u + \hat{k}_\parallel$ and we used the quasineutrality condition $\phi = Z\tau\tilde{n}$ assuming $Z = 1$, $\tau = T_e/T$, which suggests main plasma ions as the principle medium of turbulent momentum transport.

Expression for the toroidal stress $\Pi_{\varphi\rho} \propto \mathrm{Im}(\phi^\dagger \tilde{w})$ can be then derived as

$$\Pi_{\varphi\rho} \propto u' - 4\hat{u}\left(1-\hat{u}^2\right) - \hat{u}\frac{R}{L_n}, \tag{5.8}$$

and the residual part is then expressed in the following form:

$$\frac{\Pi^{res}_{\varphi\rho}}{\hat{\chi}_\varphi} = \hat{k}_\parallel\left[\frac{R}{L_n} - \frac{4}{\tau}\left(\hat{k}_\parallel^2 - 1\right)\right] \tag{5.9}$$

One way to proceed is to introduce a representation of the parallel wave vector and its square as $k_\parallel = \hat{s}\theta_0/(qR)$ and $k_\parallel^2 = 1/(qR)^2$, with q the safety factor and $\hat{s}$ the magnetic shear. The normalized quantities become

$$\hat{k}_\parallel = \frac{k_\parallel v_{th}}{4\omega_D} = \frac{k_\parallel R}{2k_\theta\rho_i} = \frac{\hat{s}\theta_0}{2qk_\theta\rho_i}, \quad \hat{k}_\parallel^2 = \frac{1}{4q^2(k_\theta\rho_i)^2}.$$

The resulting expression for the residual stress after recovering all normalizations and making an ITG-relevant assumption $k_\theta\rho_i = 0.5$ can then be written as

$$\Pi^{res}_{\varphi\rho} = \rho_m\chi_\varphi\frac{v_{th}}{R^2}\frac{\hat{s}\theta_0}{q}\left[\frac{R}{L_n} - \frac{4}{\tau}\left(\frac{1}{q^2} - 1\right)\right]. \tag{5.10}$$

This formula is similar to formula (26) obtained in the work [20]. Despite this approach being fully analytic, it implies a strong assumption, that is $k_{\|} \propto \theta_0$, which needs verification.

In practice, TGLF is used to compute the parallel wavenumber from the turbulent spectrum given the tilting angle $\hat{\theta}_0$ as an input parameter. Unfortunately, it is not possible to find the angle self-consistently, because TGLF is a local model and does not contain global effects. It is possible to obtain $\hat{\theta}_0$ from gyrokinetic global simulations, and this work has been done [70] for a few plasma conditions, but such simulations are very computationally demanding and are not suitable for extensive studies. At the same time, the range of values used in this work is consistent with the results of global modelling. After $k_{\|}$ is computed, the residual stress calculation generally follows the logic presented above, but in real geometry.

5.2 Rotation modeling setup

The ASTRA transport code is used, coupled to the TGLF transport model and the drift-kinetic solver NEO. The discharges simulated are the same as described in Sec. 3.2.2. The modelling setup is also similar, though a few differences require mentioning. The profiles of current density, electron and ion temperatures evolve freely and consistently with the related transport coefficients, until an equilibrium is reached. The electron density evolution is allowed, but the time scale is set to very long (by means of an additional diffusivity as described in [74]). This way the density profiles may vary and eliminate any inconsistencies with the transport coefficients, but stay very close to experimental. This is important, because the tilting mechanism seems to be sensitive to density gradients, and a little modification of the density profile might lead to a significant change in the required tilting angle θ_0. Boron is included as single impurity species, with density defined by the same effective charge scaling, $Z_{\text{eff}} = 1 + 3.2 I_{\text{p}}^3 / \bar{n}_{\text{e}}^3$ (I_p in MA, n_e in $10^{19}\,\text{m}^{-3}$). The impurity concentration profiles are assumed flat. This assumption is verified with separate impurity transport simulations, presented in Sec. 5.7. Such amount of attention to the impurity content is paid due to its effect on turbulence, especially ITG, which has been shown previously, in Sec. 4. A model for sawtooth instability implemented in this work is Kadomtsev-type [75] and results in the current profile flattening in the core, with consequences on the Ohmic power profile. The heat conductivities at the edge are modified in the same way as described in Sec. 4.

Another notable difference is the radiated power model. Recently recovered soft x-ray measurements demonstrated that the major radiated power comes from the edge and the SOL. Fig. 5.2 shows some of these measurements with dashed lines. Although individual profiles vary, they typically can be decomposed into a roughly flat part and a bump on top of it that reaches its maximum at the edge and continues to the SOL.

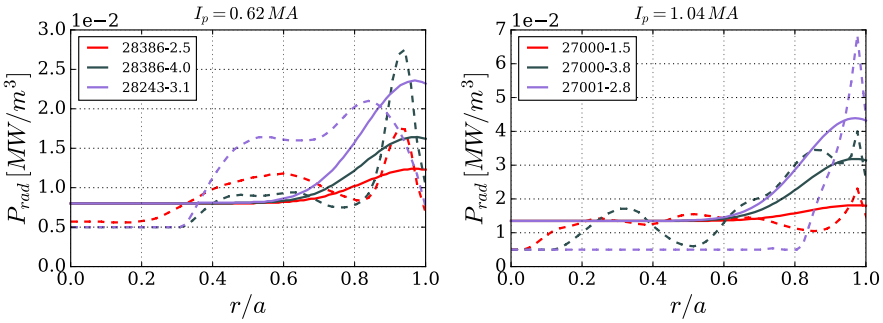

Figure 5.2: *Radiated power profiles measured with bolometric diagnostics (dashed) and its approximation used in the modeling (solid), shown for three different mean densities in each case.*

Following this observation, a scaling has been designed in the form

$$P_{rad} = 0.013 I_p + 0.001 n_{e,0}^2 \exp\left(\frac{1-x}{0.02}\right), \tag{5.11}$$

valid for all discharges under consideration. The resulting profiles are shown in Fig. 5.2 with solid lines. When integrated over the plasma volume, both the measured and the fit radiation profiles amount to roughly 60% of the total radiated power, measured separately. The difference is considered to be radiated from the SOL, which does not enter this modeling. The presented approach is somewhat different from that used in the energy confinement time modeling, where the radiation profiles were computed by ASTRA subroutine assuming tungsten to be the radiation source. However, no effect has been noticed on the resulting temperature profiles, presumably due to the stiffness of turbulent transport.

The momentum transport part of the model is as follows. ASTRA solves the momentum transport equation (5.1) for the parallel fluid velocity of deuterium $u_\parallel$, the toroidal velocity is taken as a projection:

$$v_\varphi(r) = \frac{R_0 + \Delta_S + r}{R_0} u_\parallel(r),$$

where R_0 is the tokamak major radius, Δ_S is the Shafranov shift of flux surfaces and r is average minor radius of the flux surface (to be distinguished from ρ introduced previously). This is an approximation of a more general expression $v_\varphi = u_\parallel B_0/B_\varphi$, which is valid for L-mode plasmas where $J \approx 1$ (see the definition below), because the poloidal beta $\beta_\theta = \beta\, q/\varepsilon$ is small. In order to be able to compare to the CXRS-measured velocity profiles, the deuterium-boron differential rotation is accounted for, so that $V_D = V_B + V_{dif}$ (see details in Sec. 5.3). The boundary condition for the parallel velocity is set at $r/a \approx 0.8$, where also the last experimentally measured value of v_φ is obtained. The momentum diffusivity (viscosity) $\chi_\parallel$ is related to the ion heat conductivity as $\chi_\parallel = P_r \cdot \chi_i$ with P_r the Prandtl number, which, when computed gyrokinetically, takes

values around unity. There have been experimental studies suggested P_r to be in the range 0.6 - 2 for various plasma conditions [18, 76], but normally somewhere below 1. Here we use the value $P_r = 0.9$, but set an additional limit $\chi_\parallel > 0.5\,\mathrm{m}^2/\mathrm{s}$, in order to avoid unlimited acceleration. This additional restriction only affects the plasma at $r/a \approx 0.2$, between the radial regions of high sawtooth activity and developed turbulence.

ASTRA computes the diffusion and pinch fluxes terms of equation (5.1) as:

$$\Gamma_{dif} = \frac{R_0}{J} \left\langle (\nabla\rho)^2 \right\rangle \rho_m \chi_\parallel u'_\parallel, \tag{5.12}$$

$$\Gamma_{pin} = \frac{R_0}{J} \left\langle (\nabla\rho)^2 \right\rangle \rho_m V_p u_\parallel, \tag{5.13}$$

where $J = I_{pol}/R_0 B_0$ is the normalized poloidal current function, ρ_m is the mass density, $u'_\parallel = -R\nabla_r u_\parallel / v_{th,i}$ is the normalized gradient of the parallel velocity. The pinch velocity V_p can be defined as

$$V_p = -\frac{1}{R_0}\chi_\parallel \sqrt{\varepsilon} \left(\frac{1}{2} R/L_n + 2.7 \right), \tag{5.14}$$

following the analysis in [77, 78]. If the residual stress term is provided, ASTRA uses it in the transport equation, as well.

TGLF produces the stress tensor as a sum of the diffusive (diagonal) and the residual parts. Therefore, before using it in the momentum transport equation one has to subtract the diffusive part to avoid double counting. A problem might arise here, since the diffusion term (5.12) may differ from that of TGLF. Test simulations have shown that the TGLF total stress is close to zero in the core, inside $r/a \approx 0.2$, especially in low density plasmas, so a subtraction would lead to a cancelation of explicit ASTRA diffusion and an unstable behavior of the velocity profile. To avoid this, the Heaviside function h(0.2) is applied on the subtracted expression. The value 0.2 is fixed for simplicity, even though the position where the stress vanishes may vary. Another measure used here for stability is a slight increase of $\chi_\parallel$ before it is inserted into TGLF (by approx. $0.1\,\mathrm{m}^2/\mathrm{s}$). In the following, the residual stress discussed is the difference between the TGLF stress tensor and the diffusive term.

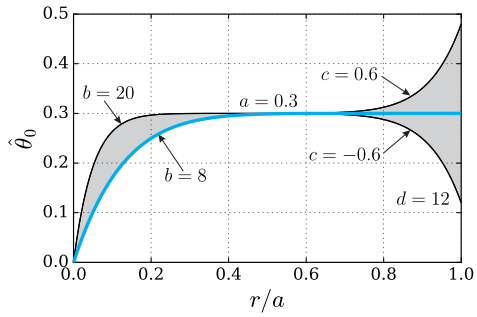

Figure 5.3: *Tilting angle scaling*

The choice of the tilting angle profile is defined by several limiting considerations.

On the magnetic axis it is expected $\theta_0 = 0$ for symmetry reasons, also since the pressure profile is flat there. It can increase towards the edge, but not exceed $\pi/2$, which would mean purely poloidal structure. Close to the edge θ_0 may decrease again, due to the strong turbulence self-organization aiming to enhance the transport. having this in mind, it is decided to represent the tilting angle by a general expression

$$\theta_0 = a(1-r)^b + cr^d, \tag{5.15}$$

which yields shapes shown in Fig 5.3 with θ_0 measured in radians (for a given value $a = 0.3$). Various parameter values have been tested. Interestingly, almost no effect has been noticed upon variation within the limits shown by the shaded regions. What matters the most is the value around the mid-radius, where $\theta_0 = a$. In the final simulations, no edge variation is assumed, $c = 0$, and a modest core increase rate with $b = 8$ is chosen. The profile adjustment to match the measured velocity profile is done by varying the a parameter alone. More discussion on the $\hat{\theta}_0$ profile shape is given in Sec. 5.4.

5.3 Toroidal differential rotation

We make a particular stress on the fact, that the CXRS measurements of the toroidal rotation result in a velocity profile for the chosen impurity species (in our case boron) and not the main plasma ions. While it is usually assumed that the difference between the rotation velocities of the two species is negligible, a stricter approach would be to account for the differential rotation as it appears in neoclassical theory. A simplified expression for the differential rotation frequency is derived in [72] under the assumption of low impurity concentration. It takes the form

$$\omega_{Imp} - \omega_i = \frac{3}{4} K_2 \frac{v_{th,i}}{R} \frac{\rho_{ip}}{L_{T_i}} \tag{5.16}$$

where $\rho_{ip} = m_i v_{th,i}/Z_i e B_p$, and K_2 is a function of the plasma collisionality, aspect ratio and impurity concentration, in our case K_2 varies from zero on the magnetic axis to $0.65 < K_2 < 0.7$ at the edge.

Fig. 5.4 compares the toroidal velocity difference obtained with formula (5.16) and with NEO in the high current case. The two match to a reasonable degree up to $r/a = 0.8$, while higher discrepancy is observed further towards the edge. So, a good approximation is available without any noticeable additional computational demands. Still, since NEO also provides poloidal velocities for both ion species, which are an important ingredient to compute the neoclassical corrections Δ_{neo}, in our calculations we implement the NEO code, that directly solves the drift-kinetic equation.

The importance of accounting for the differential rotation can be easily proven. The typical values are of the order of several km/s, that in the considered case of ohmic plasmas amounts to up to tens of percent of the boron toroidal rotation velocity.

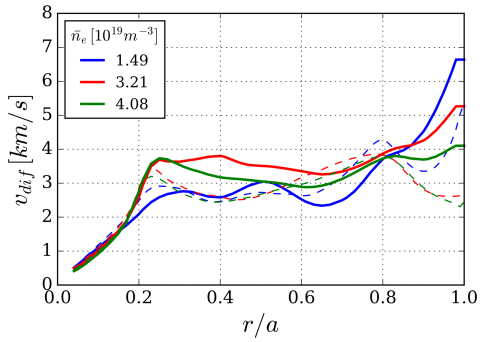

Figure 5.4: *Toroidal differential rotation of main deuterium plasma and boron impurity ($V_D - V_B$) from NEO (solid lines) and simplified formula (5.16) (dashed lines)*

Additionally, for hollow velocity profiles this shifts radially the point of $V_\varphi = 0$, that leads to a different distribution of the radial momentum flux caused by the convective term.

A typical feature of CXRS-measured profiles is the flattened central region, and the differential rotation profile increases up to approximately the same radial point, so the derived deuterium velocity would decrease towards the axis monotonously. In fact, the differential rotation in the center up to $r/a \approx 0.25$ is mainly defined by R/L_{T_i} through the dependence of deuterium poloidal velocity on its temperature gradient. Considering inaccuracies in T_i measurements close to the magnetic axis, the compensation can be assumed exact. It would also provide a handy cross-check tool between V_φ and T_i measurements, if one assumes that the radial position where the boron velocity profile bends is the same as where the L_{T_i} profile does.

5.4 Rotation simulation results

With the approach described above it is possible to reproduce the observed velocity profiles to a good accuracy, finding a proper tilting angle for each plasma state. The results are presented in this section in the following way: the values averaged over $r/a = 0.4 - 0.6$ are shown with black dots for each simulated plasma state. Five states in each current case are selected and shown in color that represent typical regimes. For these selected cases also the profiles of the important quantities are presented.

Some simulated toroidal velocity profiles in comparison with the measurements for the density scan at $I_p = 0.62\,\mathrm{MA}$ are presented in Fig. 5.5. With the boundary condition set at $r/a = 0.8$, the simulated rotation profiles and, more importantly, their mid-radius gradients are close to experimental. The gradient region extends approximately from 0.2 to 0.7 of the normalized radius, and they all feature a central bump inside $r/a = 0.2$, as discussed previously.

Fig. 5.6 presents the corresponding simulations parameters for the lower current case. Subfigure 5.6, *a* shows the $\hat{\theta}_0$ mid-radius value used as TGLF input, subfigure 5.6, *b* presents the simulated normalized velocity gradient u' averaged over

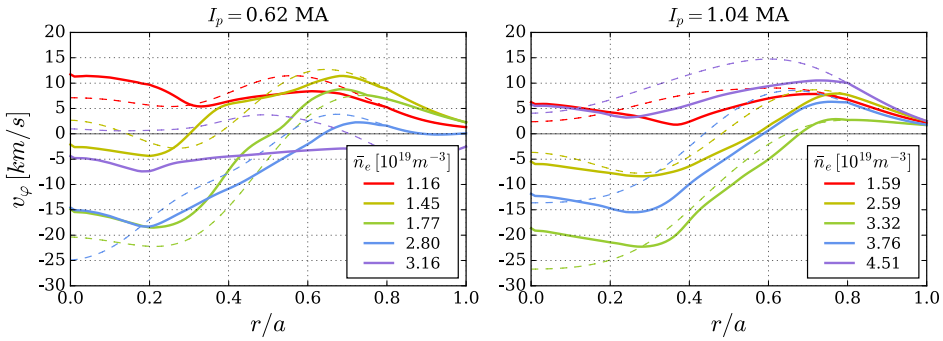

Figure 5.5: *Comparison of the boron toroidal velocity profiles as measured (dashed) and simulated (solid) at* $I_p = 0.62\,\mathrm{MA}$ *(left) and* $I_p = 1.04\,\mathrm{MA}$ *(right).*

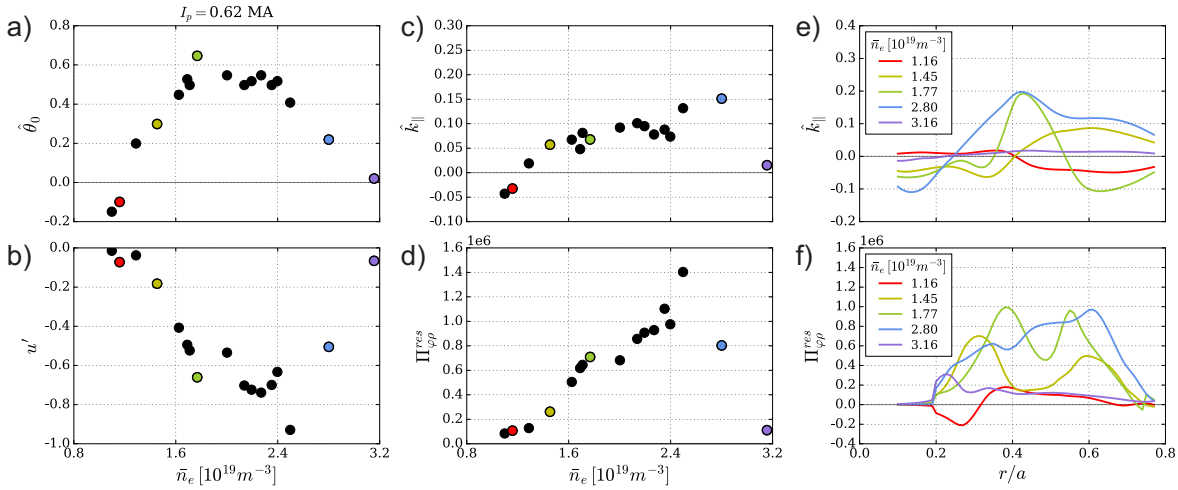

Figure 5.6: *Simulation parameters at* $I_p = 0.62\,\mathrm{MA}$*: a) input tilting angle, b) simulated* u'*, c) averaged parallel wavenumber* $\langle \hat{k}_\parallel \rangle$ *from TGLF, d) residual stress* $\Pi^{res}_{\varphi\rho}$ *from TGLF; e and f) radial profiles of* $\langle \hat{k}_\parallel \rangle$ *and* $\Pi^{res}_{\varphi\rho}$ *for the colored data points*

$r/a = 0.4 - 0.6$. The values of $\langle \hat{k}_\parallel \rangle$ and $\Pi^{res}_{\varphi\rho}$ produced by TGLF are shown in subfigures 5.6, *c* and *d*, and subfigures 5.6, *e* and *f* present the radial profiles of these quantities for the five "colored" plasma states (residual stress is actually "residual", with diffusion extracted). Interesting to note that $\hat{\theta}_0$ varies with the increase of density in a complicated manner, starting from slightly negative values at low density, increasing to ≈ 0.5 around the density of maximum R/L_n and LOC-SOC transition, and then gradually falling down below 0.1 at the highest density achieved in the experiment. At the same time, $\langle \hat{k}_\parallel \rangle$ and $\Pi^{res}_{\varphi\rho}$ scale roughly linearly to n_e and to each other. They also reach a maximum and then fall down, but at a considerably higher density than $\hat{\theta}_0$. This suggests that the analytic approximation $k_\parallel \propto \theta_0$ is only valid at low density. The trend shown by the residual stress is identical to that of u'. The profiles of $\langle \hat{k}_\parallel \rangle$ and the residual stress show rather complicated and irregular structures and are not directly correlated, only in the average amplitude. The profiles' behavior outside 0.8 of the normalized radius has no effect on the toroidal velocity due to the boundary

condition.

The initial hypothesis related the momentum transport mechanism to turbulent structures tilting, therefore it is reasonable to correlate the obtained tilt angles to the turbulence characteristics of the corresponding plasma conditions. Fig. 5.7 presents the evolution of the dominant turbulent mode real frequency in three radial positions, somewhat similar to Fig. 4.13. As already discussed in Sec. 4.2.6, at low density most scales are dominated by electron modes (TEM in the considered range), while with the density increasing ITG takes over. The TEM-ITG transitions occur at various radial positions at different densities (collisionalities). The transition range of density coincides with that where $\hat{\theta}_0$ increases. We may assume that small negative angles $\hat{\theta}_0 \approx -0.1$ are a TEM feature, while $\hat{\theta}_0 \approx 0.5$ is typical for ITG, since it is reached when ITG takes over most of the plasma core. At high density, the gradual reduction of the poloidal tilting may be explained by increased radial alignment of strong ITG turbulence. In principle, for the same reason the tilting should decrease close to the edge.

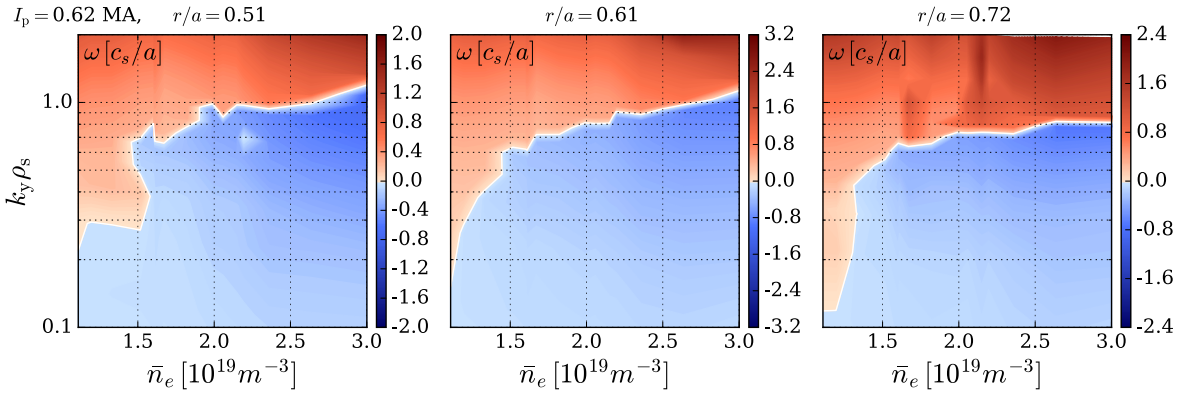

Figure 5.7: *Dominant mode real frequency ω in the range $k_y\rho_s = 0.1 - 2$ for the case $I_p = 0.62\,MA$ for three radial points: 0.5, 0.6 and 0.7.*

To support this idea, Fig. 5.8 shows the evolution of turbulence real frequency ω at three mean density values along the TEM-ITG transition, resolving it radially and presenting a picture similar to Fig. 4.14. These three states correspond to $\hat{\theta}_0$ values -0.1, 0.3 and 0.6, respectively. Note, that the low-k positive frequency spot at the edge is a modelling artifact, since the boundary was fixed at $r/a = 0.8$ and affected the density gradient there. The feature is absent in Fig. 4.14, where the boundary was set at the separatrix.

It should be noted that setting positive $\hat{\theta}_0$ at low density or negative $\hat{\theta}_0$ at high density in the simulations would result in a negative residual stress, which would drag the core rotation in the co-current direction. Taking into consideration that TEM and ITG modes propagate in opposite poloidal directions, it can be assumed that the turbulent residual stress depends on ω, or at least its sign.

Figure 5.9 shows the simulation parameters for plasmas at $I_p = 1.04\,\mathrm{MA}$. All the features discussed for the Fig. 5.6 present here as well, but shifted to higher mean

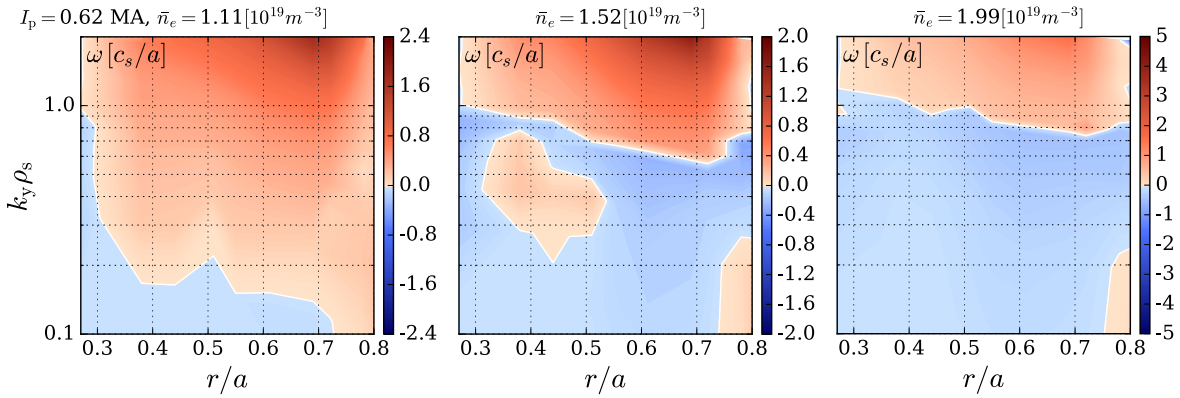

Figure 5.8: *Dominant mode real frequency ω in the range $k_y\rho_s = 0.1 - 2$ for the case $I_p = 0.62\,\mathrm{MA}$ for three mean densities along the transition from TEM to ITG-dominant*

density values. Here the region of "high density, flat rotation" plasma states is presented by several data points, while the region of TEM-ITG transition has rather poor resolution in the density scan. Both u' and $\hat{\theta}_0$ reach slightly lower maximum values than at the lower current, but $\hat{k}_\parallel$ profiles are very similar, and the residual stress is notably larger.

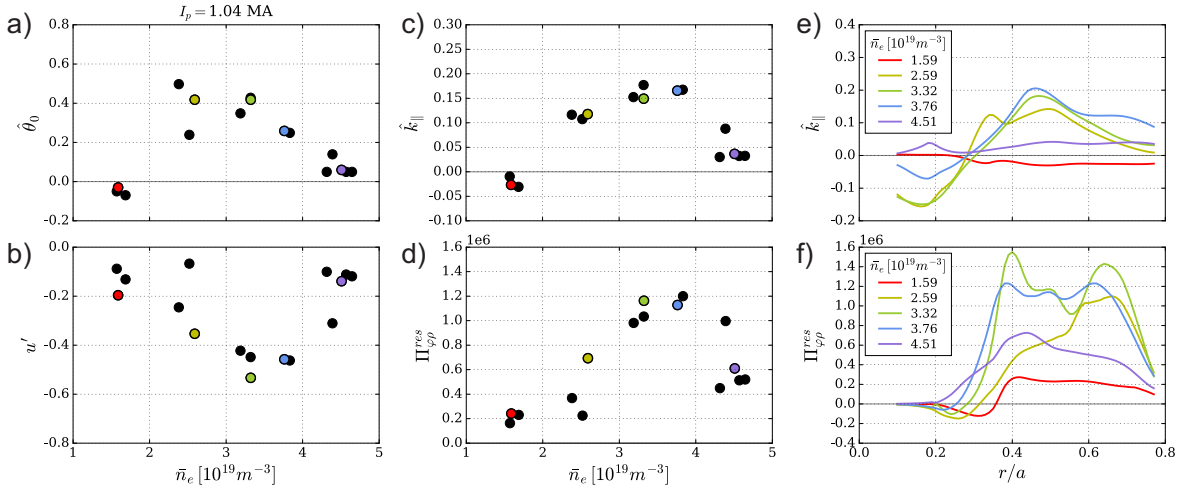

Figure 5.9: *Simulation parameters at $I_p = 1.04\,\mathrm{MA}$: a) input tilting angle, b) simulated u', c) the averaged parallel wavenumber $\langle\hat{k}_\parallel\rangle$ from TGLF, d) the residual stress $\Pi^{res}_{\varphi\rho}$ from TGLF; e and f) radial profiles of $\langle\hat{k}_\parallel\rangle$ and $\Pi^{res}_{\varphi\rho}$ for the colored data points*

A R/L_n-scaling of u' has been suggested previously [12, 13]. Indeed, as has been demonstrated in Sec. 4.2.5, the density peaking maximizes at about the same mean density as u', with the latter shown to scale as $\hat{\theta}_0$. Both of these processes are attributed to the transition from TEM to ITG dominant mode. At higher densities the peaking is also reduced, when ITG is strong in the plasma core. A weaker experimental dependence of u' on the logarithmic temperature gradients has also been reported in [13]. In this work it has been shown (see Fig. 4.6 in Sec. 4.2.1) how R/L_{T_I} varies

along the density ramp-up, and a correlation with $\hat{\theta}_0$ can indeed be found. However, it does not contradict the hypothesis of the turbulent nature of the residual stress, but rather may give a hint on the details. For example, a reduction of $\hat{\theta}_0$ at high density may be explained by stronger ITG turbulence, among other factors due to an increase in R/L_{T_i}.

5.5 Parametric scans study

In order to study in more detail how $\langle \hat{k}_\parallel \rangle$ scales with $\hat{\theta}_0$ and find other relevant factors, a single plasma state has been chosen with high velocity gradient (#27000, $t = 4.1\,\mathrm{s}$, $\bar{n}_e = 3.3 \times 10^{19}\, m^{-3}$), and $\hat{\theta}_0$ has been varied from below 0 to the fitting value (0.42 in this case) and beyond that, up to 0.8. The model has not been changed, it constrains the density profile variation and allows free evolution of electron and ion temperatures and the parallel velocity. Additional attention has been paid to the heat conductivities. It is known that a shift of turbulent eddies from radial alignment reduces their heat transport effectiveness. This can be caused not only by the profile shearing mechanism, but also by the flow shearing, i.e. finite gradient of toroidal or poloidal velocity. The effect of finite $\hat{\theta}_0$ and flow shearing can be estimated separately, if the rotation profile is fixed to experimentally measured, but the tilting is set to zero.

The results of these exercises are presented in Fig. 5.10. Subfigures a, c and e show the dependence of the normalized rotation gradient, parallel wavenumber and the residual stress (all averaged over $r/a = 0.4 - 0.6$) on the tilting angle, respectively. Subfigures b, e and f show the radial profiles of the corresponding quantities. The dashed black lines and circles represent the pure velocity shearing effect at experimental v_ϕ and $\hat{\theta}_0 = 0$ (for u' it is simply the experimental value). The vertical green lines mark $\hat{\theta}_0 = 0.42$.

At low tilting angles, $|\hat{\theta}_0| \leq 0.3$, the system response is linear to a high extend. Moreover, it seems symmetric under the sign flip of the tilting, with negative angles leading to rotation drive in the opposite direction. At $\hat{\theta}_0 > 0.3$ the parallel wavenumber does not increase linearly anymore, it starts to degrade. The residual stress continues to increase, but in a different manner: instead of a broad bump between the normalized radius points 0.3 and 0.8, there appears a single peak around $r/a = 0.55$. At $\hat{\theta}_0 > 0.7$ $\Pi^{res}_{\varphi\rho}$ demonstrates a rapid rise, and the core rotation velocity exceeds $10^5\,\mathrm{m/s}$ (not shown on the plot). The linear part resembles the LOC phase evolution, as well as the late SOC phase (reversed).

The ion heat conductivity variation with the tilting angle is shown in Fig. 5.11. Note, that only the turbulent contribution changes, while the neoclassical part is not affected, but the latter is roughly one order of magnitude smaller. Fig. 5.11 also presents the central ion temperature values, in order to see the effect of changing χ_i on a measureable quantity. The χ_i demonstrates only little variation up to moderate tilting angle values, $\hat{\theta}_0 \leq 0.4$. After this point, a notable reduction occurs, which also

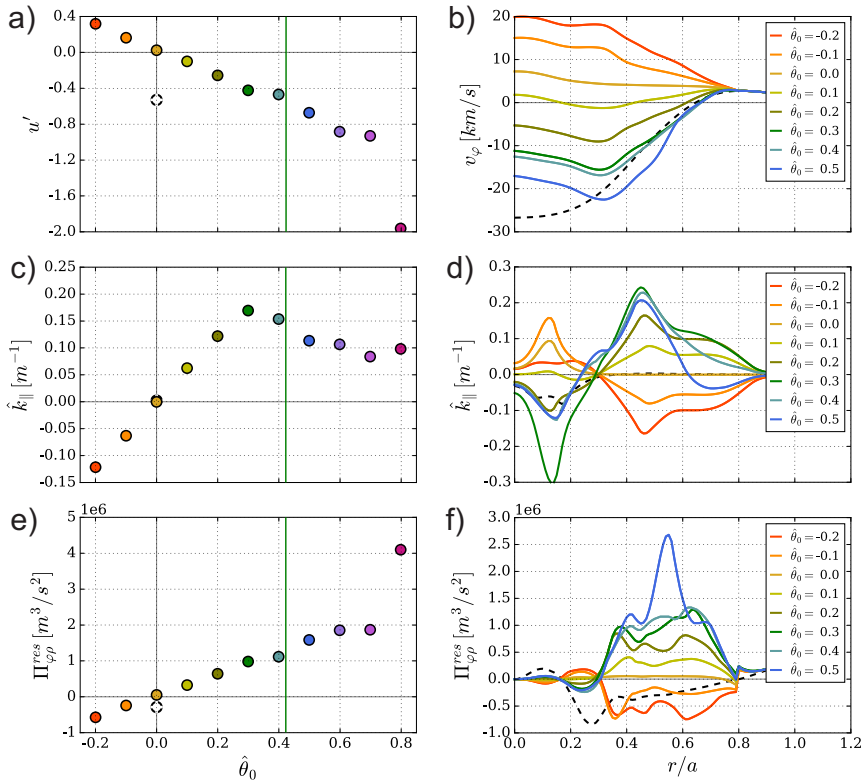

Figure 5.10: *Scan of the tilting angle for plasma parameters: a) normalized mid-radius rotation gradient u' and b) the corresponding toroidal rotation velocity profiles, c) the mid-radius averaged parallel wavenumber $\langle \hat{k}_\parallel \rangle$ and d) its radial profiles, e) the mid-radius averaged residual stress $\Pi^{res}_{\varphi\rho}$ and its radial profiles.*

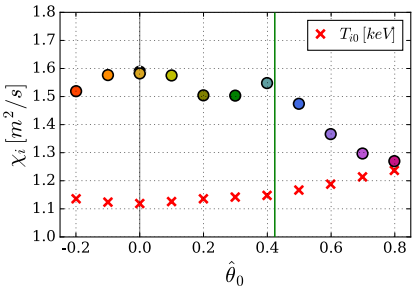

Figure 5.11: *Mid-radius ion heat conductivity as a function of the tilting angle, and the corresponding central ion temperature*

leads to a slight ion temperature rise. However, considering the usual experimental error bars on T_i around 10% and the experimentally relevant range of $\hat{\theta}_0 < 0.5$, this effect seems too small to serve as an indicator of the turbulence tilting in Ohmically heated plasmas. The velocity shearing effect alone has a negligible influence on χ_i.

There is likely a mutual impact of the residual stress and the ion heat conductivity, which is related via the Prandtl number to the viscosity $\chi_\parallel$. Velocity shearing reduces $\chi_\parallel$, it leads to larger velocity gradient that shears the turbulence even more. This might explain an abrupt increase of $\Pi^{res}_{\varphi\rho}$ at large tilting angles, however the

corresponding high rotation velocities have not been observed experimentally, which suggests that the related range of parameters ($\hat{\theta}_0 > 0.7$) has not been reached.

The analysis above concludes that $\langle \hat{k}_\parallel \rangle \propto \hat{\theta}_0$ at small tilting angles, but also suggests that in general the function $\hat{k}_\parallel(\hat{\theta}_0)$ is not just linear, but rather $\langle \hat{k}_\parallel \rangle = \hat{\theta}_0 \cdot f(...)$, where parentheses may include mode growth rates and frequencies, which are also the functions of $\hat{\theta}_0$. This explains the linearity of $\hat{k}_\parallel$ at tilting close to zero and the non-linearity at larger $\hat{\theta}_0$. Also, $\langle \hat{k}_\parallel \rangle$ is the integral value over all $k_y \rho_s$, and the impact of tilting at different scales may vary.

An exercise has been performed to investigate the effect of various plasma parameters on $\langle \hat{k}_\parallel \rangle$. The method is similar to that described in Sec. 4.2.7, it consists in the modification of single quantities in the TGLF input files. In this study the values are not taken from other plasma states, but represent a scan over some realistic range. The quantities tested are: logarithmic gradients of density R/L_n, electron temperature R/L_{T_e} and ion temperature R/L_{T_i}, the temperature ratio T_i/T_e, collisionality ν_* and the effective charge Z_{eff}. Since the momentum transport mechanism may depend on the dominant turbulence mode, two plasma states at have been studied: an early LOC phase with $n_e = 1.6 \times 10^{19}\,\text{m}^{-3}$, $\hat{\theta}_0 = -0.07$, and an early SOC phase with $n_e = 3.2 \times 10^{19}\,\text{m}^{-3}$, $\hat{\theta}_0 = 0.35$, both at $I_p = 1.04\,\text{MA}$. These plasma states have already been shown to be dominated by TEM and ITG, respectively.

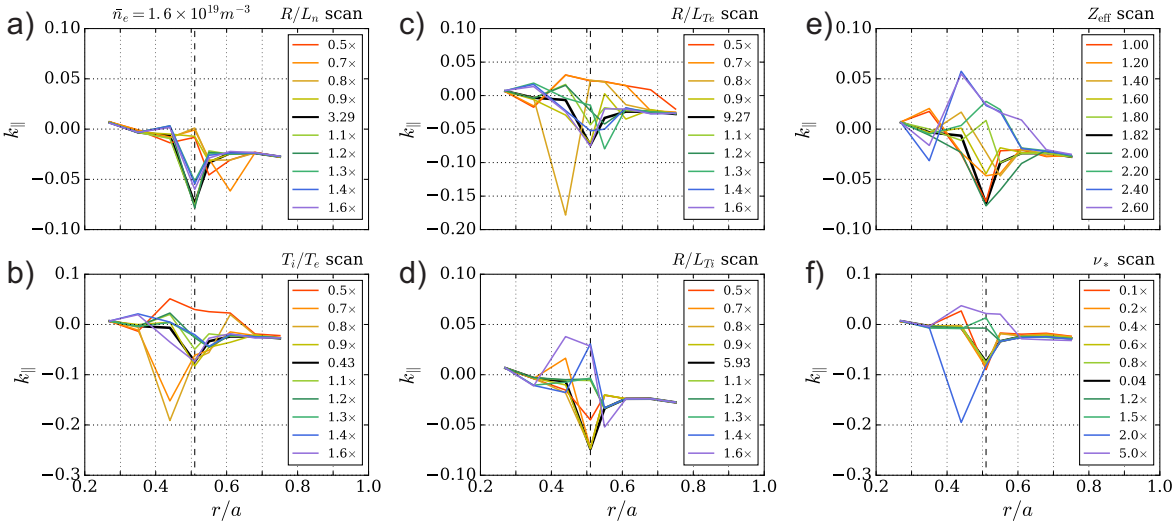

Figure 5.12: *Parameter scans of $\hat{k}_\parallel$ for a TEM-dominated plasma*

The illustrating plots for the TEM state are collected in Fig. 5.12, for the ITG state – in Fig. 5.13. They present radial profiles of $\hat{k}_\parallel$ rather than single or averaged values, in order to resolve a radial shift of the profile peak that occurs in some cases. The default, natural $\hat{k}_\parallel$ is denoted by a thick black line, it is the same in all the plots. The corresponding number in the legend shows the natural parameter value at the radial position of the dashed black vertical line, i.e. around $r/a = 0.51$. Colored lines represent $\hat{k}_\parallel$ profiles obtained with the control parameter changed by a factor (except

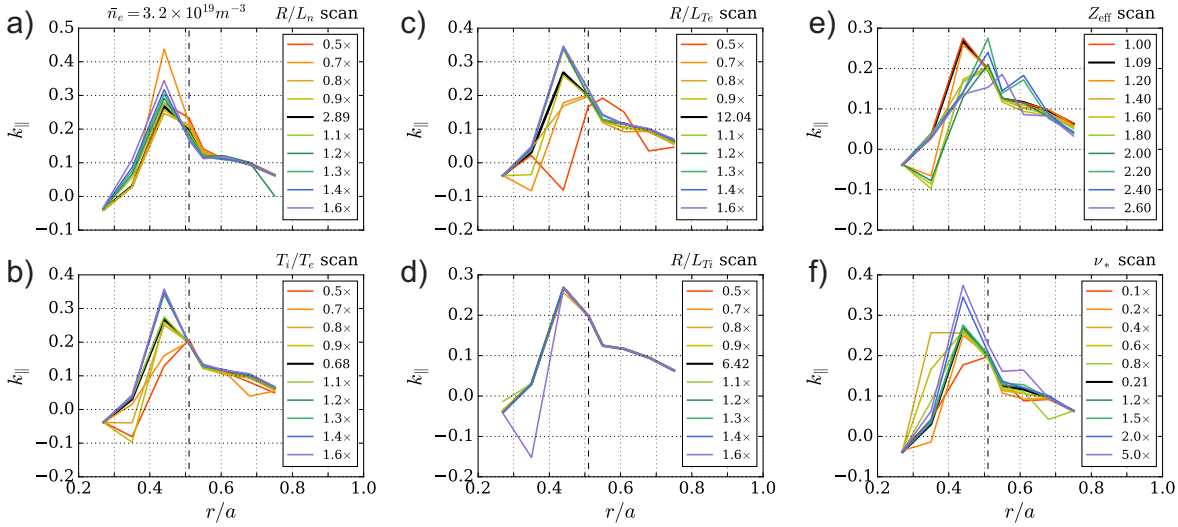

Figure 5.13: *Parameter scans of $\hat{k}_\parallel$ for an ITG-dominated plasma*

for Z_{eff}) over its whole radial profile. For R/L_n, R/L_{T_e}, R/L_{T_i} and T_i/T_e the factors vary from 0.5 to 1.6, for the collisionality the range is from 0.1 to 5. Scaling of the effective charge is done over a range of fixed values, from 1.0 to 2.6, and the Z_{eff} profile is flat.

The parameter dependencies presented are rather complicated, but some meaningful trends can be identified over limited parameter ranges. For example, in the TEM case, increasing R/L_{T_i}, Z_{eff} or ν_*, or reducing R/L_{T_e} moves $\hat{k}_\parallel$ towards positive values. In the ITG case, the maximum $\hat{k}_\parallel$ scales positively with R/L_n, R/L_{T_e}, T_i/T_e and ν_*, while higher impurity concentration tends to decrease it. Additionally, $\hat{k}_\parallel$ is insensitive to the ion temperature gradient in the ITG regime. Generally, one can conclude that there can not be a direct relation between $\hat{\theta}_0$ and u', the residual stress generation mechanism is complex, and many factors are involved.

5.6 Conclusions on momentum transport modeling

The working assumption of this study was the residual stress generation mechanism through the poloidal tilt of the turbulent global mode structure due to the radial variation of equilibrium plasma profiles. Simulations of L-mode Ohmic plasmas in AUG at various conditions have been performed with ASTRA-TGLF-NEO system, supported by experimental measurements. A proper account for the difference in the toroidal rotation velocity of deuterium and boron is made, which has been usually neglected in the past.

The modelling has yielded the tilting angle $\hat{\theta}_0$ values necessary to explain the observed plasma toroidal velocity profiles, namely the transitions from flat to hollow shape and back with the increase of plasma density. Those are in a general agreement with the results of non-linear gyrokinetic modeling with GKW of the same plasma condi-

tions described in [70]. A relation of the tilting to drift-wave turbulence characteristics is suggested. The picture seems consistent with experimentally observed scaling of the normalized rotation gradient u' with the normalized density gradient [12, 13].

The results generally confirm the fluid equations relating the residual stress, the mean parallel wavenumber $\langle \hat{k}_\parallel \rangle$ and the tilting angle at low $\hat{\theta}_0$, even though the relation between $\langle \hat{k}_\parallel \rangle$ and $\hat{\theta}_0$ is found to be more complicated than linear. Dependencies of $\langle \hat{k}_\parallel \rangle$ on a number of plasma parameters have been studied with TGLF parametric scans, confirming complexity of the residual stress generation mechanism.

5.7 Simulation of boron density profiles

It was assumed in the modelling of L-mode Ohmic discharges that boron is the only impurity in the plasma, and that the corresponding plasma effective charge follows the proposed scaling 4.5. It was also assumed that the concentration of boron is radially constant. This assumption is based on the modelling of boron transport, which results are presented in this section.

The boron transport simulations for the same discharges feature fully self-consistent evolution of electron and ion temperatures, as well as electron and boron densities, so TGLF treats boron as kinetic species. Both electron and boron density are modelled with a free boundary value, defined by a prescribed edge flux. The boron source was adjusted for each data point so that the average Z_{eff} matches to the experimental scaling. Plasma rotation is modelled in accordance with the setting described in the previous section.

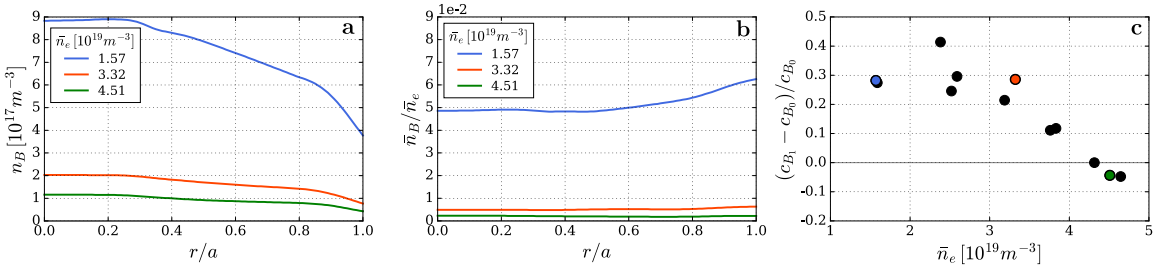

Figure 5.14: *Simulated boron density, concentration and the profile hollowness factor at* $I_{\text{p}} = 1.04\,MA$

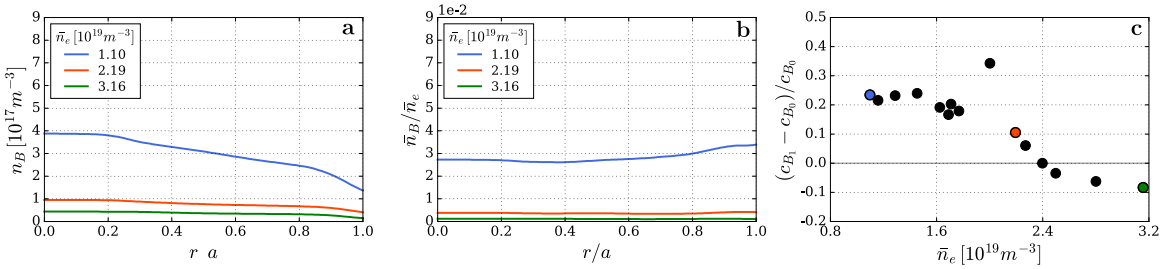

Figure 5.15: *Simulated boron density, concentration and the profile hollowness factor at* $I_{\text{p}} = 0.62\,MA$

The resulting boron density profile and the boron concentration profile for the case with $I_{\text{p}} = 1.04\,MA$ are shown in Fig. 5.14 (*a*, *b*). At low density, more impurity is accumulated at the edge, leading to a concentration profile with $\approx 30\%$ hollowness, see Fig. 5.14, *c*. As the electron density increases, boron distributes more uniformly, and at $\bar{n}_e \geq 4\times10^{19}m^{-3}$ its concentration is effectively flat. In the plasmas with $I_{\text{p}} = 0.62\,MA$ (Fig. 5.15) such uniformity is reached already at $\bar{n}_e \geq 2.2 \times 10^{19}m^{-3}$. Since the deviation from uniformity is only observed at the plasma edge, the approximation of flat boron concentration is consistent with the model predictions.

Chapter 6

Conclusions

The aim of this work is a detailed analysis of transport processes in L-mode tokamak plasmas, for which the understanding of physical mechanisms is missing or not complete. The analysis is done via integrated modelling of actual plasma discharges performed in the ASDEX Upgrade tokamak, employing the ASTRA-TGLF modelling package. The major questions that have been posed before us, are:

- What causes the saturation of the energy confinement time in Ohmically heated plasmas? Does the dominant turbulence regime fully define the energy confinement time scaling? What is the role of the impurity concentration?
- What is the dominant mechanism of spontaneous toroidal rotation in tokamak plasmas? What are the crucial plasma parameters that control the magnitude of this effect?

On the other hand, thorough modelling serves as a validation of the TGLF transport model against experimental measurements, which is an essential stage in the process of development of physical models. The degree of agreement of the measured and predicted plasma parameters can support the model correctness or point out the possible issues.

6.1 Summary of results and outlook

The analysis of plasma simulations during density ramps allowed us to relate the energy confinement time evolution with the properties of core plasma turbulence. It has been shown that the plasma core at low density is dominated by TEM turbulence, while the ITG mode is stable, and the ion channel of turbulent heat transport is weak. With the increase of density, TEM is suppressed by higher collisionality, ITG is destabilized and starts to dominate both electron and ion heat transport channels. Switching of different k_y-scales between TEM and ITG dominance occurs gradually both along the radial coordinate and the density scan, with the mid-radial region switching the last. The latter is accompanied by the maximum in the density peaking factor, which is

the ratio of the central density to the volume averaged value. The energy confinement time saturation is observed as the ITG-driven heat transport keeps increasing, when TEM is already well subdominant. The hypothesis of direct relation between TEM-ITG dominant mode shift to LOC-SOC confinement regime transition has not been confirmed. As the collisionality increases, the T_e-T_i coupling becomes stronger, and more thermal energy is transferred from the electrons to the ions. At low density, heat transport in the electron channel is reduced, while the ITG mode that dominates the ion channel is still weak. Hence, the total pressure in the core increases linearly with the density. The increase of R/L_{T_i} and the reduction of impurity concentration lead to ITG enhancement. The ion heat transport is strongly stiff and effectively exhausts the thermal energy, so the total pressure in the plasma core saturates or starts to degrade, and so does the energy confinement time.

The impurity content is confirmed to be an essential ingredient in the modelling of plasma turbulence. It acts through dilution to stabilize the ITG at lower densities, when impurities are more abundant. The observed scaling of Z_{eff} with electron density and plasma current correlates with the dependence of the energy confinement time on these parameters. Additional impurity seeding reduces the turbulent heat flux in the ion channel via ITG stabilization at higher densities and thereby can shift the plasma to the IOC phase. It is demonstrated that high impurity content modifies the spectrum of the most unstable modes, keeping ITG stable up to much higher electron density if compared to the clean plasma. The best confinement improvement at high density has been reached with $Z_{\text{eff}} \approx 3$. Some additional core ECR heating will reduce the electron-ion coupling and also improve the L-mode confinement. However, the dilution of main ion fraction makes the IOC regime unsuitable for fusion production, as the reaction rate drops accordingly. The modelling of radial transport of low-Z impurities represented by boron demonstrated the radial variation of its equilibrium concentration. It has been shown to be hollow at low density and flatten out as the density increases, with the approximation of radially constant concentration generally reasonable.

In general, the physical picture drawn by these simulations is consistent. The LOC-SOC transition has posed an open question for many years, and this work provides a detailed answer, confirming some of the previous results and providing new insights into this complex phenomenology. In particular, it has been shown previously that the amount of impurities affects strongly the ITG turbulence intensity, and that ITG is responsible for the energy confinement time saturation. On the other hand, the problem has never been approached via an integrated modelling, which allowed us to demonstrate the complex interplay of effects described above. The fact that the real plasma conditions are modelled in an integrated manner is a necessity and at the same time an advantage to gain understanding on the cause-effect relationships.

In the study of intrinsic plasma toroidal rotation a global mechanism of residual stress formation due to profile shearing effect has been tested. Profile shearing here means the effect of finite radial variation of background plasma parameters on the

turbulent modes. In particular, it causes a poloidal shift of the maximum of potential fluctuations from the outward midplane, and the consequent tilting of turbulent eddies from the radial alignment. Such poloidal asymmetry of the distribution function (finite mean parallel wavenumber $\langle \hat{k}_\parallel \rangle$) enables a substantial momentum transport. As has been shown, this mechanism is able to explain the observed toroidal rotation profiles in AUG L-mode plasmas with the assumption of tilt angles in the reasonable range, $\hat{\theta}_0 \in [-0.1, 0.6]$ radians. The values required by TGLF to reproduce the experimental intrinsic rotation profiles are consistent with the results of non-linear global gyrokinetic simulation of the same plasma discharges. The evolution of the required tilting angle with the plasma parameters suggests its relation to the dominant turbulence type, which would explain the observed rotation reversal close to the density of maximum density peaking. The picture seems consistent with experimentally observed scaling of the normalized rotation gradient u' with the normalized density gradient. The results generally confirm the fluid equations relating the residual stress, the mean parallel wavenumber $\langle \hat{k}_\parallel \rangle$ and the tilting angle at low $\hat{\theta}_0$, even though the relation between $\langle \hat{k}_\parallel \rangle$ and $\hat{\theta}_0$ is found to be more complicated than linear. Dependencies of $\langle \hat{k}_\parallel \rangle$ on a number of plasma parameters have been studied with TGLF parametric scans, confirming complexity of the residual stress generation mechanism.

As an outlook, establishing an analytical model of the tilting angle $\hat{\theta}_0$ is needed, in order to properly account for it in local simulations. However, from the practical point of view, the conclusion can be drawn that high intrinsic rotation requires a substantial normalized density gradient, so in plasmas of ITER and beyond, where the density gradient in the core is expected to be small, the effect would be very weak. Also, modelling of a conventional fusion reactor (DEMO) even with strong turbulence tilting showed rather small residual stress. Note, that the edge toroidal velocity has not been modelled in this work, and its mechanisms are so far unclear, which also makes an important research topic.

6.2 Discussion on the transport modelling

The TGLF module of turbulence-driven transport for ASTRA has proven to be a powerful and comprehensive transport model, presenting an effective tool for turbulence modelling and analysis. In the simulations of L-mode Ohmic plasmas in ASDEX Upgrade, the self-consistent profiles of electron temperature and density match the measurements very accurately. A disagreement has been found between the predicted and measured ion temperature profiles, which may be a result of an underestimation of stiffness of the ion channel of energy transport. This discrepancy is shown to have little effect the conclusions of this work, but is an important concern itself. Overprediction of the ion temperature at high density has been an issue for other physical models, too, which might be a sign of some unaccounted effects.

The current setting of TGLF (saturation rule 1) features an edge transport model

for the electrons, but not for the ions, so some approximations and assumptions have to be made in this regard. Development of an improved edge transport model is hence of great importance. Consistent treatment of shear layers could advance QL transport models and allow them to also predict the L-H transition. Coupling to the SOL would also be advantageous, eventually leading to even higher degree of integration in the modelling, covering a whole power plant.

This work shows once again the advantage of integrated modeling with QL transport models to be fast at full plasma simulations in realistic conditions, even restricted to the local limit. A global version of, for example, TGLF would include the profile shearing effects, but it would require an extensive database of global non-linear gyrokinetic simulations for the model tuning, which is not considered practical in the community.

References

[1] A. J. Brizard and T. S. Hahm, Rev. Mod. Phys. **79**, 421 (2007)

[2] J. Candy *et al.*, Phys. Plasmas **11**, L25 (2004)

[3] F. L. Hinton and R. D. Hazeltine, Rev. Mod. Phys. **48**, 239 (1976)

[4] Greenwald M *et al.*, Phys. Rev. Lett. **53**, 352 (1984)

[5] J. Rice *et al.*, Phys. Plasmas **19**, 056106 (2012)

[6] F. Romanelli *et al*, Nucl. Fusion **26**, 1515 (1986)

[7] C. Angioni *et al.*, Phys. Plasmas **12**, 040701 (2005)

[8] C. Sung *et al.*, Nucl. Fusion **53**, 083010 (2013)

[9] A.E. White *et al.*, Phys. Plasmas **20**, 056106 (2013)

[10] A. Bortolon*et al.*, Phys. Rev. Lett. **97**, 235003 (2006)

[11] J.E. Rice*et al.*, Plasma Phys. Control. Fusion **50**, 124042 (2008)

[12] C. Angioni *et al.*, Phys. Rev. Lett. **107**, 215003 (2011)

[13] R.M. McDermott *et al.*, Nucl. Fusion **54**, 043009 (2014)

[14] J.C. Hillesheim*et al.*, Nucl. Fusion **55**, 032003 (2015)

[15] Y.J. Shi*etal.* Nucl. Fusion **53**, 113031 (2013)

[16] B.A. Grierson *et al.*, Phys. Rev. Lett. **118**, 015002 (2017)

[17] Ö. Gürcan *et al.*, Phys. Plasmas **14**, 042306 (2007)

[18] F.J. Casson *et al.*, Phys. Plasmas **16**, 092303 (2009)

[19] Y. Camenen *et al.*, Phys. Rev. Lett **102**, 125001 (2009)

[20] Y. Camenen it et al., Nucl. Fusion **51**, 073039 (2011)

[21] A.G. Peeters *et al.*, Nucl. Fusion **51**, 094027 (2011)

[22] P.H. Diamond *et al.*, Nucl. Fusion **53**, 104019 (2013)

[23] M. Barnes *at al.*, Phys. Rev. Lett. **111**, 055005 (2013)

[24] F.I. Parra, M. Barnes, Plasma Phys. Control. Fusion **57**, 045002 (2015)

[25] R. Buchholz *et al.*, Phys.Plasmas **21**, 062304 (2014)

[26] C. Sung *et al.*, Phys. Plasmas **23**, 042303 (2016)

[27] I.A. Kotelnikov, G.V. Stupakov, *Plasma physics lectures*, NSU 1996

[28] R. Fitzpatrick, *Plasma Physics: An Introduction*, CRC Press 2014

[29] J.P. Freidberg, Rev. Mod. Phys. **54**, 3 (1982)

[30] R. D. Hazeltine, J. D. Meiss, *Plasma confinement*, Courier Corporation 2003

[31] U. Stroth, *Plasmaphysik*

[32] B.D. Scott *et al.*, Contrib. Plasma Phys. **50**, No. 3-5, 228 241 (2010)

[33] W. Horton, Rev. Mod. Phys. **71**, 735 (1999)

[34] A.G. Peeters *et al.*, Phys. Plasmas **16**, 042310 (2009)

[35] J. Weiland *et al.*, Nucl. Fusion **29**, 1810 (1989)

[36] M. Oberparleiter *et al.*, Phys. Plasmas **23**, 042509 (2016)

[37] C. Angioni and O. Sauter, Physics of Plasmas **7**, 1224 (2000)

[38] G.V. Pereverzev and Y. P. Yushmanov, IPP Report 5/42 (1991)

[39] E. Fable *et al.*, Plasma Phys. Control. Fusion **55**, 124028 (2013)

[40] G.M. Staebler *et al.*, Phys. Plasmas **12**, 102508 (2005)

[41] G.M. Staebler *et al.*, Phys. Plasmas **14**, 055909 (2007)

[42] R.E Waltz *et al.*, Phys. Plasmas **4**, 2482 (1997)

[43] T.M. Antonsen, Jr. and B. Lane, Phys. Fluids **23**, 1205 (1980)

[44] Tilman Dannert and Frank Jenko, Phys. Plasmas **12**, 072309 (2005)

[45] A. Casati *et al.*, Nucl. Fusion **49**, 085012 (2009)

[46] D. Told *et.al.*, Phys. Plasmas **20**, 122312 (2013)

[47] E.A. Belli and J. Candy, Plasma Phys. Control. Fusion **50**, 095010 (2008)

[48] A. Medvedeva *et al.*, Plasma Phys. Control. Fusion **59**, 125014 (2017)

[49] I. Erofeev *et al.*, Nucl. Fusion **57**, 126067 (2017)

[50] O. Sauter *at al.*, Phys. Plasmas **6**, 2834 (1999)

[51] I.A. Ivonin *et al.*, Phys. Plasmas **6**, 3163 (1999)

[52] D.E. Post *et al.*, Atomica Data and Nuclear Tables **20**, p. 397 (1977)

[53] Kadomtsev B.B., Sov. J. Plasma Phys. Vol. 1 No. 5 Sept. Oct. 1975, p. 389.

[54] R. L. Miller, M. S. Chu, J. M. Greene, Y. R. Lin-Liu, and R. E. Waltz, Phys. Plasmas **5**, 973 (1998)

[55] G.M. Staebler *et al.*, Nucl. Fusion **57**, 066046 (2017)

[56] M. Porkolab *et al.*, Plasma Phys. Control. Fusion **54**, 124029 (2012)

[57] P. Ennever *et al.*, Phys. Plasmas **22**, 072507 (2015)

[58] J. Citrin *et al.* Plasma Phys. Control. Fusion **59**, 064010 (2017)

[59] J. Neuhauser *et al.*, Plasma Phys. Control. Fusion **44**, 855 (2002)

[60] F. Ryter *et al.*, Phys. Rev. Lett. **95**, 085001 (2005)

[61] E. Fable *et al.*, Plasma Phys. Control. Fusion **52**, 015007 (2010)

[62] O. Sauter *et al.*, Phys. Plasmas **21**, 055906 (2014)

[63] C. Angioni *et al.*, Phys. Plasmas **16**, 060702 (2009)

[64] H. Arnichand *et al.*, Nucl. Fusion **54**, 123017 (2014)

[65] H. Arnichand *et al.*, Plasma Phys. Control. Fusion **58**, 014037 (2016)

[66] A. Lebschy *et al.*, Nucl. Fusion **58**, 026013 (2018)

[67] F.X. Söldner *et al.*, Phys. Rev. Lett. **61**, 1105 (1988)

[68] M. Bessenrodt-Weberpals *et al.*, Nucl. Fusion **31**, 155 (1991)

[69] W. Hornsby *et al.*, Nucl. Fusion **57**, 046008 (2017)

[70] W. Hornsby *et al.*, Nucl. Fusion **58**, 056008 (2018)

[71] E. Fable, Plasma Phys. Control. Fusion **57**, 045007 (2015)

[72] Y.B. Kim *et al.*, Physics of Fluids B: Plasma Physics **3**, 2050 (1991)

[73] Y. Kishimote *et al.*, Plasma Phys. Control. Fusion **41**, A663 (1999)

[74] G.V. Pereverzev, G. Corrigan, Comput. Phys. Commun. **179**, 579-585 (2008)

[75] B.B. Kadomtsev, Sov. J. Plasma Phys. **1** 389 (1975)

[76] D. Strintzi, A.G. Peeters and J. Weiland, Phys. Plasmas **15**, 044502 (2008)

[77] A.G. Peeters, C. Angioni, D. Strintzi, Phys. Rev. Lett. **98**, 265003 (2007)

[78] H. Weisen *et al.*, Nucl. Fusion **52**, 042001 (2012)

Acknowledgements

First of all I would like to regard those who contributed greatly into the thesis and into my advancement as a scientist. I am very grateful to my executive supervisor Emiliano Fable, who attentively guided me over these years and always offered support by kind advises and discussions. The experience he shared with me in regard of the modelling approaches and techniques has built a solid basis for the thesis activities. I am also thankful to the leader of our scientific group Clemente Angioni for general planning and valuable educatory discussions. He supervised me softly but thoughtfully. Another warm thanks goes to Rachael McDermott, who introduced me to the experiments that formed the modelling background in this work and readily explained the details of measurements. She helped me understand that the experimental work is hard and that one has to interpret its results with care. I am grateful to Anna Medvedeva for sharing her experience with electron density profiles and operating the truly wonderful FRS diagnostic instrument. I am grateful to Valentin Igochine for our discussions on MHD that enlightened me in regard of the sawteeth instability.

Thanks to the HEPP Graduate School and especially to Peter Manz, who puts a lot of effort to it and who much concerns himself with his students. Thanks to the Technical University of Munich for its doctoral programme, I wish it good luck for its 150th birthday.

I would like to thank my office mates Alexander Ross, Menglong Zhao and Patrik Astfalk for keeping the friendly and cozy atmosphere in the office. Our talks inspired me for some good ideas. Additional thanks to Alex for correcting the Zusammenfassung of this thesis. I would like to thank the previous inhabitants of our office for leaving the plants that I could care about and that brought me comfort in times of doubts and reflection. I would like to thank our secretary staff Anja Bauer, Petra Jordan and Margot Jung, who know everything and who are glad to help anytime. A separate thanks to them for keeping the coffee machine up and running.

Upon arrival to Garching I entered a very friendly community of Russian-speaking people, who stayed close and kind no matter what the political background would be. Over the years some people left, but others arrived and joined, so the idea of unification lives on. The main activity remains the after-lunch tea drinking, and since for more than two years it was mostly myself who prepared the tea, I feel to a certain degree responsible for keeping this union together. I want to thank the friends and colleagues who I spent a lot of time with. I particularly thank Dima Meshcheriakov

for his honesty and philosophical thinking, Anton Bogomolov for his liveliness and optimism and Masha Usoltceva for sharing musical activities.

I want to express my respect and gratitude to my parents for supporting me in whatever direction I choose to follow, for their trust and love. Finally, I address my special thanks to Vesta Matveeva for peace and unity, now and forever.